NUMERICAL MODELING OF MULTIPHASE FLOWS IN POROUS MEDIA AND ITS APPLICATION IN HYDRAULIC ENGINEERING

A thesis submitted

by

NENAD JAĆIMOVIĆ

to

the Department of Urban Management

in partial fulfillment of the requirements for the degree of

Doctor of Philosophy

Kyoto University

Kyoto, Japan

June, 2007.

Abstract

Multiphase flows are governed by three-dimensional Navier Stokes equations for each involved phase. Therefore, solution of these equations for given boundary and initial conditions, in principle, would determine the flow field in time and space. Generally, boundaries between involved phases are not known a priory, but are part of the solution; or in the case of flows in a porous medium, these boundaries have too complicated geometry to be resolved mathematically. This resulted into development of simplified models, where the level of simplifications determines the model applicability. However, in order to represent simulated flows accurately, the model should include as much as possible relevant mechanisms and fluid properties.

In this study, a numerical model is developed based on finite volume method, in which the volume averaged governing equations are solved. In contrary to the simplified models, a full momentum equations for each involved phase is considered. Such model is utilized in the study to investigate commonly adopted simplifications, and their effects on the model applicability. Namely, for the flows in porous media, the effects of acceleration terms in momentum equations are investigated; first for the saturated groundwater flow, and then, for the air/water flow during air injection into initially saturated soil. It is revealed that in the case of saturated flow in homogeneous, incompressible, low permeable soils, the pressure adapts the new imposed boundary conditions instantaneously, while the velocities reach the quasi-steady conditions extremely fast. In the case of heterogeneous soil, pressure and velocity field have transient nature, but quickly reach the quasi-steady conditions. Only during this onset of flow, the inertia terms play a role.

In the case of air/water flow during air sparging, it is revealed that acceleration becomes important for porous medium with average grain size larger than 2 mm. This implies that simulations of such flow in coarse sands and gravels should include acceleration. It is explicitly shown that phenomena of flow pulsation, manifesting as steady pulsation at the constant air-injection flow rate, can be modeled only by inclusion of acceleration terms in governing equations. Theoretical analysis, conducted by application of one-dimensional stability analysis, revealed that inertial effects promote the instability, while the capillary forces oppose it. Ratio of these forces determines the onset of instability. It is showed that for materials with average grain size smaller than 2 mm, instability can not be expected.

In order to apply the model for simulation of contaminant removal during air sparg-

ing, the contaminant transport model is supplied. Mechanistic numerical models inherently assume that involved phases are completely mixed, and by now reported models commonly assume the local equilibrium of contaminant between the air and water phase. As reported by many investigators, this leads toward an overestimated contaminant removal. Therefore, in this model a channel air flow pattern is considered, where transfer of contaminant between the water and the air phase is modeled according to two film theory. Diffusive process of contaminant transport toward the air phase is modeled by a first order kinetic process between two water compartments: a immobile compartment in contact with the air phase and mobile compartment which has no contact with the air phase. Application of the developed model to reported two-dimensional experiment, showed a good agreement between simulated and measured transient change of dissolved contaminant in the water.

This study also showed that single numerical model, through the minor refinements, can be applied to wide variety of hydraulic engineering problems. By inclusion of gas compressibility, and mass exchange between the gas and the water phase in continuity equations, with adapting the drag term in momentum equations, a bubble plume model is proposed which can be utilized for simulation of lake amelioration by gas (air or pure oxygen) injection. Model is qualitatively and quantitatively validated by comparison with reported experiments from the literature. Hypothetical simulation of pure oxygen injection into 50 m deep lake showed that, due to ambient water entrainment into the gas plume, a significant spreading of dissolved oxygen can not be expected. Therefore, a optional gas injection strategy should be considered. Developed model can be utilized in order to propose an optimal gas injection design.

Finally, the same numerical model is proposed for simulation of flow in complex flow domains, consisting of bulk water and flow in porous medium with free surface boundary. Model is formulated in generalized curvilinear coordinates, in order to provide adequate representation of irregular boundaries. In contrast to earlier proposed boundary conditions at the two domain interface, in this model a continuity of velocities and stresses is assumed; for both regions a single set of governing equations is solved. Model application is illustrated by simulation of embankment overflow and its effect on effective stresses in the porous medium. It is showed that coupled, bulk water and groundwater flow, significantly influence the slope failure potential, here quantified by the Coulomb failure coefficient for non cohesive soils.

Acknowledgments

The thesis you are holding is a result of two and a half years of study, conducted at the River Engineering and Management Laboratory of the Department of Urban Management, Kyoto University. Many people, directly or indirectly, contributed toward completion of this study. Most of them I have mentioned herein, however, I am taking this opportunity to apologize to those I have inadvertently omitted.

I express my sincere appreciation to my supervisor, Professor Dr. **Takashi Hosoda**, whose tireless patience and effort greatly contributed toward the completion and, I hope, success of this study. His ideas at first place, but also advices, provided handouts and discussions helped me greatly.

Special thanks to Professor Dr. **Marko Ivetić** who advised me to come to Kyoto, but also who thought me fundamental principles of numerical modeling. His advices, suggestions and encouragements during my stay in Japan helped me a lot.

I am indebted to Associate Professor Dr. **Kiyoshi Kishida** for comments and proof readings, especially in the beginning of this study, when it was the most difficult. My special thanks are due to research assistant Dr. **Shinichiro Onda**, who was an excellent host and whose assistance helped me greatly in many aspects.

My special thanks go to my examiners, Associate Professor Dr. **Satoru Ushijima** and Associate Professor Dr. **Hitoshi Gotoh**, for valuable discussions and suggestions.

Needless to say, I am greatfull to all members of the River Engineering and Management laboratory for pleasant working environment they provided. Here, I met many of kind and interesting people among former and present students, from all over the world. I am especially thankful to my friends Dr. **Prosper Mgaya** and Dr. **Tran Ngoc Anh** for fruitful discussions and assistance over many issues.

Special thanks to my dear colleagues and friends at Belgrade University, Dr. **Dušan Prodanović**, **Dragutin Pavlović**, **Ana Mijić** and **Nemanja Branisavljević** for taking my responsibilities there, during my stay in Japan.

I am also taking this opportunity to express my deepest gratitude to my lovely wife **Jelena Jaćimović** and my lovely daughters **Una** and **Tara**. Their encouragement and support brightened the entire study.

Finally and certainly very importantly, I wish to acknowledge gratefully the financial support from the *Japanese Government Scholarship* "Monbusho", which enabled me this great opportunity; to live and study in Japan.

Dedication

Dedicated to my parents, Milenka and Milan Jaćimović.

Preface

The content of this thesis includes the contents of the following published and/or submitted journal and conference papers:

Jacimovic, N., T. Hosoda, K. Kishida and M. Ivetic (2005), Numerical Solution of the Navier-Stokes equations for incompressible flow in porous media with free surface boundary, Journal of Applied Mechanics, JSCE, Vol.8, pp. 225-231.

Jacimovic, N., T. Hosoda, K. Kishida and M. Ivetic (2005), Numerical solution of Navier-Stokes equations for incompressible flow in porous media, In the CD-Proceedings of the 40th Japan National Conference on Geotechnical Engineering JGS, 2.-5. July Hakodate-Japan , No.468.

Jacimovic, N., T. Hosoda, K. Kishida and M. Ivetic (2006), Two-phase numerical model for air sparging simulation with modeling of acceleration terms, Journal of Applied Mechanics, JSCE, Vol.9, pp. 765-771.

Onda, S., T. Hosoda, T. Uchida and N. Jacimovic (2006), Numerical simulation of unsteady flood flows with unknown boundary conditions, In the Proceedings of the 7-th International Conference on Hydroinformatics 2006, Vol. 3, pp. 1619-1626.

Jacimovic, N., T. Hosoda, K. Kishida and M. Ivetic (2006), A new numerical model for simulation of air sparging, In the CD-Proceedings of the 41th Japan National Conference on Geotechnical Engineering JGS, 12.-15. July, Kagoshima-Japan , No.593.

Jacimovic, N., T. Hosoda, K. Kishida and M. Ivetic (2006), Two-phase numerical model for simulation of air sparging, In the CD-Proceedings of the 2nd Int. Conference on Environmental Science and Technology AAS, 12.-15. August, Houston-USA , No.659.

Jacimovic, N., T. Hosoda, K. Kishida and M. Ivetic (2006), Numerical Simulation of Embankment overflow and its application on the slope failure estimation, In the Proceedings of the 20th Symposium on Computational Fluid Dynamics JSFM, 18.-20. December, Nagoya-Japan , No. F6-1.

Jacimovic, N., T. Hosoda, K. Kishida and M. Ivetic (2007), Numerical simulation of contaminant removal during air sparging, Annual Journal of Hydraulic Engineering, JSCE, Vol.51, pp. 13-18.

Jacimovic, N., T. Hosoda, M. Ivetic and K. Kishida (2007), A novel approach in numerical simulation of contaminant removal by air sparging, Groundwater Management in the Danube River Basin and Other Large River Basins - IWA, Paper accepted for oral presentation, 5. -7. June, Belgrade, Serbia.

Contents

List of Figures

List of Tables

Chapter 1

Introduction

1.1 Preliminaries

Multiphase flows are very common in many areas of hydraulic engineering, geoscience or industry. For example, oil/gas extraction, groundwater flow and transport, underground disposal of hazardous materials, soil remediation, etc., involve systems with different substances or different phases of matter (solid, liquid or gas) in coexistence. A phase in multiphase system can be dispersed (i.e. not materially connected) such as particles, droplets or bubbles. Multiphase flows can be also non-dispersed such as fluid flows through a porous material, or immiscible flows of NAPL (Non-Aqueous Phase Liquid) and water. Saturated groundwater flow can also be considered as two phase flow, in which one phase (porous medium) is stagnant.

Flow dynamics of such flows is significantly more complex than single fluid flows, mainly due to existence of the interphase between the phases. Through the interface several physical processes appear, such as transfers of energy, mass and momentum. A primary difficulty is prediction of the shape and position of the interface between different phases. In general, the geometry and spatial distribution of the interface is not known a priory, but it is a part of the solution. From the mathematical point of view, the interface represents discontinuity for certain quantities, e.g. pressure, density or viscosity, from which computational difficulties arise.

An inherently complex flow structure resulted in model simplifications in order to

simulate such flows. Therefore, the underlying multiphase character is often neglected, and the system is treated formally as a single-phase. This leads to so called *Homogeneous models*, where the assumption of mechanical equilibrium (i.e. relative velocity equals zero) is utilized. Therefore, only one velocity field needs to be computed, with averaging of physical parameters. This approach is, for example, utilized for modeling of dispersed flows, where viscous forces dominate over inertial and buoyancy forces. In the case of unsaturated flows in porous medium, the air phase is often neglected, assuming it under a constant (atmospheric) pressure, i.e. stagnant. Actually, the fact is that air phase has significantly higher mobility in the porous materials, and its effects on groundwater flow may, under some circumstances, be neglected. Introduction of constitutive equation for relative velocity between the phases leads to so called *Diffusion models*, where difference between the phase velocities is allowed. This approach is extensively utilized in modeling of bubble plumes, with constant, vertical slip velocity of the air phase [e.g. Kobus 1968; McDougall 1977; Milgram 1983; Sokolichin and Eigenberger 1994; etc.].

Among the different multiphase flow models which can be found in the literature, multidimensional models with balance equations for each of the phases, presently allow most detailed description of multiphase flows. This is especially true in the cases where along the flow, another accompanying processes are of interest, such as mass transfer and transport.

Multiphase flow and transport processes in subsurface were first modeled in the petroleum industry, in order to predict oil recovery as a result of its displacement by gas or water. The Buckley-Leverett [1941] one-dimensional theory was mainly utilized before occurrence of numerical models. Recently, as the environmental concerns are growing and as the NAPL-s are encountered in the subsurface more frequently, numerical modeling of multiphase systems became very important in the groundwater quality fields. Here, the main objective is to predict the fate of pollutant in the subsurface and extents of its influence on groundwater quality. Similar approach in modeling was used in both aforementioned fields [Lake 1989, Bear and Bachmat 1991], with formally the same continuum balance equations and closure (constitutive) relations. The common approach in all these models is that acceleration effect in all involved phases can be neglected.

Logical extension of application of multiphase system modeling is simulation of soil remediation technologies, such as steam injection [Falta *at al.*, 1992a, 1992b], soil venting

[Baehr *at al.*, 1989; Gierke *at al.*, 1990; Brusseau, 1991] or air sparging ¯Unger *at al.*, 1995; Lundegard and Andersen, 1996; McCrey and Falta, 1997]. However, in this case, the lack of model validation by comparison with measured in situ or laboratory data is evident.

1.2 The Topics to be Studied

The main objective of this study is development a detailed numerical model for simulation one/two phase flows, capable for simulation of free fluid/porous media flows. It is assumed that flow field is exactly defined by mass balance and Navier-Stokes equations accompanied with related boundary conditions. Necessary constitutive relations are taken from the literature, without analysis of their reliability. Such detailed model enables analysis of different phenomena encountered in multiphase flows. For example, effects of acceleration terms on air flow and distribution during air sparging, which are neglected in all to date published numerical models. This approach is very important, since multiphase flows involve complex processes which require understanding of many fundamental mechanisms. This, in turn, should lead to better handling of realistic problems. In that way, this research can also be considered as experimental study (numerical, though) in which some aspects of multiphase flows in porous media and in free fluid are analyzed.

Development of numerical model involves several topics which require attention. This includes:

- Theoretical considerations
- Model development and verification (discretization methods and solution techniques)
- Methods of dealing with complex flow domains
- Model application

Theoretical background of multiphase flows is well established in the literature, however, some observed phenomena still require theoretical explanation. Example is a phenomena of flow pulsation during the air sparging in coarse materials, which is analytically and numerically treated in this study.

The governing, volume averaged equations, are discretized by control volumes. This enables writing of all governing equations in conservative form and preserving this property in

discretized form. Model is verified by comparison with analytical solutions, another numerical methods or by application on laboratory experiments, where appropriate data were available.

Developed model is further refined by formulation in generalized curvilinear coordinates. This enables fruitful treatment of complex flow domains, which are often encountered in real problems. This, of course, has to be paid by more complicated governing and discretized equations.

It is showed in this study that the same model, through the minor refinements, can be applied for wide variety of hydraulic problems. Several of them are treated in this study: simulation of air sparging, modeling of bubble plumes and simulation of flows in a complex flow domains, consisting of bulk fluid and porous medium with free surface boundaries.

1.3 Scope of the study

Chapter 2 presents theoretical ground of governing equations for multiphase flows which are numerically solved in this study. Chapter 3 is devoted in the development and verification of the proposed numerical model. The model validation is firstly accomplished through comparison of the numerical solution to the analytical solution of the Buckley-Leverett problem, and then, by comparison with finite element solution of the free surface flow in porous medium. Further verification is also provided in the following chapters by comparisons with analytical solutions and laboratory experiments, where different types of flows are treated.

In the Chapter 4, analysis of acceleration terms effects on the pressure redistribution in a deep, low permeability soil is conducted. Here, numerical results are compared with derived analytical solutions for homogeneous and heterogeneous cases.

Flow simulations of air sparging is presented in Chapter 5. Also, the role of acceleration terms on flow fields and air distribution in initially saturated soil is analyzed. In addition, the contaminant transport model is proposed as a component of the developed multiphase flow model. Comparison with some reported experiments from the literature is presented.

Chapter 6 is devoted in refinement and application of developed model for simulations of bubble plumes in a clear water. Simulations of reported experiments in a flat water tank are presented, as model validation. Its application to deep lake amelioration is

illustrated by simulation of pure oxygen injection.

In the Chapter 7 model is further refined by formulation in generalized curvilinear coordinates. Then, it is applied for simulation of flow in a complex flow domains with free surface boundaries. A fundamental analysis of combined effects of bulk fluid and groundwater flow on effective stresses in overflowed embankment is presented.

Finally, conclusions and some recommendations are made in Chapter 8.

Chapter 2

Governing equations of multiphase flows

2.1 Preliminaries

In order to formulate mathematical model of multiphase flow in porous media, it is necessary to address several concepts, which will enable us to apply differential apparatus in describing the flow of multiphase systems. One of the most important concepts is *Continuum approach* in dealing with multiphase (solid, air, water, etc.) system. According to this concept, the system with several phases is replaced by fictive continuum, in which for every point it is possible to assign any property, of any phase in the system.

A multiphase system is composed of inter-penetrating phases, with each phase occupying only part of the whole system. Phases are divided by the highly irregular interphase boundaries (surfaces), which may have some thermo-mechanical properties, such as surface tension. Through the interface, there is exchange of extensive quantities (e.g. mass, momentum, energy). Each phase is characterized by its thermodynamic quantities, which are continuous for that phase, but discontinuous over the whole system. Locally, the standard balance laws can be applied for each of the phases. Those equations, supported by the appropriate boundary conditions and with conditions at the interphase surfaces may provide, in principle, the state of the system.

Since the solution of those equations at this, microscopic scale is a formidable task,

the common procedure is to obtain the governing equations at the macroscopic scale. This change, from the microscopic to macroscopic scale is accomplished through the application of appropriate averaging procedure for various types of flows. If we consider only Eulerian averaging techniques, several averaging procedures can be found in the literature: volume averaging, time averaging, both time and volume averaging and statistical (ensemble) averaging [e.g. Ishii, 1975; Drew and Prassman, 2000]. In the theoretical analysis of flows in porous media, the volume averaging over some representative elementary volume (REV) [Bear, 1972, pp. 19], is the most common way to obtain macroscopic governing equations. This volume represents mathematical point at the macroscopic scale, at which the quantities of all available phases in the system are defined. Through this change of the scale, hydraulic variables and parameters become continuous variables of time and space. In fact, obtained fictive continuum represents the overlapping continuum for every available phase. Fortunately, the engineering practice is most often concerned with a gross (macroscopic) properties, without need to know the exact locations of the particular phase in the system. In addition, the measurement of specific properties is only possible as some kind of average (e.g. time, mass or volume average) of microscopic quantities.

Volume averaging procedure is well established in the literature. Since understanding of origins of several terms in macroscopic balance equations is of great importance in terms of their numerical modeling, a brief explanation of averaging procedure is given in this chapter. These terms are a consequence of scale change from microscopic to macroscopic, as it will be showed in the following sections.

2.2 Volume averaging of the balance equations

Volume averaging procedure is presented by several researchers [Slattery, 1969; Whitaker, 1969; Gray and O'Neill, 1976; Neuman, 1977; etc.]. However, probably the most general approach is reported by Hassanizadeh and Gray [1979a; 1979b; 1980]. The derivation presented here, mainly follows the study reported by Hassanizadeh and Gray [1979a], which is here slightly adapted for the types of flows which will be numerically treated in this thesis. For now, the main concern is mechanical phenomena and therefore, only derivations of the macroscopic mass and momentum balance equations will be presented, under isothermal

conditions.

At the microscopic scale, single phase flow is governed by the mass and momentum balance equations, which in their most general form can be written as [e.g. Aris, 1962]:

$$\frac{\partial \rho}{\partial t} + \nabla \cdot (\rho \mathbf{v}) = 0 \tag{2.1}$$

$$\frac{\partial (\rho \mathbf{v})}{\partial t} + \nabla \cdot (\rho \mathbf{v}\mathbf{v}) = \rho \mathbf{f} + \nabla \cdot \mathbf{T} \tag{2.2}$$

where ρ is the fluid density, $\mathbf{v}$ is the velocity vector, $\mathbf{f}$ is the body-force vector per unit mass, $\mathbf{T}$ is the stress tensor and ∇ represents a divergence operator which in Cartesian coordinates can be expressed as:

$$\nabla = \frac{\partial}{\partial x}\mathbf{e}_x - \frac{\partial}{\partial y}\mathbf{e}_y + \frac{\partial}{\partial z}\mathbf{e}_z \tag{2.3}$$

where $\mathbf{e}_x$, $\mathbf{e}_y$ and $\mathbf{e}_z$ are unit vectors in x, y and z directions, respectively.

The first term on the left side of Equation (2.2) represents the acceleration of a fluid particle, because, at a fixed point in space, the velocity may change with time. The second term, the advective acceleration, represents the acceleration that a particle may have, even in a steady-state flow field, by virtue of moving to a location at which there is a different velocity. The forcing terms on the right side represent the applied body force, and the surface forces. Often, the only appreciable body force is gravity, in which case $\mathbf{f} = -g\mathbf{e}_z$, where $\mathbf{e}_z$ is the unit vector in the upward vertical direction and $g = 9.81$ m/s^2.

Equations (2.1) and (2.2) are valid for every subregion of the multiphase system where the the considered phase is available. At the interphase boundaries these equations are not valid, but appropriate quantities (mass and momentum) have to be conserved. Therefore, the "jump" conditions at the boundaries can be formulated as [e.g. Hassanizadeh and Gray, 1979a; Drew and Passman, 2000]:

mass balance:

$$[\rho(\mathbf{w} - \mathbf{v})] \cdot \mathbf{n} = 0 \tag{2.4}$$

momentum balance:

$$[\rho \mathbf{v}(\mathbf{w} - \mathbf{v}) + \mathbf{t}] \cdot \mathbf{n} = 0 \tag{2.5}$$

where $\mathbf{w}$ represents the velocity of the interface and the boldface brackets denote the jump over the interface. The right side of the equation (2.5) is not zero in the case that interface has thermodynamic properties.

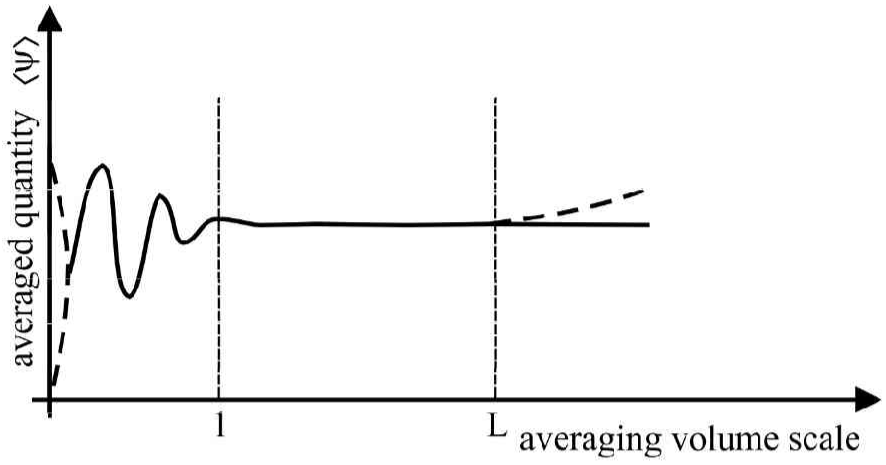

Figure 2.1: Dependence of averaged quantity on the averaging scale after Bear [1972].

In order to obtain macroscopic equations, the equations (2.1) and (2.2) are averaged over the small volume dV which is bounded by the surface dA. This volume contains all fluids of interest and in order that obtained averaged quantities do not depend on the size of this volume, it is necessary that the scale of volume dV satisfies certain conditions. If we denote this scale by D, condition can be expressed as [Whitaker, 1969]:

$$l \ll D \ll L \tag{2.6}$$

where l is the characteristic microscale length and L is the scale of the gross inhomogeneities which may cause the change of the averaging quantities. This can be seen in Figure (2.1); if the averaging volume is too small, of the scale l, the local condition affects the averaging quantity (for example, if the averaging volume contains only one fluid, the averaged quantities of the other fluids are all zero). If the condition (2.6) can not be fulfilled from some reason, the averaging procedure can not obtain valid macroscopic equations.

Figure (2.2) shows the volume dV which is characterized by its center vector $\mathbf{x}$ in some referent coordinate system. Any point in the averaging volume can be referenced with a vector $\mathbf{r}$ in the same reference, or by the vector ξ in the local coordinates parallel to referent coordinates. The center represents the macroscopic point for which the averaged quantities are defined. For the sake of simplicity, only two phases (phase α and phase β) are present here, however, the following equations are valid for any number of phases.

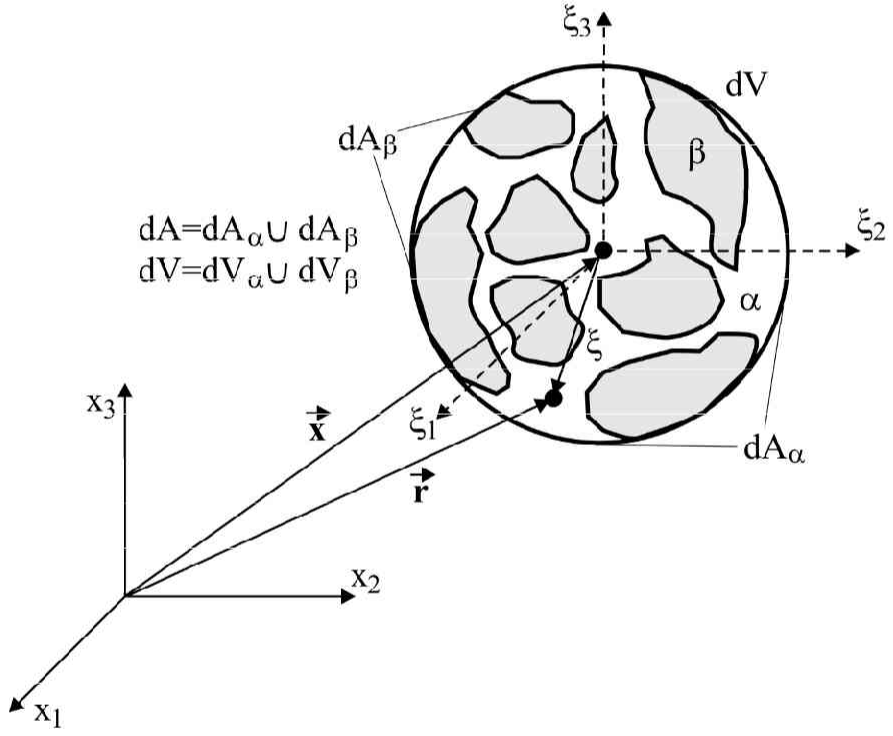

Figure 2.2: A REV containing two phases α and β.

There are two types of boundaries for each of the phases. First, the internal boundaries between the phases $dA^{\alpha\beta}$ and two, a part of the surface dA, here denoted as dA_α. Therefore, $dA = dA_\alpha \cup dA_\beta$. For the averaging volume, it can also be written $dV = dV_\alpha \cup dV_\beta$. Portion of the volume dV, occupied by the phase α is $\alpha = dV_\alpha / dV$.

The phase distribution function can be defined to characterize the geometry of the phase considered [Whitaker, 1969; Hassanizadeh and Gray 1979a]:

$$\varphi_\alpha(\mathbf{r}, t) = \begin{cases} 1 & \text{if} \quad \mathbf{r} \in \alpha \\ 0 & \text{if} \quad \mathbf{r} \in \beta \end{cases} \tag{2.7}$$

Several identities can be derived, using the phase distribution function:

$$dV_\alpha = \int_{dV} \varphi_\alpha \, d\upsilon \tag{2.8}$$

$$dA_\alpha = \int_{dA} \varphi_\alpha \, da \tag{2.9}$$

$$\int_{dV_\alpha} \psi_\alpha \, d\upsilon = \int_{dV} \psi_\alpha \varphi_\alpha \, d\upsilon \tag{2.10}$$

where $d\upsilon$ denotes integration over the volume dV in local coordinates, da the microscopic element of the area dA and ψ_α represents some extensive quantity of the phase α. Equation (2.10) shows that the volume integral over the phase α can be replaced by the integral over the whole volume dV.

Using the phase distribution function, several averaging operators can be defined, such as volume average, intrinsic volume average, mass average and surface average:

$$\langle \psi_\alpha \rangle(\mathbf{x}, t) = \frac{1}{dV} \int_{dV} \psi_\alpha(\mathbf{r}, t) \varphi_\alpha(\mathbf{r}, t) \, d\upsilon \tag{2.11}$$

$$\langle \psi_\alpha \rangle^\alpha(\mathbf{x}, t) = \frac{1}{dV_\alpha} \int_{dV} \psi_\alpha(\mathbf{r}, t) \varphi_\alpha(\mathbf{r}, t) \, d\upsilon \tag{2.12}$$

$$\overline{\psi_\alpha}(\mathbf{X}, t) = \frac{1}{\langle \rho_\alpha \rangle(\mathbf{x}, t) dV} \int_{dV} \psi_\alpha(\mathbf{r}, t) \varphi_\alpha(\mathbf{r}, t) \, d\upsilon \tag{2.13}$$

$$\hat{\mathbf{f}}_\alpha(\mathbf{x}, t) = \frac{1}{dA} \int_{dA} \mathbf{f}(\mathbf{r}, t) \varphi_\alpha(\mathbf{r}, t) \mathbf{n} \, da \tag{2.14}$$

Comparing the equations (2.11) and (2.12), volume average and intrinsic volume average can be related by $\langle \psi_\alpha \rangle = \alpha \langle \psi_\alpha \rangle^\alpha$. As pointed out by Hassanizadeh and Gray [1979a], specific fluid quantities should be averaged by appropriate averaging operator, taking into account the intrinsic nature of the property.

2.2.1 Averaging of the mass balance equation

In order to obtain averaged forms of balance equations (2.1) and (2.2) for the specific phase α, after averaging on the REV dV, the microscopic equations have to be integrated over the small macroscopic volume V. Applying this procedure on the first term of equation (2.1) yields:

$$\int_V \left[\frac{1}{dV}\int_{dV}\frac{\partial \rho_\alpha}{\partial t}\varphi_\alpha d\upsilon\right] dV_x = \int_V \frac{\partial}{\partial t}\left[\frac{1}{dV}\int_{dV}\rho_\alpha\varphi_\alpha d\upsilon\right] dV_x - \int_V \left[\frac{1}{dV}\int_{dA^{\alpha\beta}}\rho_\alpha \mathbf{w}\mathbf{n}^{\alpha\beta} da\right] dV_x \tag{2.15}$$

where dV_x represents integration which is carried out in $\mathbf{x}$ coordinates and $\mathbf{n}^{\alpha\beta}$ is the unit normal vector of the interphase surface in the direction from phase α to phase β.

After applying equation (2.11) to the first term on the right side, equation (2.15) can be expressed as:

$$\int_V \left[\frac{1}{dV}\int_{dV}\frac{\partial \rho_\alpha}{\partial t}\varphi_\alpha d\upsilon\right] dV_x = \int_V \frac{\partial \langle\rho_\alpha\rangle}{\partial t} dV_x - \int_V \left[\frac{1}{dV}\int_{dA^{\alpha\beta}}\rho_\alpha \mathbf{w}\mathbf{n}^{\alpha\beta} da\right] dV_x \tag{2.16}$$

The same procedure for the second term of equation (2.1) yields:

$$\int_V \left[\frac{1}{dV}\int_{dV}\nabla\cdot(\rho_\alpha\mathbf{v}_\alpha)\varphi_\alpha d\upsilon\right] dV_x = \int_V \nabla\left[\frac{1}{dV}\int_{dV}\rho_\alpha\mathbf{v}_\alpha\varphi_\alpha d\upsilon\right] dV_x - \int_V \left[\frac{1}{dV}\int_{dA^{\alpha\beta}}\rho_\alpha\mathbf{v}_\alpha\mathbf{n}^{\alpha\beta} da\right] dV_x \tag{2.17}$$

$$\int_V \left[\frac{1}{dV}\int_{dV}\nabla\cdot(\rho_\alpha\mathbf{v}_\alpha)\varphi_\alpha d\upsilon\right] dV_x = \int_V \nabla\cdot(\langle\rho_\alpha\rangle\overline{\mathbf{v}}_\alpha) dV_x + \int_V \left[\frac{1}{dV}\int_{dA^{\alpha\beta}}\rho_\alpha\mathbf{v}_\alpha\mathbf{n}^{\alpha\beta} da\right] dV_x \tag{2.18}$$

Summing equations (2.16) and (2.18) gives a macroscopic mass balance equation in the integral form:

$$\int_V \frac{\partial\langle\rho\rangle_\alpha}{\partial t} dV_x + \int_V \nabla\cdot(\langle\rho\rangle_\alpha\overline{\mathbf{v}}_\alpha) dV_x = \int_V \left[\frac{1}{dV}\int_{dA^{\alpha\beta}}\rho_\alpha(\mathbf{w}-\mathbf{v}_\alpha)\mathbf{n}^{\alpha\beta} da\right] dV_x \tag{2.19}$$

where the term on the right side represents exchange of the mass through the boundary between the phases α and β. In the case of more than two phases, the exchange of the mass would be integrated over all interfaces of the fluid α.

In equations (2.15) and (2.16) two important theorems were used which relate integral of a derivative to the derivative of the integral [Whitaker, 1969; Slattery 1969]:

Theorem I:

$$\left\langle \frac{\partial \psi_\alpha}{\partial t} \right\rangle = \frac{\partial}{\partial t} \langle \psi_\alpha \rangle - \frac{1}{dV} \int_{dA_{\alpha\beta}} \psi_\alpha \mathbf{w}\mathbf{n}^{\alpha\beta}\, da \tag{2.20}$$

Theorem II:

$$\langle \nabla \psi_\alpha \rangle = \nabla \langle \psi_\alpha \rangle + \frac{1}{dV} \int_{dA_{\alpha\beta}} \psi_\alpha \mathbf{n}^{\alpha\beta}\, da \tag{2.21}$$

Equation (2.20) represents general transport theorem for the fixed point. In the case where boundary velocity equals fluid velocity, this becomes Raynolds' transport theorem [e.g. Aris, 1962, pp.84]. The proof of these theorems is quite simple, as presented by Gray and Lee [1977].

In the differential form, equation (2.19) can be expressed as:

$$\frac{\partial \langle \rho \rangle_\alpha}{\partial t} + \nabla \cdot (\langle \rho \rangle_\alpha \overline{\mathbf{v}}_\alpha) = M_{\alpha\beta} \tag{2.22}$$

where $M_{\alpha\beta}$ represents a mass exchange term.

2.2.2 Averaging of the momentum balance equation

The first term of equation (2.2) can be treated in a similar manner:

$$\int_V \left[\frac{1}{dV} \int_{dV} \frac{\partial(\rho_\alpha \mathbf{v}_\alpha)}{\partial t} \varphi_\alpha dv \right] dV_x = \int_V \frac{\partial}{\partial t} (\langle \rho_\alpha \rangle \overline{\mathbf{v}}_\alpha) dV_x - \int_V \left[\frac{1}{dV} \int_{dA^{\alpha\beta}} \rho_\alpha \mathbf{v}_\alpha \mathbf{w}\mathbf{n}^{\alpha\beta} da \right] dV_x \tag{2.23}$$

Before applying the above scheme on the second term of equation (2.2), the velocity of the α phase will be expressed as a sum of a mass average ($\overline{\mathbf{v}}_\alpha$) and deviation ($\tilde{\mathbf{v}}_\alpha$):

$$\mathbf{v}_\alpha(\mathbf{r}, t) = \overline{\mathbf{v}}_\alpha(\mathbf{x}, t) + \tilde{\mathbf{v}}_\alpha(\mathbf{r}, t), \tag{2.24}$$

with valid following identities:

$$\overline{\tilde{\mathbf{v}}_\alpha} - 0 \tag{2.25}$$

$$\overline{\tilde{\mathbf{v}}_\alpha \overline{\mathbf{v}}_\alpha} = 0 \tag{2.26}$$

$$\overline{\mathbf{v}_\alpha \mathbf{v}_\alpha} = \overline{\mathbf{v}}_\alpha \overline{\mathbf{v}}_\alpha + \overline{\tilde{\mathbf{v}}_\alpha \tilde{\mathbf{v}}_\alpha} \tag{2.27}$$

Expressing the quantity as a deviation from the average value is a common procedure in analysis of fluid dynamics. The same approach is used in turbulence analysis, where $\overline{\psi}$ is a time average [e.g. Hajdin, 1992]. In the mixture theory this value represents an ensemble average [Ishii, 1975; Drew and Prassman, 2000]. It can also represent both, the space and time average [Drew and Prassman, 2000].

Considering identities(2.25-2.27) and the theorem (2.21), the second term in equation (2.2) can be averaged as follows:

$$\int_V \left[\frac{1}{dV}\int_{dV} \nabla\cdot(\rho_\alpha \mathbf{v}_\alpha\mathbf{v}_\alpha)\varphi_\alpha dv\right] dV_x = \int_V \nabla\cdot(\langle\rho_\alpha\rangle\overline{\mathbf{v}}_\alpha\overline{\mathbf{v}}_\alpha)dV_x$$
$$+\int_A \left[\frac{1}{dA}\int_{dA}\rho_\alpha\tilde{\mathbf{v}}_\alpha\tilde{\mathbf{v}}_\alpha\varphi_\alpha\mathbf{n}da\right]dA_x + \int_V\left[\frac{1}{dV}\int_{dA^{\alpha\beta}}\rho_\alpha\mathbf{v}_\alpha\mathbf{v}_\alpha\mathbf{n}^{\alpha\beta}da\right]dV_x \tag{2.28}$$

The two terms on the right side of equation (2.2), can be expressed as:

$$\int_V\left[\frac{1}{dV}\int_{dV}\rho_\alpha\mathbf{f}\varphi_\alpha dv\right]dV_x = \int_V\langle\rho_\alpha\rangle\,\overline{\mathbf{f}}\,dV_x \tag{2.29}$$

$$\int_V\left[\frac{1}{dV}\int_{dV}(\nabla\cdot\mathbf{T})\varphi_\alpha dv\right]dV_x = \int_A\left[\frac{1}{dA}\int_{dA}\mathbf{T}\varphi_\alpha\mathbf{n}da\right]dA_x$$
$$+\int_V\left[\frac{1}{dV}\int_{dA^{\alpha\beta}}\mathbf{T}\mathbf{n}^{\alpha\beta}da\right]dV_x \tag{2.30}$$

In deriving of equation (2.30) another theorem is utilized:

Theorem III:

$$\int_V\left[\frac{1}{dV}\int_{dV}\nabla\cdot\mathbf{f}dv\right]dV_x = \int_V\nabla\left[\frac{1}{dV}\int_{dV}\mathbf{f}dv\right]dV_x = \int_A\left[\frac{1}{dA}\int_{dA}\mathbf{f}\mathbf{n}da\right]dA_x \tag{2.31}$$

for which the proof is given in Hassanizadeh and Gray [1979a].

Now, using the obtained identities (2.23), (2.28), (2.29) and (2.30), the macroscopic momentum equation can be written as:

$$\int_V\frac{\partial}{\partial t}(\langle\rho_\alpha\rangle\overline{\mathbf{v}_\alpha})\,dV_x + \int_V\nabla\cdot(\langle\rho_\alpha\rangle\overline{\mathbf{v}}_\alpha\overline{\mathbf{v}}_\alpha)\,dV_x = \int_V\langle\rho_\alpha\rangle\,\overline{\mathbf{f}}\,dV_x$$
$$+\int_A\left[\frac{1}{dA}\int_{dA}\mathbf{T}\varphi_\alpha\mathbf{n}da\right]dA_x - \int_A\left[\frac{1}{dA}\int_{dA}\rho_\alpha\tilde{\mathbf{v}}_\alpha\tilde{\mathbf{v}}_\alpha\varphi_\alpha\mathbf{n}da\right]dA_x$$
$$+\int_V\left[\frac{1}{dV}\int_{dA^{\alpha\beta}}\mathbf{T}\mathbf{n}^{\alpha\beta}da\right]dV_x + \int_V\left[\frac{1}{dV}\int_{dA^{\alpha\beta}}\rho_\alpha\mathbf{v}_\alpha(\mathbf{w}-\mathbf{v}_\alpha)\mathbf{n}^{\alpha\beta}da\right]dV_x \tag{2.32}$$

where the third term on the right side represents microscopic inertia effects, the fourth term represents exchange of momentum through the mechanical interactions and the last term on

the right side represents the exchange of the momentum between the phases through the mass exchange. Hassanizadeh and Gray [1979a] showed that force vector $\hat{\mathbf{t}}$, averaged over the boundary dA:

$$\hat{\mathbf{t}} = \frac{1}{dA}\int_{dA} \mathbf{T}\mathbf{n}\varphi_\alpha \, da \tag{2.33}$$

can be expressed as a function of a existent partial stress tensor ($\mathbf{T}^\alpha$) and the unit normal vector ($\mathbf{N}$):

$$\hat{\mathbf{t}} = \mathbf{T}^\alpha \mathbf{N} \tag{2.34}$$

They have grouped together the third and fourth term on the right side of equation (2.32) into single macroscopic stress tensor. However, $\mathbf{T}$ comes from viscous effects and the fourth term on the right side has a kinematic origin. Since inertia effects become more significant in the case of higher velocity flows in comparison with viscous effects, here will be separated and expressed in a body force form:

$$\overline{\mathbf{t}}^* = \frac{1}{\langle\rho_\alpha\rangle dV}\int_{dV} \nabla(\rho_\alpha \tilde{\mathbf{v}}_\alpha \tilde{\mathbf{v}}_\alpha \varphi_\alpha)\, d\upsilon \tag{2.35}$$

In addition, it is possible to define $\overline{\mathbf{t}}^{\alpha\beta}$ as:

$$\overline{\mathbf{t}}^{\alpha\beta} = \frac{1}{\langle\rho_\alpha\rangle dV}\int_{dA^{\alpha\beta}} \mathbf{T}\mathbf{n}^{\alpha\beta}\, da \tag{2.36}$$

If there is no exchange of mass between the phases, $(\mathbf{w} - \mathbf{v}_\alpha)$ equals zero; as well as the last term in equation (2.32). In that case, substitution of (2.33-2.36) into (2.32) gives:

$$\begin{aligned}\int_V \frac{\partial}{\partial t}(\langle\rho_\alpha\rangle\overline{\mathbf{v}}_\alpha)dV_x + \int_V \nabla\cdot(\langle\rho_\alpha\rangle\overline{\mathbf{v}}_\alpha\overline{\mathbf{v}}_\alpha)dV_x &= \int_V \langle\rho_\alpha\rangle\,\overline{\mathbf{f}}\,dV_x \\ + \int_A \mathbf{T}^\alpha\mathbf{N}dA_x - \int_V \langle\rho_\alpha\rangle\,\overline{\mathbf{t}}^*dV_x &+ \int_V \langle\rho_\alpha\rangle\mathbf{t}^{\alpha\beta}dV_x\end{aligned} \tag{2.37}$$

which, in differential form, can be expressed as:

$$\frac{\partial}{\partial t}(\langle\rho_\alpha\rangle\overline{\mathbf{v}}_\alpha) + \nabla\cdot(\langle\rho_\alpha\rangle\overline{\mathbf{v}}_\alpha\overline{\mathbf{v}}_\alpha) = \langle\rho_\alpha\rangle\,\overline{\mathbf{f}} + \nabla\cdot\mathbf{T}^\alpha - \langle\rho_\alpha\rangle\,\overline{\mathbf{t}}^* + \langle\rho_\alpha\rangle\overline{\mathbf{t}}^{\alpha\beta} \tag{2.38}$$

Comparison between obtained macroscopic linear momentum balance equation (2.38) and starting, microscopic equation (2.2) shows that averaging procedure, or change of the scale, produced additional two terms. Namely, averaged interaction between the phases and averaged microscopic inertial effects. Obviously, these terms have to be experimentally estimated for specific multiphase flow. In the case of existence of mass transfer between the phases, there is an additional momentum exchange term, as shown in equation (2.32).

2.3 Saturated flow in porous media

2.3.1 Preliminaries

Saturated flow in porous media can be considered as a special case of multiphase flow with solid and fluid phase present. Since the establishment of the Darcy's law in 1856, as a generally accepted empirical macroscopic equation of motion in porous media for small Reynolds numbers [e.g. Bear, 1972], many authors have reported theoretical studies of flow in porous media. Some of them tried to derive the Darcy's law theoretically [Hubbert, 1956; Hall, 1956; Whitaker, 1966; Gray and O'Neill, 1976; Neuman, 1977] by averaging Navier-Stokes equations over a representative volume of porous media. Ahmed and Sunada [1969] used the same approach to derive macroscopic equation of motion for flows with greater Reynolds numbers, where linear dependency of hydraulic gradient and flux is not valid any more. Probably the most significant step toward theoretical analysis of flow in porous media was derivation of the theorem which relates volume averages of space derivatives and space derivatives of volume averages (Slattery, 1967; Whitaker, 1969] (Theorem II in previous section), as a spatial analog of general transport theorem. Some other authors presented an alternative approach by treating the flow in porous media as a stochastic process [Scheidegger, 1954; Bachmat, 1965], or by simplifying the structure of the pores (conceptual models) [Bear 1972]. In this case, the porous media is represented as a system of capillary tubes in some arrangement, with Hagen-Poisseuille's law as a starting governing equation.

Originally, the Darcy's law was established as an empirical correlation between the hydraulic gradient and volumetric flux for one-dimensional flow of a single fluid through the porous column:

$$Q = KA\frac{\Delta h}{L} \tag{2.39}$$

where Q is the volumetric flow rate, K is the constant of proportionality, A is the cross-sectional area of the porous column, Δh is the head difference along the column and L is the column length. Later, a generalized form of this relation was intuitively formulated as:

$$q_i = -K_{ij}J_j, \quad i,j = 1,2,3 \tag{2.40}$$

where q_i is the i-th component of specific discharge vector of the fluid, K_{ij} is the hydraulic conductivity tensor (assumed as symmetric), and J_j is the j-th component of hydraulic gra-

dient vector. Hydraulic conductivity tensor is often expressed as a function of permeability tensor as a property of porous media and characteristic fluid properties [Bear, 1972]:

$$\mathbf{K} = \mathrm{k}\frac{\rho_f g}{\mu_f} \tag{2.41}$$

where μ_f is the fluid viscosity. Symmetrical nature of permeability tensor is proved by Neuman [1977].

2.3.2 Averaged momentum balance equation and Darcy law

In this section, it will be showed that obtained volume-averaged equation of linear momentum balance (2.37) can be reduced to Darcy's law. The following analysis is restricted to the case of an incompressible homogeneous Newtonian fluid moving thorough the voids of rigid and stationary porous medium under isothermal and steady conditions.

Two constitutive relations have to be obtained for equation (2.37). A constitutive equation for fluid stress tensor, under incompressibility restriction may be written as:

$$T_{ij}^{\alpha} = -\alpha p_{\alpha}\delta_{ij} + 2\hat{\mu}_{\alpha}\hat{d}_{ij} \tag{2.42}$$

where p_α is the macroscopic fluid pressure, $\hat{\mu}_\alpha$ is the macroscopic viscosity coefficient (depends on fluid content) and $\hat{\mathbf{d}}$ is the macroscopic rate of deformation. Fluid content α, in front of pressure term occurs since it should produce a force acting on the fluid phase, averaged over the whole area of elementary volume.

The last term in equation (2.37) represents the resistance of a solid phase present in averaged volume. Taking into account thermodynamic considerations, Hassanizadeh and Gray [1980] showed that this term can be divided into a reversible and a dissipative part:

$$\langle\rho_\alpha\rangle\overline{\mathfrak{t}}^{\alpha\beta} = p_\alpha\nabla\alpha + \mathbf{R}\overline{\mathbf{v}}_\alpha \tag{2.43}$$

where the dissipative part is linearly expanded around the equilibrium (hydrostatic) point and $\mathbf{R}$ represents resistivity coefficient tensor. They also showed that $-\mathbf{R} \geq 0$.

It is generally accepted that viscous forces are much smaller in comparison with solid resistance and therefore can be neglected. Assuming the fluid as incompressible, the intrinsic average of the density equals the intrinsic density of the fluid, which in turn means

that $\langle \rho_\alpha \rangle^\alpha = \rho_\alpha = \langle \rho_\alpha \rangle / \alpha$. Neglecting, in addition, the inertial effects, equation (2.37) under steady conditions can be expressed as:

$$0 = \alpha \rho_\alpha \overline{\mathbf{f}} - \alpha \nabla p_\alpha + \mathbf{R} \overline{\mathbf{v}}_\alpha \tag{2.44}$$

or, in the component form:

$$q_{\alpha i} = -\frac{k_{ij}}{\mu_\alpha} (\nabla_j p_\alpha - \rho_\alpha f_j) \tag{2.45}$$

where $\mathbf{k}/\mu_\alpha = -\alpha^2/\mathbf{R}$, under condition that $-\mathbf{R}$ is invertible and $\mathbf{q}_\alpha = \alpha \overline{\mathbf{v}}_\alpha$. Obtained equation (2.45) has the same form as the Darcy law equation (2.40).

2.3.3 High velocity flow in porous media

The limitations of Darcy law are well known [e.g. Bear, 1972]. It is valid for low Raynolds numbers, where inertial effects are negligible. As velocity increases, the inertial effects increase, and in turn, deviations from Darcy law become more significant. In the early investigations, this deviation was prescribed to the turbulence by analogy with flow in pipes, where, after reaching specific Raynolds numbers, the hydraulic gradient has quadratic dependency in terms of velocity. However, experimental investigations revealed that deviation from Darcy law occurs significantly earlier in comparison with onset of turbulence (e.g. Wright, 1968; Bear 1972]. Therefore, this deviation is prescribed to the inertial effects, as a consequence of curvature of fluid velocity streamlines on the microscopic level. These effects on the macroscopic level are contained in the second term on the left side and the third term on the right side of equation (2.37).

An early and widely applied formula for high velocity flows in porous media was proposed by Forchheimer as:

$$J = aq + bq^2 \tag{2.46}$$

where J represents the hydraulic gradient and a and b are the empirical coefficients. Many empirical relation, derived by other authors have the same form as the equation (2.46) [e.g. Ergun, 1952]. Similar relation is also reported by several authors, based on the theoretical work [Irmay, 1958; Bachmat, 1965; Ahmed and Sunada, 1969].

Cvetkovic [1986] has conducted a similar volume averaging procedure as other authors in order to obtain macroscopic balance equations. As he pointed out, the form of

obtained inertial terms in equation (2.37) is not sufficiently appropriate for theoretical explanation of origins of microscopic inertial effects, as well as for deriving equation (2.46) from obtained macroscopic momentum balance equation. Instead of variation of microscopic velocity as given in equation (2.24), he considered variation of velocity magnitude, as well as microscopic variation of velocity direction:

$$v = \overline{v} + \tilde{v} \tag{2.47}$$

$$\delta_k = \overline{\delta}_k + \tilde{\delta}_k \tag{2.48}$$

where $v = |\mathbf{v}|$ and $\delta_k (k = 1, 2, 3)$ are cosines of angles between vector direction and reference unit vectors ($v_k = v\delta_k$).

In this case, volume averaging of acceleration terms gives additional terms, based on which he could conclude that inertial forces arise [Cvetkovic, 1986]:

- due to local velocity changes,
- due to microscopic curvature of streamlines, and
- due to difference of macroscopic and microscopic velocity magnitude.

Probably, the most important conclusion of his research is that coefficient b in quadratic term of equation (2.46) is not a material property of porous media, as in the case of coefficient a. In fact, it also depends on macroscopic velocity field. This point is usually neglected in numerical modeling of this type of flows, since this dependence is probably not possible to establish.

2.4 Summary

Volume averaging procedure has obtained macroscopic governing equations of multiphase flow (equations (2.22) and (2.37)). These equations are valid for a general case of multiphase flow, however, in many practical cases it is possible to introduce some simplifications. For the case of incompressible and immiscible flow, these equations can be written in a component form for each phase as:

mass balance equation:

$$\frac{\partial \alpha}{\partial t} + \frac{\partial}{\partial x_j}(\alpha V_{\alpha j}) = 0 \tag{2.49}$$

momentum balance equation:

$$\frac{\partial(\alpha V_{\alpha i})}{\partial t} + \frac{\partial\left(\alpha V_{\alpha i} V_{\alpha j}\right)}{\partial x_j} = -\frac{\alpha}{\rho_\alpha}\frac{\partial p_\alpha}{\partial x_i} - \alpha g \frac{\partial x_3}{\partial x_i} + \nu_\alpha \frac{\partial(\alpha \tau_{ij}^\alpha)}{\partial x_j} + F_{\alpha i} \tag{2.50}$$

where α is the phase volumetric content, $V_{\alpha i}$ is the mass averaged velocity (for the convenience, the overbars will be omitted onward), ν_α is the kinematic viscosity of the fluid, $F_{\alpha i}$ is the macroscopic resistance force in the i-th direction comprising the force exerted by the other phases in the system and microscopic inertial effects, averaged over the REV.

It is shown that equation (2.50) can be reduced to the Darcy law, after neglecting inertial and viscous terms and after linear expansion of the resistance term.

Equations (2.49) and (2.50) will be numerically discretized in the following chapter.

Chapter 3

Development of the numerical model

3.1 Preliminaries

In this chapter, the development of numerical model for simulation of single phase flow is presented and in the next chapter, the same model is extended to two-phase flows. Since the flow in porous media is also considered under assumption that solid phase is stagnant and rigid, in that case the models could be also considered as two, or three phase models, respectively.

The models developed in this study basically rely on the MAC (Marker and Cell) method, the first method proposed for numerical integration of Navier-Stokes equations for two-dimensional flows with free surface boundary [Welch *et al.*, 1965; Harlow and Welch, 1965], and later applied for simulation of three-dimensional flow domains [Hirt and Cook, 1972]. In the original MAC method, pressure field is obtained from the Poisson equation, in which the source term is function of velocity field, formulated in order to satisfy the incompressibility condition. From obtained pressure field, the velocity field at the new time step is explicitly calculated from Navier-Stokes equations. At the end of the time step, the non-material particles are convected in order to trace the movement of the free surface.

The Poisson equation for pressure field required a special care of boundary conditions in the original MAC method. This inconvenience was significantly improved in the later

versions of the MAC method. For example, in SMAC (Simplified MAC) method by Amsden and Harlow [1970], or HSMAC (Highly Simplified MAC) method [Hirt and Cook, 1972], which was inspired by the work of Chorin [1968] and Viecelli [1971]. In the latter method, the solution of Poisson equation is completely avoided by introduction of an iterative procedure in which the both, pressure and velocity fields are iteratively updated until the incompressibility condition is achieved. This numerical scheme is used in the thesis, and will be described in more detail in this chapter.

3.2 Discretization of governing equations

Following the HSMAC method, governing equations (2.49 and 2.50) will be discretized by the finite volumes, with staggered arrangement of hydraulic variables. This means that velocity components are defined at the cell boundaries and scalar quantities (pressure, phase contents, concentrations, etc.) are defined at the cell centers (Figure 3.1). The flow domain is divided on the grid cells by planes parallel to the coordinate axes. It is generally accepted that staggered arrangement is more accurate in comparison with ordinary grid arrangements, and that conservation of extensive quantities (mass, momentum, etc.) is more easily accomplished. The staggered arrangement is also convenient in terms of imposing different types of boundary conditions [Ferziger, 1987].

It should be noted that control volumes, over which the specific terms in governing equations are integrated, do not necessarily need to coincide with the grid volumes, as shown in Figure (3.2). For the momentum equations, control volumes are shifted for half of the cell size, so that corresponding velocity comes into the center of the control volume.

The continuity equation (2.49) could be discretized as follows:

$$\frac{\partial \alpha}{\partial t} \approx \frac{\alpha^{n+1} - \alpha^{n}}{\Delta t} \tag{3.1}$$

$$\frac{\partial}{\partial x_j}(\alpha V_{\alpha j}) \approx \frac{(\alpha V_{\alpha 1})_D - (\alpha V_{\alpha 1})_U}{\Delta x_1} + \frac{(\alpha V_{\alpha 2})_D - (\alpha V_{\alpha 2})_U}{\Delta x_2} + \frac{(\alpha V_{\alpha 3})_D - (\alpha V_{\alpha 3})_U}{\Delta x_3} \tag{3.2}$$

or more precisely:

$$\frac{1}{\Delta \mathbf{V}} \int_{\Delta \mathbf{V}} \frac{\partial}{\partial x_j}(\alpha V_{\alpha j}) d\mathbf{V} = \frac{1}{\Delta \mathbf{V}} \int_{A} (\alpha V_{\alpha j}) n_j dA \approx \frac{(\alpha V_{\alpha 1})_D - (\alpha V_{\alpha 1})_U}{\Delta x_1}$$

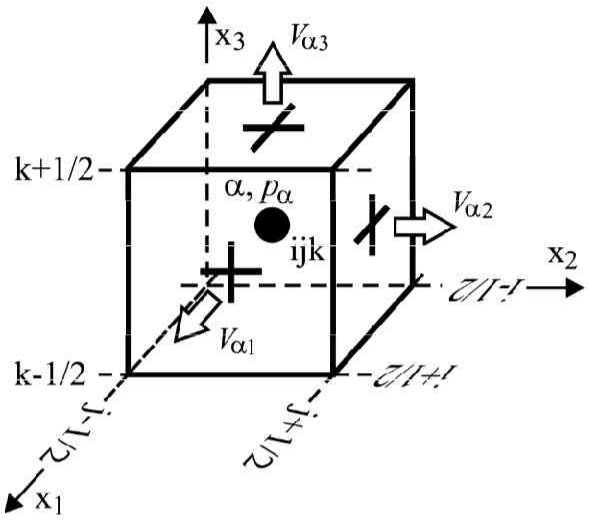

Figure 3.1: Staggered arrangement of hydraulic variables

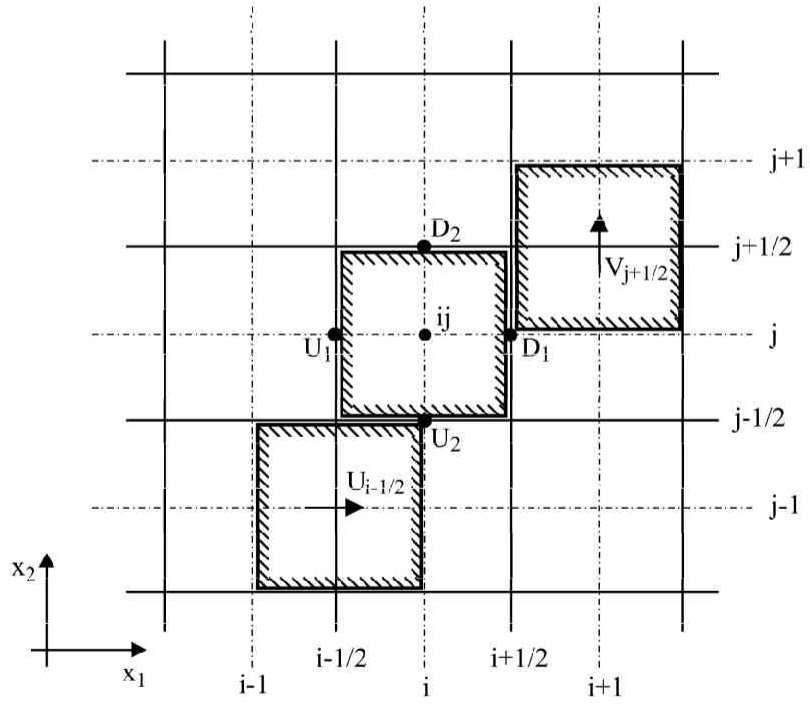

Figure 3.2: Control volumes for the mass balance and momentum equations (2D-case)

$$+\frac{(\alpha V_{\alpha 2})_D - (\alpha V_{\alpha 2})_U}{\Delta x_2} + \frac{(\alpha V_{\alpha 3})_D - (\alpha V_{\alpha 3})_U}{\Delta x_3} \tag{3.3}$$

where n and $n+1$ denote current and the next time step, respectively, and $\Delta \mathbf{V}$ is the control volume. Subscripts D and U denote fluxes through downward and upward face of the control volume, respectively, considering the orientation of the coordinate axes.

It can be seen that α, in order to estimate fluxes over the boundary surfaces in equation (3.3), has to be approximated at the cell boundaries from the values at the cell centers, where it is defined. There are several options to choose an appropriate value of α. It could be chosen by simple averaging; however, it is well known that central differencing in conjunction with explicit Euler's method for time integration produce unconditionally unstable scheme. In the case of different time integration scheme, central differencing can produce oscillations under certain conditions.

Probably the most often used scheme which avoids the oscillations produced by central differencing is so called upwind scheme. Approximated value of convected quantity (in this case α) depends on direction of velocity component:

$$(\alpha V_{\alpha 1})_D = \begin{cases} \alpha_{ijk} V_{\alpha i+\frac{1}{2}} & \text{if} \quad V_{\alpha i+\frac{1}{2}} > 0 \\ \alpha_{i+1jk} V_{\alpha i+\frac{1}{2}} & \text{if} \quad V_{\alpha i+\frac{1}{2}} < 0 \end{cases} \tag{3.4}$$

$$(\alpha V_{\alpha 1})_U = \begin{cases} \alpha_{i-1jk} V_{\alpha i-\frac{1}{2}} & \text{if} \quad V_{\alpha i-\frac{1}{2}} > 0 \\ \alpha_{ijk} V_{\alpha i-\frac{1}{2}} & \text{if} \quad V_{\alpha i-\frac{1}{2}} < 0 \end{cases} \tag{3.5}$$

and similarly for the other flux directions.

The upwind scheme is first-order accurate and its error contains a significant diffusion term, with artificial viscosity of the order $V\Delta x(1-C)/2$, where $C = V\Delta t/\Delta x$ is the Courant number. Its smoothing effect is especially pronounced in the case when the flow is at some angle to the grid (the most significant at 45° angle). However, owing to its stability, it is extensively used in the engineering practice. For the Euler's method of time integration, the upwind scheme is stable under Courant-Friedrich-Lewy condition:

$$CFL = \left(\frac{|V_i|}{\Delta x_i} + \frac{|V_j|}{\Delta x_j} + \frac{|V_k|}{\Delta x_k} \right) \Delta t \leq 1 \tag{3.6}$$

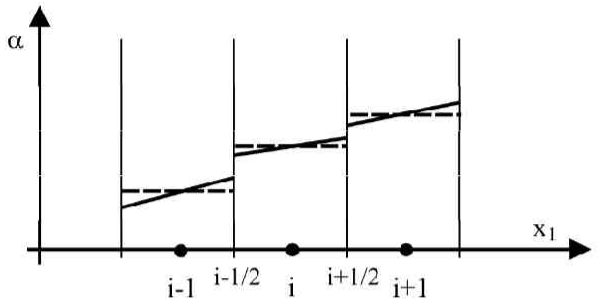

Figure 3.3: Distribution of the advected quantity in the computational cell: dashed line represents a constant approximation and the continuous line represents a linear approximation

Artificial diffusion, introduced by the upwind (or upstream) scheme is unacceptable in the simulations of multiphase flows, where the sharp boundaries between the phases exist. This leads toward higher order schemes. One of them, the MUSCL (Monotone Upstream-centered Scheme for Conservation Laws), with a TVD (Total Variation Diminishing) condition is used in the presented model. This scheme will be briefly explained here.

3.2.1 Discretization of the convective term by higher order scheme

In the upwind scheme, it is implicitly assumed that value of the convected property is constant in the computational cell. Assuming its value changing linearly, we come to the second-order spatial accuracy. It is obvious that, in order to establish this linearity, we need at least two cell averaged values (Figure 3.3). Similarly, the third-order spatial accuracy would be obtained if the change of convected quantity would be represented as a quadratic function of space. A MUSCL (after the name of code, developed by Van Leer [1979]) approach imply variable extrapolation of averaged cell values, providing this way a higher-order accuracy. Unfortunately, it is shown that simple replacement of first-order upwind scheme by higher-order upwind scheme leads to similar deficiencies as encountered with central scheme, i.e. oscillations around discontinuities. In addition, it can be theoretically shown that linear, second-order upwind schemes always generate oscillations [Enquist and Osher, 1981]. Therefore, an additional treatment is required.

Harten [1983] introduced the criterion of bounded total variation in order to ensure that oscillations are not generated by the numerical scheme. Here, the total variation, at the

current time step, is defined as:

$$TV(\alpha^n) = \sum_j |\alpha^n_{j+1} - \alpha^n_j| \tag{3.7}$$

with condition that numerical scheme is a TVD scheme if:

$$TV(\alpha^{n+1}) \leq TV(\alpha^n) \tag{3.8}$$

In other words, a TVD condition ensures that scheme is a monotonicity preserving, which means that monotonicity is preserved during the solution time evolution and oscillations can not occur. It can be easily shown that first-order upwind scheme satisfies the condition (3.8) for $C \leq 1$, and therefore it is a TVD scheme.

The value of the quantity (α) at the cell boundaries from the left and the right side can be approximated as [Hirsch, 1990]:

$$\alpha^L_{i+\frac{1}{2}} = \alpha_i + \frac{\epsilon}{4}\left[(1-\kappa)\frac{\alpha_i - \alpha_{i-1}}{\Delta x_{i-\frac{1}{2}}} + (1+\kappa)\frac{\alpha_{i+1} - \alpha_i}{\Delta x_{i+\frac{1}{2}}}\right]\Delta x_i \tag{3.9}$$

$$\alpha^R_{i+\frac{1}{2}} = \alpha_{i+1} \quad \frac{\epsilon}{4}\left[(1 \quad \kappa)\frac{\alpha_{i+2} - \alpha_{i+1}}{\Delta x_{i+\frac{3}{2}}} \; | \; (1 \; | \; \kappa)\frac{\alpha_{i+1} - \alpha_i}{\Delta x_{i+\frac{1}{2}}}\right]\Delta x_{i+1} \tag{3.10}$$

where parameter ϵ determines the spatial accuracy. For $\epsilon = 0$, it is first-order approximation, and for $\epsilon = 1$, the scheme is of higher order. Similarly, parameter κ determines higher order accuracy. For example, in the case that $\kappa = 1/3$, (3.9) and (3.10) represent a third-order Taylor expansion, for $\kappa = 1/2$ a QUICK scheme [Leonard, 1979] can be obtained, which for constant space discretization can be written as:

$$\alpha_{i+\frac{1}{2}} = \begin{cases} \alpha^L_{i+\frac{1}{2}} = \frac{1}{2}(\alpha_i + \alpha_{i+1}) - \frac{1}{8}(\alpha_{i-1} + \alpha_{i-1} - 2\alpha_i) & \text{if} \quad V_{\alpha i+\frac{1}{2}} > 0 \\ \alpha^R_{i+\frac{1}{2}} = \frac{1}{2}(\alpha_i + \alpha_{i+1}) - \frac{1}{8}(\alpha_i + \alpha_{i+2} - 2\alpha_{i+1}) & \text{if} \quad V_{\alpha i+\frac{1}{2}} < 0 \end{cases} \tag{3.11}$$

$$\alpha_{i-\frac{1}{2}} = \begin{cases} \alpha^L_{i-\frac{1}{2}} = \frac{1}{2}(\alpha_{i-1} + \alpha_i) - \frac{1}{8}(\alpha_{i-2} + \alpha_i - 2\alpha_{i-1}) & \text{if} \quad V_{\alpha i-\frac{1}{2}} > 0 \\ \alpha^R_{i-\frac{1}{2}} = \frac{1}{2}(\alpha_{i-1} + \alpha_i) - \frac{1}{8}(\alpha_{i-1} + \alpha_{i+1} - 2\alpha_i) & \text{if} \quad V_{\alpha i \; \frac{1}{2}} < 0 \end{cases} \tag{3.12}$$

and similarly for other directions. This scheme is used for convective term in momentum equation in this thesis. In the case of $\kappa = -1$, we obtain a simple linear, one-sided extrapolation of nodal values on the cell boundary.

In the equations (3.9) and (3.10) the second therm on the right side brings higher order accuracy, but also produces eventual oscillations. In order to ensure the TVD condition,

a slope limiters can be introduced in those terms, having the role to restrict the amplitude of gradients:

$$\alpha^{L}_{i+\frac{1}{2}} = \alpha_i + \frac{\epsilon}{4}\left[(1-\kappa)\Psi^{+}_{i-\frac{1}{2}}\frac{\alpha_i - \alpha_{i-1}}{\Delta x_{i-\frac{1}{2}}} + (1+\kappa)\Psi^{-}_{i+\frac{1}{2}}\frac{\alpha_{i+1} - \alpha_i}{\Delta x_{i+\frac{1}{2}}}\right]\Delta x_i \tag{3.13}$$

$$\alpha^{R}_{i+\frac{1}{2}} = \alpha_{i+1} - \frac{\epsilon}{4}\left[(1-\kappa)\Psi^{-}_{i+\frac{3}{2}}\frac{\alpha_{i-2} - \alpha_{i+1}}{\Delta x_{i+\frac{3}{2}}} + (1+\kappa)\Psi^{+}_{i+\frac{1}{2}}\frac{\alpha_{i+1} - \alpha_i}{\Delta x_{i+\frac{1}{2}}}\right]\Delta x_{i+1} \tag{3.14}$$

where the limiters $\Psi^{\pm}_{i+\frac{1}{2}}$ are functions of ratio of consecutive gradients:

$$\Psi^{+}_{i+\frac{1}{2}} = \Psi\left(r^{+}_{i+\frac{1}{2}}\right) = \Psi\left(\frac{\alpha_{i+2} - \alpha_{i+1}}{\alpha_{i+1} - \alpha_i}\frac{\Delta x_{i+\frac{1}{2}}}{\Delta x_{i+\frac{3}{2}}}\right) \tag{3.15}$$

$$\Psi_{i+\frac{1}{2}} = \Psi\left(r_{i+\frac{1}{2}}\right) = \Psi\left(\frac{\alpha_i - \alpha_{i-1}}{\alpha_{i+1} - \alpha_i}\frac{\Delta x_{i+\frac{1}{2}}}{\Delta x_{i-\frac{1}{2}}}\right) \tag{3.16}$$

In order to simplify equations (3.13) and 3.14), the limiters $\Psi(r^L)$ and $\Psi(r^R)$ can be defined as:

$$\Psi\left(r^L\right) = \Psi\left(r^{+}_{i-\frac{1}{2}}\right) \tag{3.17}$$

$$\Psi\left(r^R\right) = \Psi\left(r^{-}_{i+\frac{3}{2}}\right) \tag{3.18}$$

and substituted to obtain:

$$\alpha^{L}_{i+\frac{1}{2}} = \alpha_i + \frac{\epsilon}{4}\left[(1-\kappa)\Psi\left(r^L\right) + (1+\kappa)r^L\Psi\left(\frac{1}{r^L}\right)\right]\frac{\alpha_i - \alpha_{i-1}}{\Delta x_{i-\frac{1}{2}}}\Delta x_i \tag{3.19}$$

$$\alpha^{R}_{i+\frac{1}{2}} = \alpha_{i+1} - \frac{\epsilon}{4}\left[(1-\kappa)\Psi\left(r^R\right) + (1+\kappa)r^R\Psi\left(\frac{1}{r^R}\right)\right]\frac{\alpha_{i+2} - \alpha_{i+1}}{\Delta x_{i\,|\,\frac{3}{2}}}\Delta x_{i+1} \tag{3.20}$$

Naturally, every function of the ratio r can not be a gradient limiter. A detailed analysis of required limiter properties is given, for example, in the work of Sweby [1984]. In short, to satisfy the TVD condition it is necessary that limiter has the following property:

$$0 \leq \Psi(r) \leq min(2r, 2) \tag{3.21}$$

The region defined by equation (3.21) on a $r - \Psi$ diagram is shown in Figure 3.4. In addition, in order to ensure a higher order accuracy a more restrictive condition can be established [Sweby, 1984]:

$$\Psi(r) = max(0, min(\beta r, 1), min(r, \beta)) \quad 1 \leq \beta \leq 2 \tag{3.22}$$

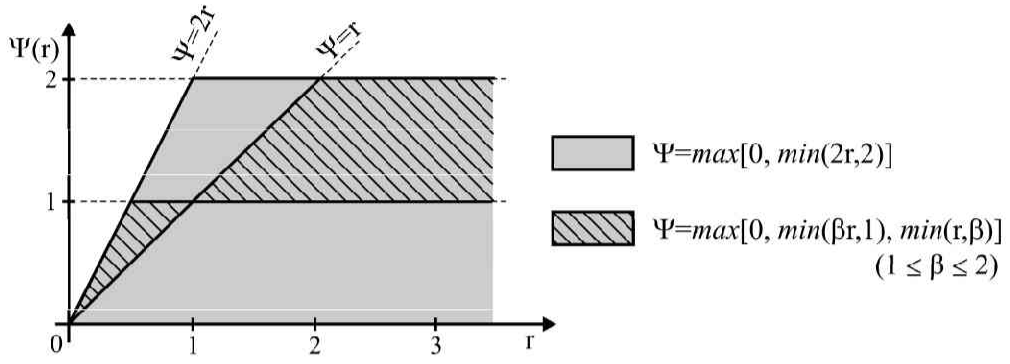

Figure 3.4: A limiter function region satisfying the TVD condition

for which the region on the $r - \Psi$ diagram is also shown in Figure (3.4). Some of the most frequently used limiters are shown in Figure 3.5. It can be seen that $\Psi(r) = minmod(1, r)$ limiter represents a lower boundary of marked region in Figure 3.4. Here, a *minmod* function is defined as:

$$minmod(a,b) = \begin{cases} a & if \quad |a| < |b| \quad and \quad ab > 0 \\ b & if \quad |a| > |b| \quad and \quad ab > 0 \\ 0 & if \quad ab < 0 \end{cases} \tag{3.23}$$

Considering definition, given by equation (3.23), an action of a *minmod* limiter becomes clear. It takes a smaller gradient for extrapolation of variable when consecutive gradients have the same sign. In the case that subsequent gradients change the sign, an ordinary upwind scheme is utilized, avoiding occurrence of oscillations.

Approximated values from equations (3.19) and (3.20) give the flux at the cell boundary, considering the velocity direction. In a general form, it can be written as:

$$(\alpha V_\alpha)_D = 0.5 \left[V_{\alpha i+\frac{1}{2}} \left(\alpha^L_{i+\frac{1}{2}} + \alpha^R_{i+\frac{1}{2}} \right) + |V_{\alpha i+\frac{1}{2}}| \left(\alpha^L_{i+\frac{1}{2}} - \alpha^R_{i+\frac{1}{2}} \right) \right| \tag{3.24}$$

$$(\alpha V_\alpha)_U = 0.5 \left[V_{\alpha i-\frac{1}{2}} \left(\alpha^L_{i-\frac{1}{2}} + \alpha^R_{i-\frac{1}{2}} \right) + |V_{\alpha i-\frac{1}{2}}| \left(\alpha^L_{i-\frac{1}{2}} - \alpha^R_{i-\frac{1}{2}} \right) \right| \tag{3.25}$$

with the same scheme for other flux directions.

Several gradient limiters are tested in this thesis for the case of two phase flow in porous media. Results and appropriate conclusions will be given in the section about model verification.

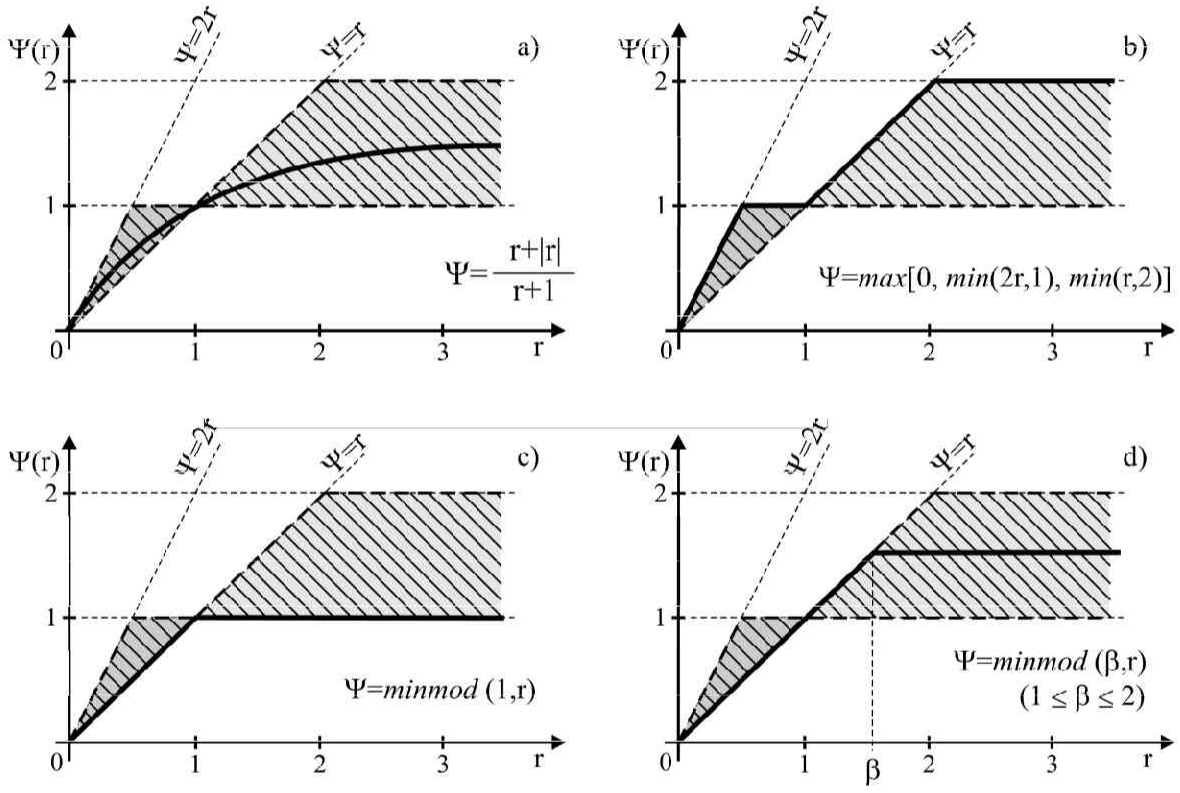

Figure 3.5: Some gradient limiters for second order extrapolation schemes: a) Van Leer's limiter; b) 'Superbee' limiter; c) 'minmod' limiter; d) Chakravarthy and Osher limiter

3.2.2 Discretization of momentum equation

Additional therms in momentum equations (2.50) which will be considered here, are the pressure, viscous and resistance term. Discretization of the pressure gradient term is straightforward for the staggered arrangement of variables:

$$\left(\frac{\partial p_\alpha}{\partial x_i}\right)_{i+\frac{1}{2}} \approx \frac{(p_\alpha)_{i+1} - (p_\alpha)_i}{\Delta x} \tag{3.26}$$

However, treatment of this term in curvilinear coordinate system requires a special attention, in order to avoid occurrence of false flows. This will be explained in the Chapter 7, where governing equation are discretized in generalized curvilinear coordinate system.

For the viscous term, it is necessary to evaluate gradients of velocities at the control volume boundaries. This is also straightforward, due to arrangement of hydraulic variables:

$$\begin{aligned}\frac{\partial}{\partial x_j}\left(\alpha\nu_\alpha\frac{V_{\alpha 1}}{\partial x_j}\right) \approx & \frac{\left(\alpha\nu_\alpha\frac{V_{\alpha 1}}{\partial x_1}\right)_{1D} - \left(\alpha\nu_\alpha\frac{V_{\alpha 1}}{\partial x_1}\right)_{1U}}{\Delta x_1} \\ & + \frac{\left(\alpha\nu_\alpha\frac{V_{\alpha 1}}{\partial x_2}\right)_{2D} - \left(\alpha\nu_\alpha\frac{V_{\alpha 1}}{\partial x_2}\right)_{2U}}{\Delta x_2} \\ & + \frac{\left(\alpha\nu_\alpha\frac{V_{\alpha 1}}{\partial x_3}\right)_{3D} - \left(\alpha\nu_\alpha\frac{V_{\alpha 1}}{\partial x_3}\right)_{3U}}{\Delta x_3}\end{aligned} \tag{3.27}$$

with the same for other velocity components. Figure (3.2) shows the position of evaluation of gradients for the 2-D case.

The resistance term F_i is usually, depending on the type of flow, some function of velociy (linear or nonlinear). In some cases it dominates in the momentum equation and therefore it should be treated implicitly, due to stability considerations. In the simulation of flow in porous media, numerical experiments revealed that in the case of explicit evaluation of this term, required time step was of the order of hydraulic permeability values. If, in general case, this term can be expressed as $F_i = C_i V_{\alpha i}$, where C_i is the constant, in the numerical model it is evaluated as:

$$F_i = C_i \frac{1}{2}\left(V_{\alpha i}^n + V_{\alpha i}^{n+1}\right) \tag{3.28}$$

or full-implicitly, which increases the allowed time step.

3.3 HSMAC iterative procedure

The original HSMAC method for numerical solution of Navier-Stokes equations is slightly adapted, due to existence of more than one phase and an additional resistance term in momentum equation (2.50). Here, the method will be presented for a general case of two-phase fluid (e.g. water and air) flow in porous media. Extension to saturated flow in porous media, or multi-phase flow in porous media is straightforward.

The method includes an iterative procedure which consists of two steps. In the first step predicted values of fluid fluxes are calculated from the discretized form of momentum equations:

$$(\alpha V_\alpha)^{n+1,r+1}\left(1+\Delta t\frac{C_\alpha}{2}\right)=(\alpha V_\alpha)^{n}\left(1-\Delta t\frac{C_\alpha}{2}\right)-\Delta t\Big[(pressure\ term)^{n+1,r}+(gravity\ term)^{n+1,r}+(inertia\ term)^{n+1}-(viscous\ term)^{n+1}\Big] \tag{3.29}$$

$$(\beta V_\beta)^{n+1,r+1}\left(1+\Delta t\frac{C_\beta}{2}\right)=(\beta V_\beta)^{n}\left(1-\Delta t\frac{C_\beta}{2}\right)-\Delta t\Big[(pressure\ term)^{n+1,r}+(gravity\ term)^{n+1,r}+(inertia\ term)^{n+1}-(viscous\ term)^{n-1}\Big] \tag{3.30}$$

where superscripts r and $r+1$ denote the current and the next iteration, respectively. The inertia and viscous terms at the new time step are estimated using the Adams-Bashforth scheme:

$$(term)^{n+1}=1.5(term)^{n}-0.5(term)^{n-1} \tag{3.31}$$

After obtaining predicted fluxes, the divergence for each discretization cell is computed as:

$$\begin{aligned}D^{r+1}=&\frac{(\alpha U_\alpha)^{n+1,r+1}_{i+\frac{1}{2}}-(\alpha U_\alpha)^{n+1,r+1}_{i-\frac{1}{2}}}{\Delta x_1}+\frac{(\alpha V_\alpha)^{n+1,r+1}_{j+\frac{1}{2}}-(\alpha V_\alpha)^{n+1,r+1}_{j-\frac{1}{2}}}{\Delta x_2}\\&+\frac{(\alpha W_\alpha)^{n+1,r+1}_{k+\frac{1}{2}}-(\alpha W_\alpha)^{n+1,r+1}_{k-\frac{1}{2}}}{\Delta x_3}+\frac{(\beta U_\beta)^{n+1,r+1}_{i+\frac{1}{2}}-(\beta U_\beta)^{n+1,r+1}_{i-\frac{1}{2}}}{\Delta x_1}\\&+\frac{(\beta V_\beta)^{n+1,r+1}_{j+\frac{1}{2}}-(\beta V_\beta)^{n+1,r+1}_{j-\frac{1}{2}}}{\Delta x_2}+\frac{(\beta W_\beta)^{n+1,r+1}_{k+\frac{1}{2}}-(\beta W_\beta)^{n+1,r+1}_{k-\frac{1}{2}}}{\Delta x_3}\end{aligned} \tag{3.32}$$

In the second step, the pressure of one phase (α or β) is corrected in order to vanish

the divergence, e.g.:

$$p_\alpha^{n+1,r+1} = p_\alpha^{n+1,r} + \delta p_\alpha^{r+1} = p_\alpha^{n+1,r} - \omega \frac{D^{r+1}}{\left(\frac{\partial D^{r+1}}{\partial p_\alpha}\right)} \tag{3.33}$$

where ω is the relaxation coefficient. The denominator in the second term on the right side of equation (3.33) can be derived, considering definition of the divergence (equation (3.32)) and expressions for phase fluxes in equations (3.29) and (3.30):

$$\begin{aligned}\left(\frac{\partial D^{r+1}}{\partial p_\alpha}\right) = \Delta t \Bigg[& \frac{\left(\frac{\alpha}{M_\alpha}\right)_{i-\frac{1}{2}} + \left(\frac{\alpha}{M_\alpha}\right)_{i+\frac{1}{2}}}{(\Delta x_1)^2} + \frac{\left(\frac{\alpha}{M_\alpha}\right)_{j-\frac{1}{2}} + \left(\frac{\alpha}{M_\alpha}\right)_{j+\frac{1}{2}}}{(\Delta x_2)^2} \\ & + \frac{\left(\frac{\alpha}{M_\alpha}\right)_{k\ \frac{1}{2}} + \left(\frac{\alpha}{M_\alpha}\right)_{k\ |\ \frac{1}{2}}}{(\Delta x_3)^2} \Bigg] + \Delta t \Bigg[\frac{\left(\frac{\beta}{M_\beta}\right)_{i\ \frac{1}{2}} + \left(\frac{\beta}{M_\beta}\right)_{i\ |\ \frac{1}{2}}}{(\Delta x_1)^2} \\ & + \frac{\left(\frac{\beta}{M_\beta}\right)_{j-\frac{1}{2}} + \left(\frac{\beta}{M_\beta}\right)_{j+\frac{1}{2}}}{(\Delta x_2)^2} + \frac{\left(\frac{\beta}{M_\beta}\right)_{k-\frac{1}{2}} + \left(\frac{\beta}{M_\beta}\right)_{k+\frac{1}{2}}}{(\Delta x_3)^2} \Bigg] \frac{\rho_\alpha}{\rho_\beta}\end{aligned} \tag{3.34}$$

where M_α and M_β are defined as:

$$M_\alpha = 1 + \Delta t \frac{C_\alpha}{2} \quad M_\beta = 1 + \Delta t \frac{C_\beta}{2} \tag{3.35}$$

Momentum equations for different phases are coupled through the pressure terms, i.e. the constitutive relation for pressure difference between the phases is needed. For the case of air-water flow in porous media, this difference is called a capillary pressure for which several empirical relations can be found in the literature. If, for example, the pressure of the fluid α is calculated from equation (3.33), then the pressure of fluid β is calculated from the constitutive relation. For the numerical cells, in which both fluids exist , formally it has no importance for which fluid pressure will be calculated from equation (3.33), and which one will be calculated from the constitutive relation. However, efficiency of the iterative process may depend on this choice. Here, one can introduce a lower limit for the phase content, over which pressures of that fluid will be updated from equation (3.33). In some cases this produced convergence problems if the limit is exceeded during the iterations. Therefore, in the presented model, two control values are used as a lower and upper limit (e.g. for the phase α: α_B and α_T), with a simple control structure before each iteration [Jacimovic *et al.*, 2006]:

IF [$(\alpha^r > \alpha_B$ *.and.* $\alpha^{r-1} > \alpha_B)$ .or. $\alpha^r > \alpha_T$] THEN

1) Pressure p_α from the equation (3.33)

2) Pressure p_β from the constitutive relation for pressures

ELSE

1) Pressure p_β from the equation (3.33)

2) Pressure p_α from the constitutive relation for pressures

ENDIF

In the case that pressure for the β fluid is first corrected, equation (3.34) is slightly changed:

$$\left(\frac{\partial D^{r-1}}{\partial p_\beta}\right) = \Delta t \left[\frac{\left(\frac{\alpha}{M_\alpha}\right)_{i-\frac{1}{2}} + \left(\frac{\alpha}{M_\alpha}\right)_{i+\frac{1}{2}}}{(\Delta x_1)^2} + \frac{\left(\frac{\alpha}{M_\alpha}\right)_{j-\frac{1}{2}} + \left(\frac{\alpha}{M_\alpha}\right)_{j+\frac{1}{2}}}{(\Delta x_2)^2} + \frac{\left(\frac{\alpha}{M_\alpha}\right)_{k-\frac{1}{2}} + \left(\frac{\alpha}{M_\alpha}\right)_{k+\frac{1}{2}}}{(\Delta x_3)^2} \right] \frac{\rho_\beta}{\rho_\alpha} + \Delta t \left[\frac{\left(\frac{\beta}{M_\beta}\right)_{i-\frac{1}{2}} + \left(\frac{\beta}{M_\beta}\right)_{i+\frac{1}{2}}}{(\Delta x_1)^2} + \frac{\left(\frac{\beta}{M_\beta}\right)_{j-\frac{1}{2}} + \left(\frac{\beta}{M_\beta}\right)_{j+\frac{1}{2}}}{(\Delta x_2)^2} + \frac{\left(\frac{\beta}{M_\beta}\right)_{k-\frac{1}{2}} + \left(\frac{\beta}{M_\beta}\right)_{k+\frac{1}{2}}}{(\Delta x_3)^2} \right] \tag{3.36}$$

Above described iterations are repeated until the given divergence criteria is satisfied, i.e. $|D^{r+1}| < criteria$. A graphical representation of the iterative procedure is shown in Figure 3.6.

The procedure can be now easily adapted for different types of flows. If considered flow is saturated flow in the fixed porous media, then α is substituted by the porosity, and β is zero. If the free, single fluid flow is considered, then α equals one. In this case, there is no resistance term in momentum equations and therefore, the divergence and the pressure correction terms become a familiar expressions from the standard HSMAC method:

$$D^{r+1} = \frac{U^{n+1,r+1}_{i+\frac{1}{2}} - U^{n+1,r+1}_{i-\frac{1}{2}}}{\Delta x_1} + \frac{V^{n+1,r+1}_{j+\frac{1}{2}} - V^{n+1,r+1}_{j-\frac{1}{2}}}{\Delta x_2} + \frac{W^{n+1,r+1}_{k+\frac{1}{2}} - W^{n+1,r+1}_{k-\frac{1}{2}}}{\Delta x_3} \tag{3.37}$$

$$p^{n+1,r+1} = p^{n+1,r} + \delta p^{r+1} = p^{n+1,r} - \omega \frac{D^{r+1}}{2\Delta t \left(\frac{1}{(\Delta x_1)^2} + \frac{1}{(\Delta x_2)^2} + \frac{1}{(\Delta x_3)^2}\right)} \tag{3.38}$$

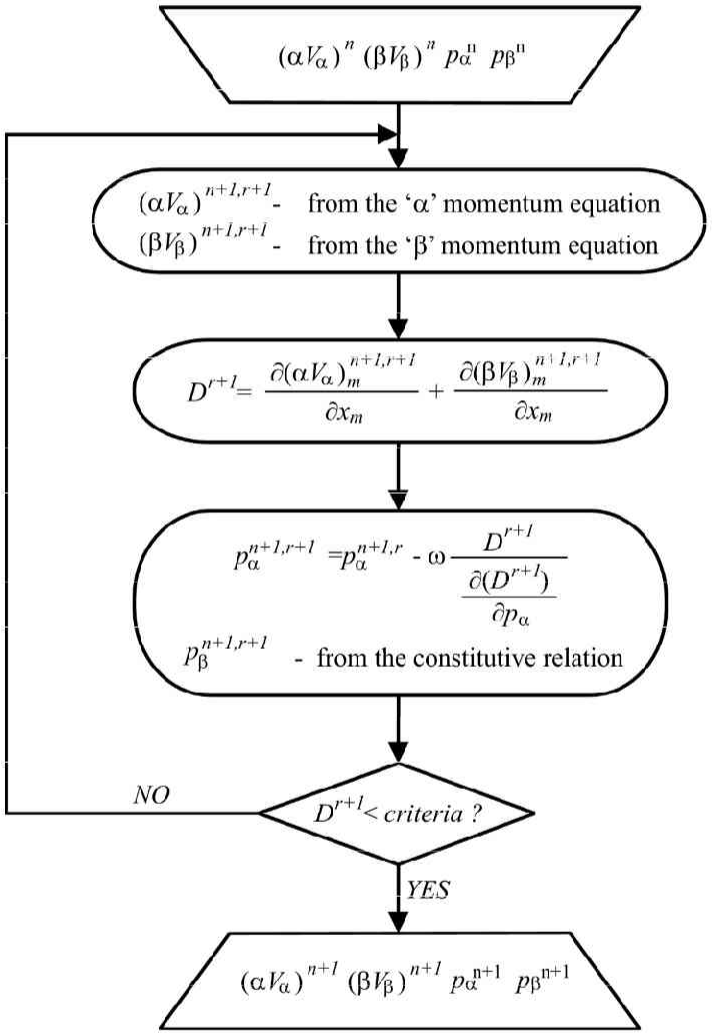

Figure 3.6: Iterative procedure for calculation of pressure and velocity field of two phase flow

3.4 Treatment of the free surface

In many flow problems, at least one of the domain boundaries represents a free fluid surface. After obtaining a velocity and pressure field by using an appropriate solver (such as HSMAC method), the position of the free surface has to be updated. In the original MAC method a massless markers are used, for which the velocity vectors are interpolated from the cell boundaries, and used for calculation of their new position. Cells containing markers and which are surrounded with empty cells, contain a free surface. It is obvious that this approach suffers from large amount of additional memory required to keep a track of each marker and additional computational time required to calculate a new position for the each marker.

Hirt and Nichols [1981] proposed a Volume of Fluid (VOF) method for free surface tracking. This was not the first proposed method for volume tracking [Kothe *et al.*, 1996], however, it is probably the most often used. In the method, a volume fraction occupied by the fluid is introduced as a new property and which is advected at each time step. Exact geometry of the free surface inside the cell is not known; it is reconstructed under conservation condition that free surface truncates the cell by the volume equal to the volume of fluid property. The method has been later significantly improved [e.g. Youngs, 1982; Kothe *et al.*, 1996; Rider and Kothe, 1998]. The main accuracy improvement comes from the linear reconstruction of the surface inside the cell, instead the original constant approximation. Nevertheless, the original method has been widely used with satisfactorily results in many flow problems and therefore will be used in this study. An exquisite historical review of volume tracking methods is given by Rider and Kothe [1998].

Outline of the VOF method

If 'f' denotes the volume fraction occupied by the fluid, then for a given flow field $\mathbf{v}$, a standard advection equation governs the time evolution of f:

$$\frac{df}{dt} = \frac{\partial f}{\partial t} + \mathbf{v} \cdot \nabla f = 0 \tag{3.39}$$

where d/dt denotes the material derivative. Considering the incompressible flow field ($\nabla \cdot \mathbf{v} = 0$),

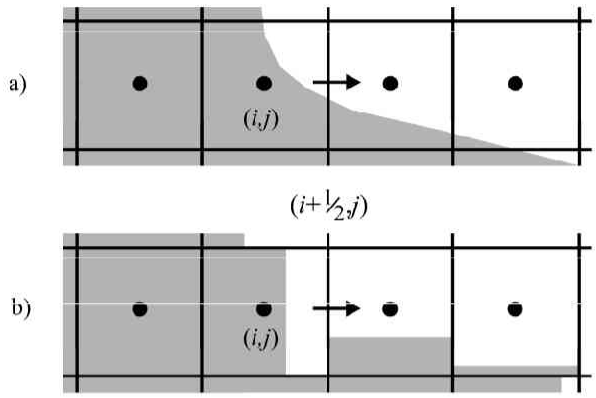

Figure 3.7: VOF approximation of the free surface: a) actual free surface, b) VOF approximation

(3.39) can be expressed in conservative form as:

$$\frac{\partial f}{\partial t} + \nabla \cdot (\mathbf{v} f) = 0 \tag{3.40}$$

Even application of higher order, high resolution numerical schemes to equation (3.40) can not completely avoid a numerical dissipation. Therefore, the VOF method introduces the so called geometric solution as appropriate combination of upstream and downstream first order schemes in order to preserve discontinuous nature of the f quantity and sharp definition of the free surface.

Considering a 2D case, the free surface is approximated as shown in Figure 3.7. The truncation line can be either parallel to x_1 or x_2 coordinate. Calculation of the fluid volume f, i.e. whether the upstream or downstream value will be used in order to calculate the flux, depends on orientation of the surface with respect of velocity direction. According to the method, if the surface in the upstream cell is normal to the velocity vector, then the downstream value is used; if it is parallel, the upstream value is utilized. In addition, if downstream cell is empty, or upstream cell of current cell is empty, again the downstream value is used. This ensures that fluid can not exit the cell, until it is full. Described calculation of the volume flux, at the cell boundary in x_1 direction can be formulated as [Hirt and Nichols, 1981]:

$$(Uf) = min\left(f^*|U| + CF, f_{upstream} \cdot \Delta x_1\right) \Delta x_2 \, \Delta x_3$$

$$CF = max\left[(1 - f^*)|U| - (1 - f)_{upstream} \cdot \Delta x_1,\, 0\right] \tag{3.41}$$

where f^* is upstream or downstream value of f, depending on the surface orientation. The *min* operator ensures that only available amount of fluid in the upstream cell can be transfered, and the *max* operator ensures that additional amount of fluid is added in the case that there is not enough void in the upstream cell to be transported. The same can be applied to other directions. After calculation of fluxes, a f value is updated for each 'active' cell, where active cell is considered as cell which contains the free surface $(0 < f < 1)$ and all neighbor cells. Some additional adjustments are also required in order to avoid occurrence of f values larger than one, or less than zero. The complete VOF procedure can be described through the following steps:

1. Construction of free surface truncation line for the cells with $(0 < f < 1)$, depending on the neighbor f gradients.

2. Calulation of the boundary fluxes for each 'active' cell.

3. Calculation of the new f values for each 'active' cell.

4. Cells with $f > (1 - \epsilon)$ are considered as full cells $(f = 1)$, with changing status of all empty, neighbour cells by adding a small amount of fluid volume $(f = \epsilon)$. Here, ϵ is a small number, usually $\epsilon = 10^{-6}$.

5. Cells with $f < \epsilon$ are considered as empty cells $(f = 0)$, with changing status of all full, neighbour cells by subtracting a small amount of fluid $(f = 1 \quad 1.1\epsilon)$.

6. Calculation of boundary pressure in the free surface cells by interpolation/extrapolation of pressure from the neighboring full cell and imposed pressure on the free surface (usually zero pressure). The full cell, which is used for pressure interpolation/extrapolation, is chosen to be normal to the free surface.

Application of the VOF method to the flow in porous media requires additional adaption. In the advection equation (3.40), the porosity has to be involved:

$$\frac{\partial(nf)}{\partial t} + \nabla \cdot (\mathbf{v}\, nf) = 0 \tag{3.42}$$

where n is the porosity of the media and nf represents actual fluid content. In this case f denotes a fluid saturation. At the boundaries between porous media and free fluid flow, the model takes the less value of the porosity between two neighboring cells to calculate the flux, meaning that no more fluid can cross the interface than upstream cell can physically provide or downstream cell can receive. The same is applied in the case of heterogeneous porous media, at the interfaces between different porosities.

3.5 Validation of the numerical model

In order to validate developed numerical model, it will be applied to different types of flows. First, the problem of free surface flow in homogeneous porous media is simulated, where the model is compared with the results of the finite element solution of Laplace equation, obtained after neglecting acceleration and viscous terms in momentum equation. This is also opportunity to examine the effects of acceleration in these conditions.

Next, model is applied to the well known Buckley-Leverett problem of two-phase flow in porous media [Buckley and Leverett, 1941], where the model results are compared with analytical solution of the problem. Existence of the sharp front between the phase saturations in this problem is utilized to test the model in terms of numerical dissipation effects, where several parameters are tested. Results obtained here are essential for the model applications, described in the following chapters.

Finally, model is applied to the 1D problem of water infiltration into the unsaturated soil, where it is compared with available semi-analytical solutions. The effect of air flow on the water infiltration could be analyzed by using the developed model.

3.5.1 Modeling of saturated, free surface flow in porous media

In order to verify the presented model with VOF method for free surface tracking, results are compared with results of finite element (FEM) numerical solution of governing equation for 2D Darcy flow (Laplace equation) for homogeneous, isotropic porous media in vertical plane. Models are applied on the problem of seepage through the vertical dam, after sudden decrease of downstream water level, as shown in Figure 3.8.

Outline of the FEM solution

This initial boundary value problem, for the rigid porous media considered here, can be described by the following set of equations [Neuman and Witherspoon, 1971]:

$$\frac{\partial}{\partial x_m}\left(K\frac{\partial h}{\partial x_m}\right) = 0 \qquad \text{on} \quad \Omega \tag{3.43}$$

$$h\left(x_m, 0\right) = h_0\left(x_m\right) \tag{3.44}$$

$$\xi\left(x_m, 0\right) = \xi_0\left(x_m\right) \tag{3.45}$$

$$h\left(x_m, t\right) = H_1\left(x_m, t\right) \qquad \text{on} \quad B_1 \tag{3.46}$$

$$h\left(x_m, \xi, t\right) = \xi\left(x_m\right) \qquad \text{on} \quad F \tag{3.47}$$

$$K\left(\frac{\partial h}{\partial x_m}\right) n_m = -\phi\frac{\partial \xi}{\partial t} n_2 \qquad \text{on} \quad F \tag{3.48}$$

$$K\left(\frac{\partial h}{\partial x_m}\right) n_m = 0 \qquad \text{on} \quad B_2 \tag{3.49}$$

$$h = x_2 \qquad \text{on} \quad S \tag{3.50}$$

where h is the total head, K is the hydraulic permeability, ξ is the elevation of the free surface from the bottom boundary, H_1 is the prescribed head, Ω is the flow domain, B_1 is prescribed head boundary, B_2 is prescribed flux boundary (zero flux is used), F is the free surface boundary and S is the seepage face. It is important to note that equation (3.43) can be derived from the momentum equation (2.50) and continuity equation (2.49), where acceleration and viscous terms are neglected and the drag term is expressed according to the Darcy law.

To obtain a system of algebraic equations with total heads as unknows, the Galerkin's method of weighted residuals is applied to the system (3.43 - 3.50) [e.g. Pinder and Gray, 1977], with flow domain discretized by linear, quadrilateral elements. Position of the free surface at the new time step is calculated by iteration, where each iteration consists of two steps. At the first step, equation (3.43) is solved for prescribed head conditions at the free surface and seepage face from the previous iteration. At the end of this step, nodal fluxes on the seepage face are calculated and used at the second step together with fluxes on the free surface boundary from equation (3.48). In the second step, (3.43) is solved again, but now with prescribed fluxes on the free surface and seepage face. At the end, the mesh is

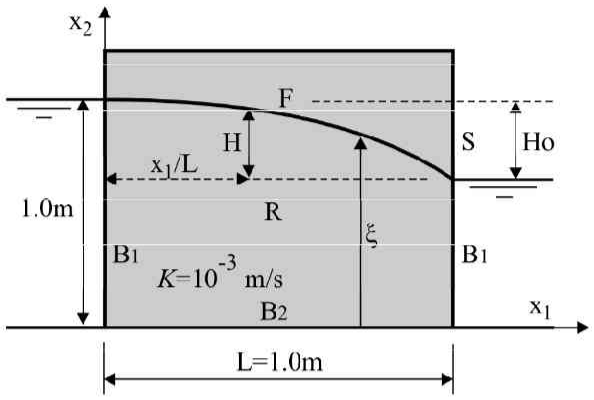

Figure 3.8: Modeling of seepage through the vertical dam: boundary conditions

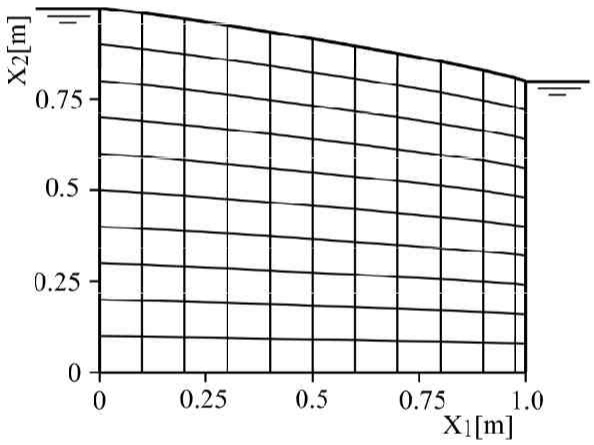

Figure 3.9: Seepage through the vertical dam: FEM mesh ($H_0 = 0.2m$)

deformed in order to satisfy condition expressed by equation (3.47). Iterations are repeated until the difference between calculated pressure head on the free surface and position of the free surface satisfy the given criteria. Figure 3.9 shows converged finite element mesh for one denivelation case. Finer discretization resulted to change of computed free surface levels by less than 1%.

Since the finite volume (FV) model is developed as three-dimensional, the two-dimensional domain is regularly discretized by 5cm x 5cm x 5cm volumes with 20x20x1 cells in x_1, x_2 and x_3 direction, respectively. Initially, the whole domain is saturated by the water.

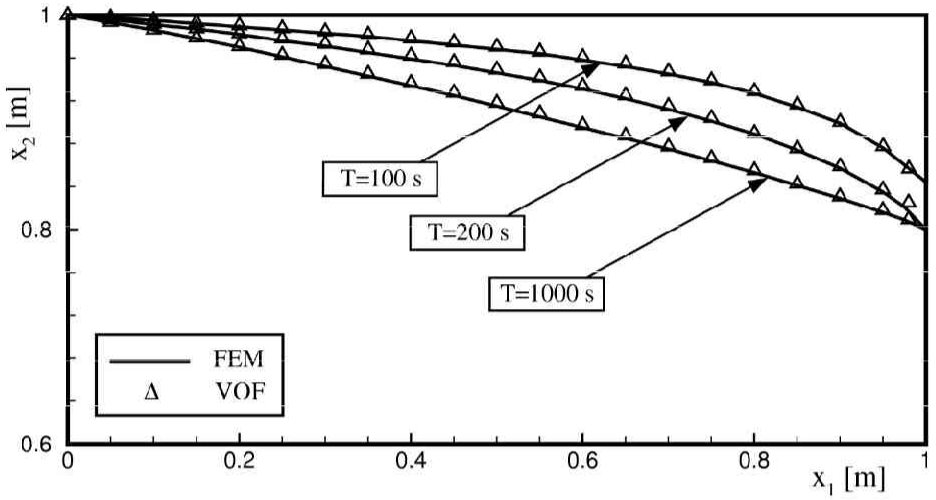

Figure 3.10: Comparison of calculated water levels ($H_0 = 0.2m$)

Results and discussion

Figures 3.10 and 3.11 show calculated transient surface positions for two cases of denivelation heights ($H_0 = 0.2m$ and $H_0 = 0.4m$). Good agreement between the results suggests that (VOF) method can adequately track the free surface movement in the porous media. Inertial effects, in case of flow with small gradients is negligible, but as gradient increases these terms become more significant and the calculated surface levels slightly differ from (FEM) solution (Figure 3.12). In such cases, this produces better reconstruction of free surface boundary. As it was described above, FEM approach requires special treatment of the seepage face. Here, particular problem represents intersection point of free surface and seepage face boundary, because calculation of nodal flux at this point include both boundaries and error has effect on the whole domain. Several approximations are suggested to treat this problem. One of them is to place this point in the line with the two nearest nodes on F [Neuman and Witherspoon, 1971], which is used here. In FV model, the seepage face boundary is naturally included by imposing zero pressure at the cells on this boundary.

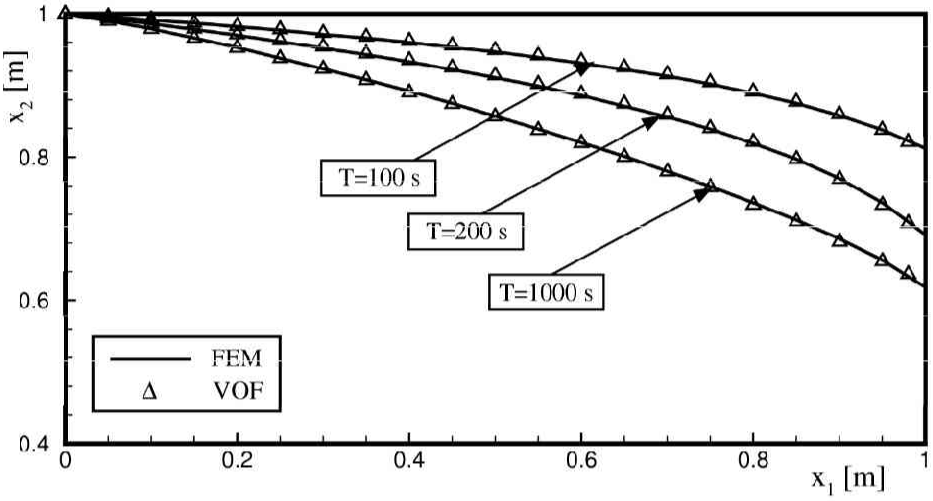

Figure 3.11: Comparison of calculated water levels ($H_0 = 0.4m$)

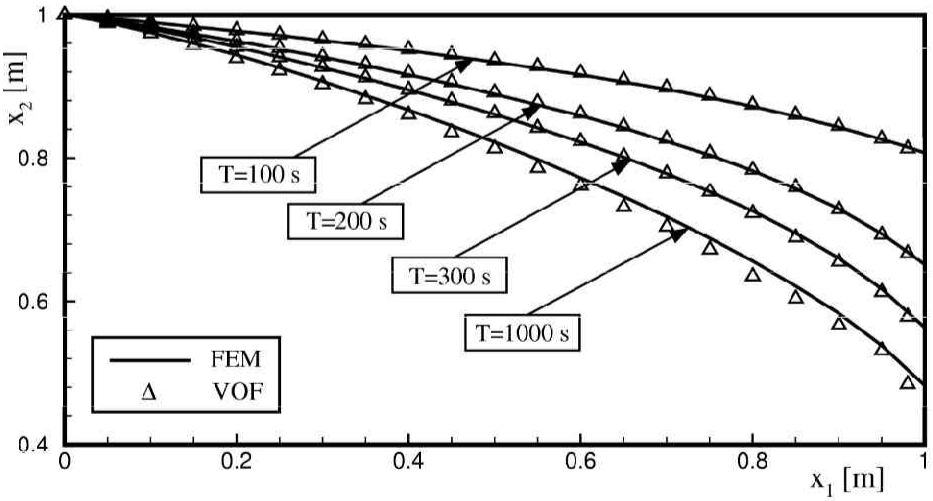

Figure 3.12: Comparison of calculated water levels ($H_0 = 0.6m$)

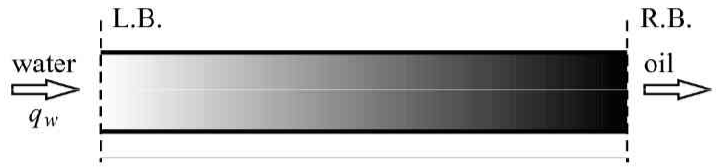

Figure 3.13: The Buckley-Leverett test problem scheme

3.5.2 The Buckley-Leverett problem

The Buckley-Leverett problem [Buckley and Leverett, 1941] describes one-dimensional (horizontal) transient displacement of the oil phase by the water (or gas) in homogeneous porous media with neglected capillary effects. Under such conditions, the problem allows an analytical solution. Initially, it is assumed that domain is saturated by the oil phase, with water at the residual saturation. At the left boundary, a constant water influx is imposed as a boundary condition (Figure 3.13).

After a minor manipulation, the fractional flow function for the water phase can be defined as:

$$g_w = \frac{q_w}{q_{total}} = \frac{\alpha_w V_w}{\alpha_w V_w + \alpha_o V_o} = \frac{\lambda_w}{\lambda_w + \lambda_o}\left(1 + \frac{1}{\lambda_o}\frac{\lambda_w q_w \quad \lambda_o q_o}{q_w + q_o}\right) \tag{3.51}$$

where subscripts w and o denote the water and oil phase, respectively, q is the specific flux of the corespondent phase and λ is given as:

$$\lambda_w = \frac{\mu_w}{k\ k_{rw}} \qquad \lambda_o = \frac{\mu_o}{k\ k_{ro}} \tag{3.52}$$

in which k_{rw} and k_{ro} represent relative permeability function for the water and oil phase, respectively. It is worthwhile to note that from the incompressibility condition q_{total} is constant throughout the domain and equals to the injected flow rate of the water. This injection rate, in general case, can be function of time, however, in this test case it is taken as constant.

Neglecting acceleration and viscous terms, momentum equation for the horizontal (x_1) direction simplifies to:

$$q_w \lambda_w = -\frac{\partial p}{\partial x_1} \tag{3.53}$$

$$q_o \lambda_o = -\frac{\partial p}{\partial x_1} \tag{3.54}$$

where for the resistance term, the Darcy law with hydraulic permeability is utilized (expression (2.41), supplemented with relative permeability concept). Since the capillarity is neglected, there is no "jump" of pressure at the interface between the water and oil phase and therefore, subscripts in the pressure terms are omitted.

Substitution of (3.53) and (3.54) reduces equation (3.51) to:

$$g_w = \frac{\lambda_w}{\lambda_w + \lambda_o} = \frac{1}{1 + \frac{\mu_o k_{rw}}{\mu_w k_{ro}}}, \tag{3.55}$$

i.e. it is only function of the relative permeability functions, which, in turn, are only function of the water content.

Considering the continuity equation (2.49) for the water phase, expressed in terms of fractional flow function:

$$\frac{\partial S_w}{\partial t} + \frac{q_{total}}{\phi}\frac{\partial g_w}{\partial x_1} = 0, \tag{3.56}$$

the fractional flow function, conceptually solves the problem, with non dimensional propagation velocity of specific water saturation given by:

$$v_S = \frac{dg_w}{dS_w} \tag{3.57}$$

where S_w is the water saturation ($S_w = \alpha_w/\phi$). The advance of specific saturation profile can be calculated from:

$$(x_1)_{S_w} = \frac{q_{total}}{\phi}\int_0^t \left(\frac{dg_w}{dS_w}\right)_{S_w} d\tau \tag{3.58}$$

In the case that propagation velocity does not decrease monotonically everywhere from the initial condition (which is the case here), the nonphysical solution occurs with multivalued saturations at specific lengths. Or alternatively, if somewhere in the domain, higher saturations move faster than lower saturations, the saturation jump must exist. Graphically, the saturation jump is defined by the tangent line on the $g_w\,(S_w)$ function starting from the initial saturation. For the test problem considered here, the fractional flow function is shown in Figure 3.13. Physical parameters are taken from the Wendland and Flensberg [2005] and summarized in Table 3.1. Relative permeability functions are adopted from the Brooks and Corey model, defined as:

$$k_{rw} = S_{we}^{(2+3\chi)/\chi} \tag{3.59}$$

$$k_{ow} = (1 - S_{we})^2 \left(1 - S_{we}^{(2+\chi)/\chi}\right) \tag{3.60}$$

Table 3.1: Physical parameters adopted for the test problem.

Parameter	Value
Intrinsic permeability	$1.0 \cdot 10^{-7}$ [m^2]
Porosity	0.2 [-]
Water residual saturation	0.2 [-]
Oil residual saturation	0.2 [-]
Density of water and oil	1000.0 [kg/m^3]
Viscosity of water and oil	0.001 [Pa s]
Parameter χ in eqs. (3.59) and (3.60)	2.0 [-]

Table 3.2: Boundary conditions for numerical simulation.

Left boundary:	Right boundary:	Walls:
$q_w = 1.5 \cdot 10^{-7}$ m/s	$p = 0.0$	$V_w = 0.0$ $W_w = 0.0$
$q_o = 0.0$		$V_o = 0.0$ $W_o = 0.0$
$S_w = 0.8$		

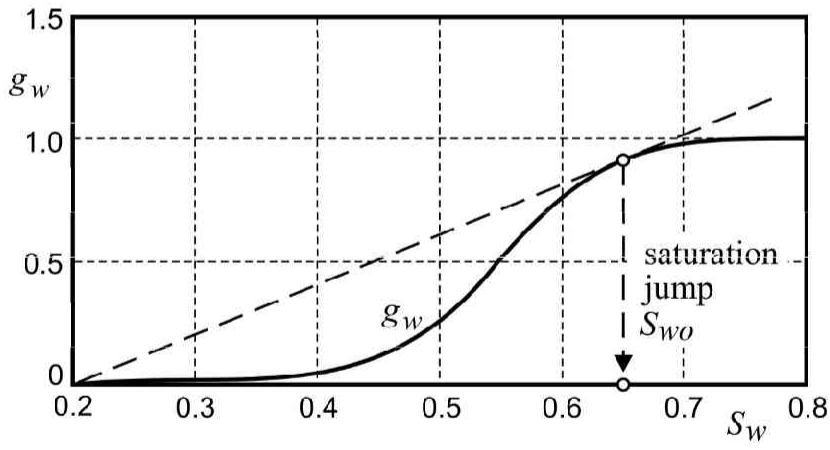

Figure 3.14: Fractional flow curve for the test problem

where S_{we} is the effective water saturation ($S_{we} = S_w - S_{residual}$) and χ is the fitting parameter.

To complete the mathematical description of the test problem, the boundary conditions must be specified. These are summarized in Table 3.2. Calculated saturation jump

for specified initial and boundary conditions is $S_{wo} = 0.65$, with $g_w(S_{wo}) = 0.92$ and $g'_w(S_{wo}) = 2.0455$.

Results and discussion

For the numerical solution, a 300m long domain is discretized by cubes, where the size of cubes is varied: 2mx2mx2m, 4mx4mx4m and 10mx10mx10m. For all tests, the same time step of one day adopted as a appropriate value for the simulation. The test problem is used to investigate effects of different slope limiters on calculated results.

In addition to limiters shown in Figure 3.5, a limiter function proposed by Mulder [Wendland and Flensberg, 2005] is also compared. For the linear distribution of convected property α, the values at the cell boundary are estimated as:

$$\alpha^L_{i+1/2} = \alpha_i + \frac{\Delta x_i}{2} S^L_{x_1} \tag{3.61}$$

$$\alpha^R_{i+1/2} = \alpha_{i+1} - \frac{\Delta x_{i+1}}{2} S^R_{x_1} \tag{3.62}$$

where the slope S_{x_1} for the left (L) side, according to the Mulder limiter function is defined as:

$$S^L_{x_1} = \begin{cases} min\left[2\delta^{LU}, 2\delta^{LD}, \frac{1}{2}(\delta^{LU} + \delta^{LD})\right], & if \quad \delta^{LU} > 0 \quad and \quad \delta^{LD} > 0 \\ max\left[2\delta^{LU}, 2\delta^{LD}, \frac{1}{2}(\delta^{LU} + \delta^{LD})\right], & if \quad \delta^{LU} < 0 \quad and \quad \delta^{LD} < 0 \\ 0, \quad else \end{cases} \tag{3.63}$$

where $\delta^{LU} = (\alpha_i - \alpha_{i-1})/\Delta x_{i-1/2}$ and $\delta^{LD} = (\alpha_{i+1} - \alpha_i)/\Delta x_{i+1/2}$.

Similarly for the right (R) side:

$$S^R_{x_1} = \begin{cases} min\left[2\delta^{RU}, 2\delta^{RD}, \frac{1}{2}(\delta^{RU} + \delta^{RD})\right], & if \quad \delta^{RU} > 0 \quad and \quad \delta^{RD} > 0 \\ max\left[2\delta^{RU}, 2\delta^{RD}, \frac{1}{2}(\delta^{RU} + \delta^{RD})\right], & if \quad \delta^{RU} < 0 \quad and \quad \delta^{RD} < 0 \\ 0, \quad else \end{cases} \tag{3.64}$$

where $\delta^{RU} = (\alpha_{i+1} - \alpha_i)/\Delta x_{i+1/2}$ and $\delta^{RD} = (\alpha_{i+2} - \alpha_{i+1})/\Delta x_{i+3/2}$.

Figures 3.15 - 3.20 show comparison of numerical and analytical solution of water/oil distribution, where several types of limiter functions are applied and for different size of space discretization. It can be observed that all limiter functions produced very similar results. The accuracy is significantly increased with finer space discretization. With 2m discretization,

which is reasonable discretization for the most of two phase flows in subsurface applications, the agreement with analytical solution is almost perfect, with minimal effects of numerical diffusion.

The mass balance can be critical point in numerical schemes for simulation of two-phase flow in porous media [Celia *et al.*, 1990; Celia and Binning, 1992; Forsyth *et al.*, 1995]. In the presented model, the mass balance accuracy directly depends on adopted convergence criteria for divergence. In the presented test problem, after 1500 days of simulation, the mass balance error was in all cases less than 0.002%. This error is calculated as a mass accumulation divided by net influx through the left boundary.

3.6 Summary

The volume averaged governing equations for multiphase flow, obtained in the previous chapter, are discretized by finite volume method with full staggered arrangement of hydraulic variables. Here, the velocity vectors are defined at cell boundaries and scalars are defined at cell centers. For reconstruction of scalars at the cell boundaries, a higher order approach is utilized, with a TVD slope limiters applied in order to avoid numerical diffusive effects, as well as occurrence of oscillations around the sharp fronts, which is characteristic for higher order schemes. In the case of existence of free surface, the VOF method is utilized, which is here slightly adapted for flows in porous media.

Coupled momentum and mass conservation equations are solved by extending the HSMAC method to multiphase flows, where special consideration is devoted to efficiency of iterative procedure.

Developed model is validated by applying to two flow problems. First, to the free surface flow problem through the vertical dam, where the model is compared with finite element solution of Darcy flow equation (Laplace equation). The intention was to check the performance of VOF method in the flow in porous media and also, to examine the role of acceleration terms on free surface shape, in relatively high permeable soils. The model showed very good agreement with the FEM results, except in the case of high gradients, where the difference occurred due to acceleration effect.

In the second test problem, the well known Buckley-Leverett problem of two phase

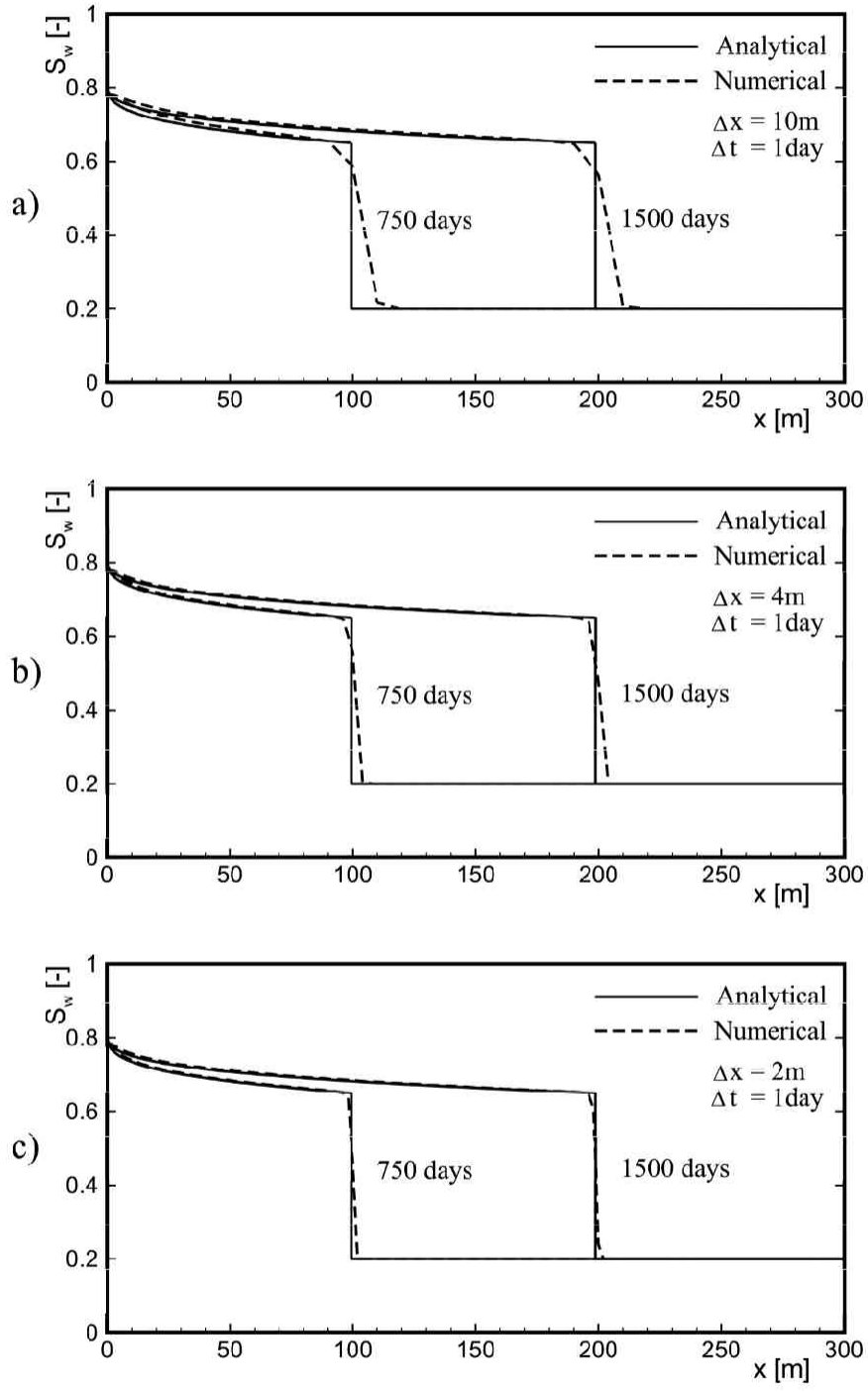

Figure 3.15: Comparison of numerical and analytical solution - Van Leer's limiter: a) 10m space discretization, b) 4m space discretization, c) 2m space discretization.

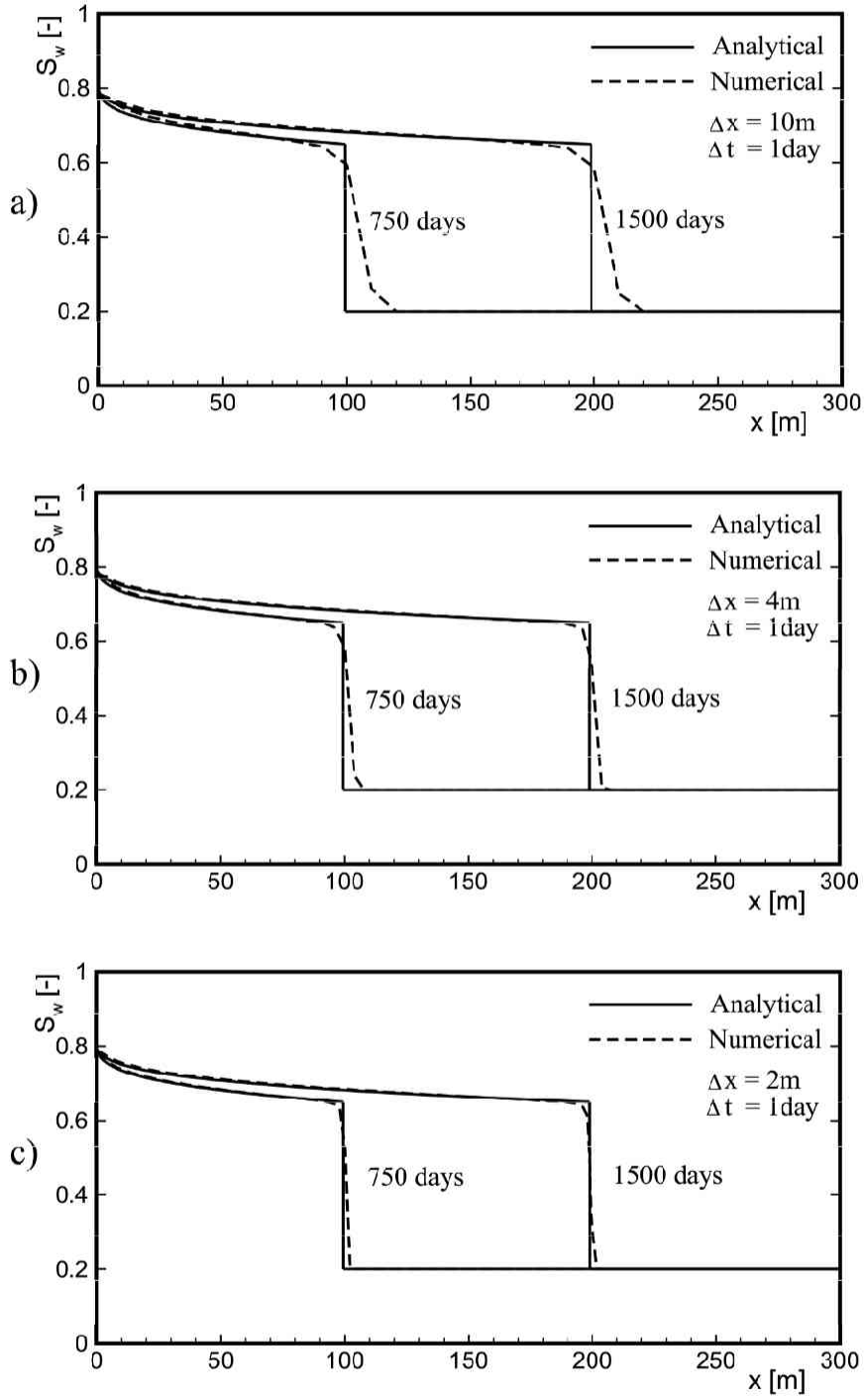

Figure 3.16: Comparison of numerical and analytical solution - Minmod limiter: a) 10m space discretization, b) 4m space discretization, c) 2m space discretization.

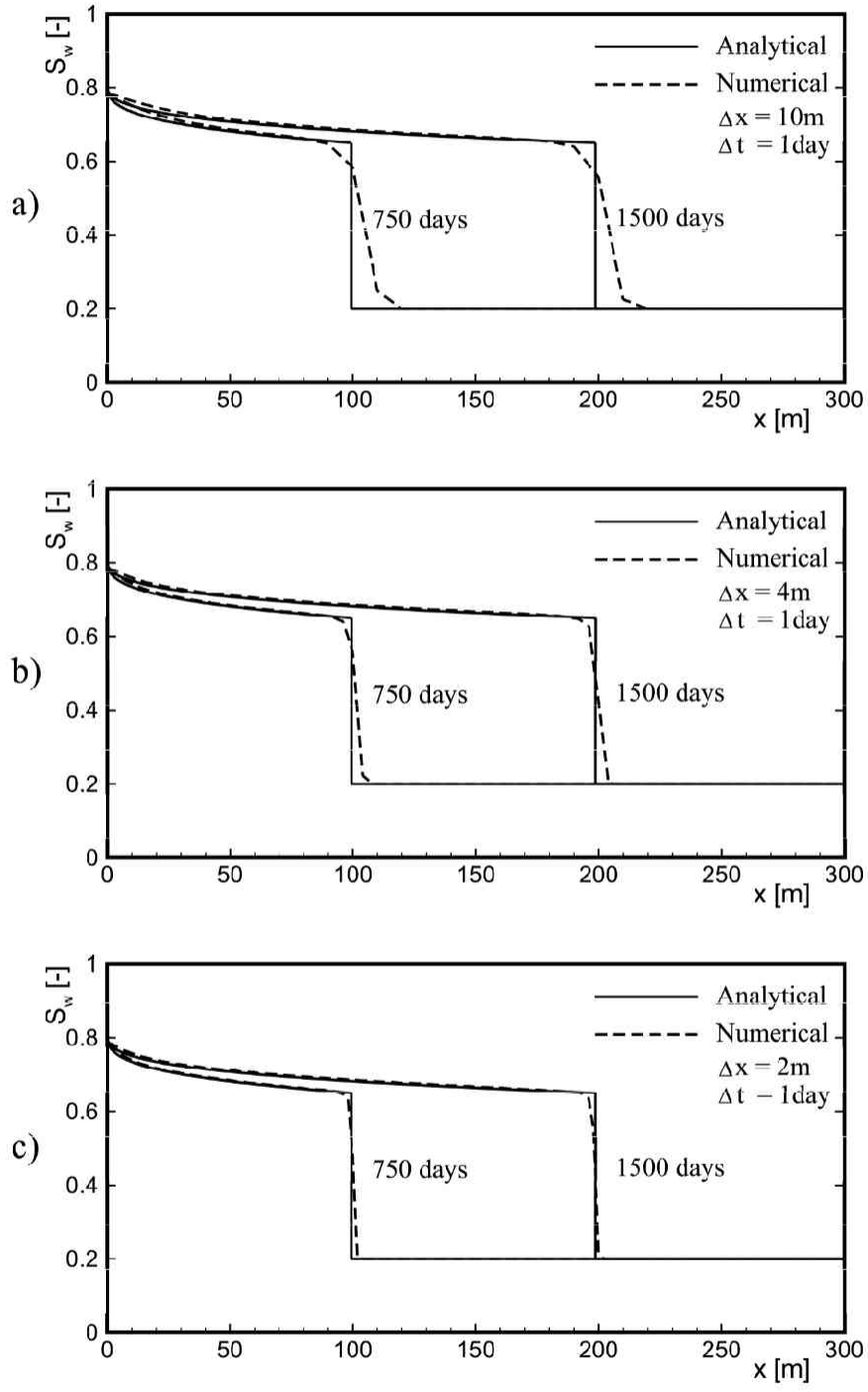

Figure 3.17: Comparison of numerical and analytical solution - SuperBee limiter: a) 10m space discretization, b) 4m space discretization, c) 2m space discretization.

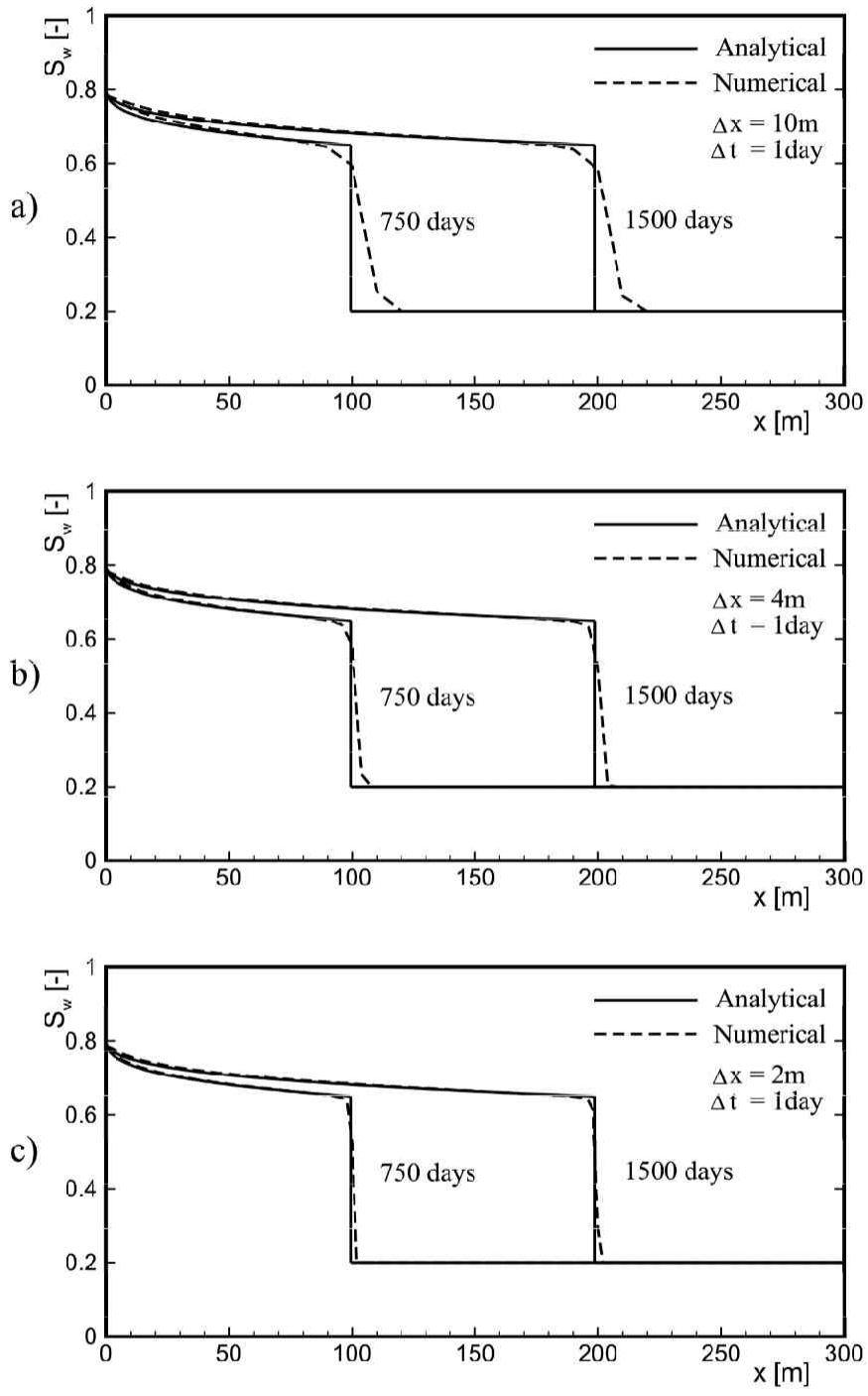

Figure 3.18: Comparison of numerical and analytical solution - Chakravarthy and Osher limiter ($\kappa = 1/3$, $\beta = 1.2$): a) 10m space discretization, b) 4m space discretization, c) 2m space discretization.

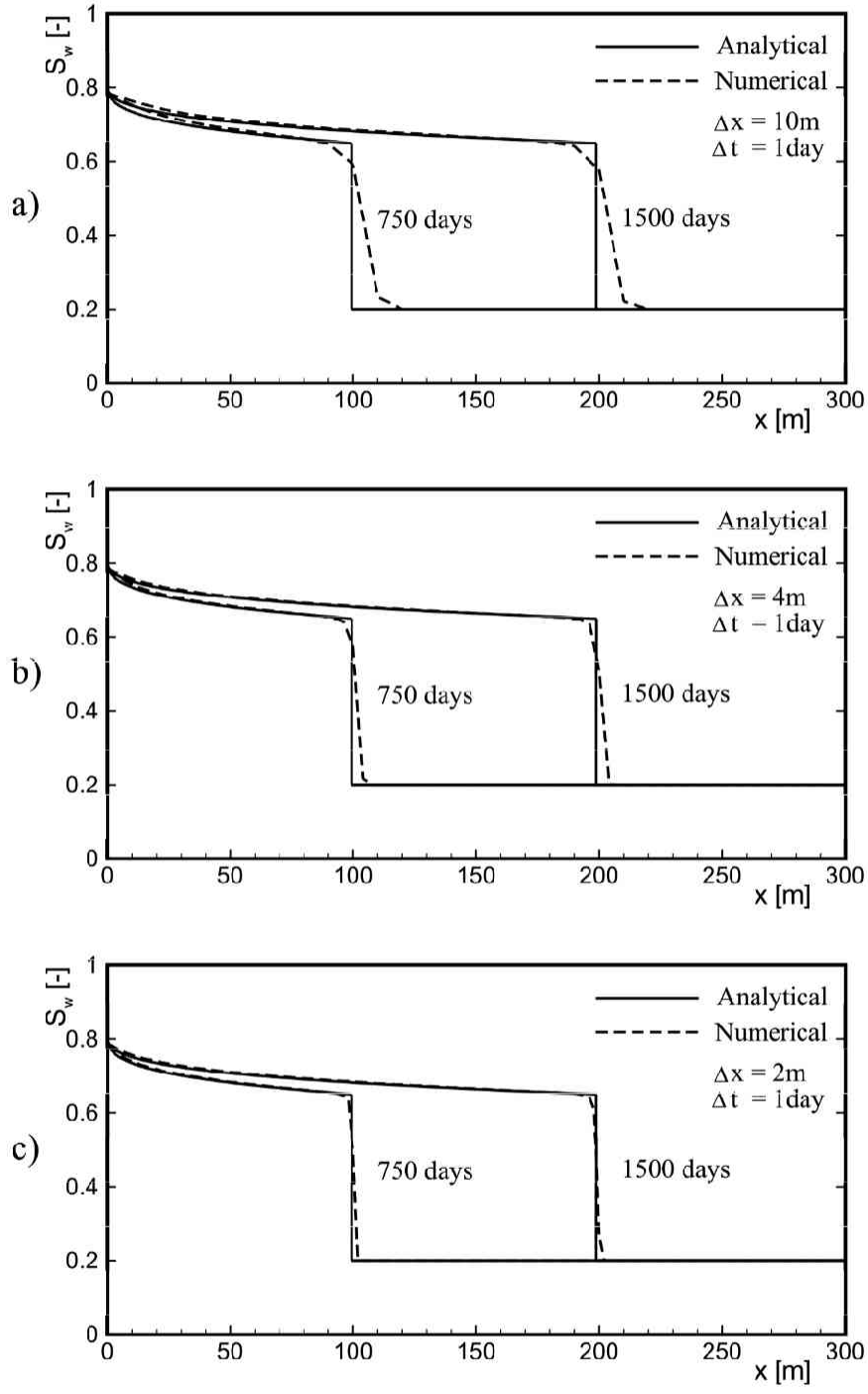

Figure 3.19: Comparison of numerical and analytical solution - Chakravarthy and Osher limiter ($\kappa = 1/3$, $\beta = 2.0$): a) 10m space discretization, b) 4m space discretization, c) 2m space discretization.

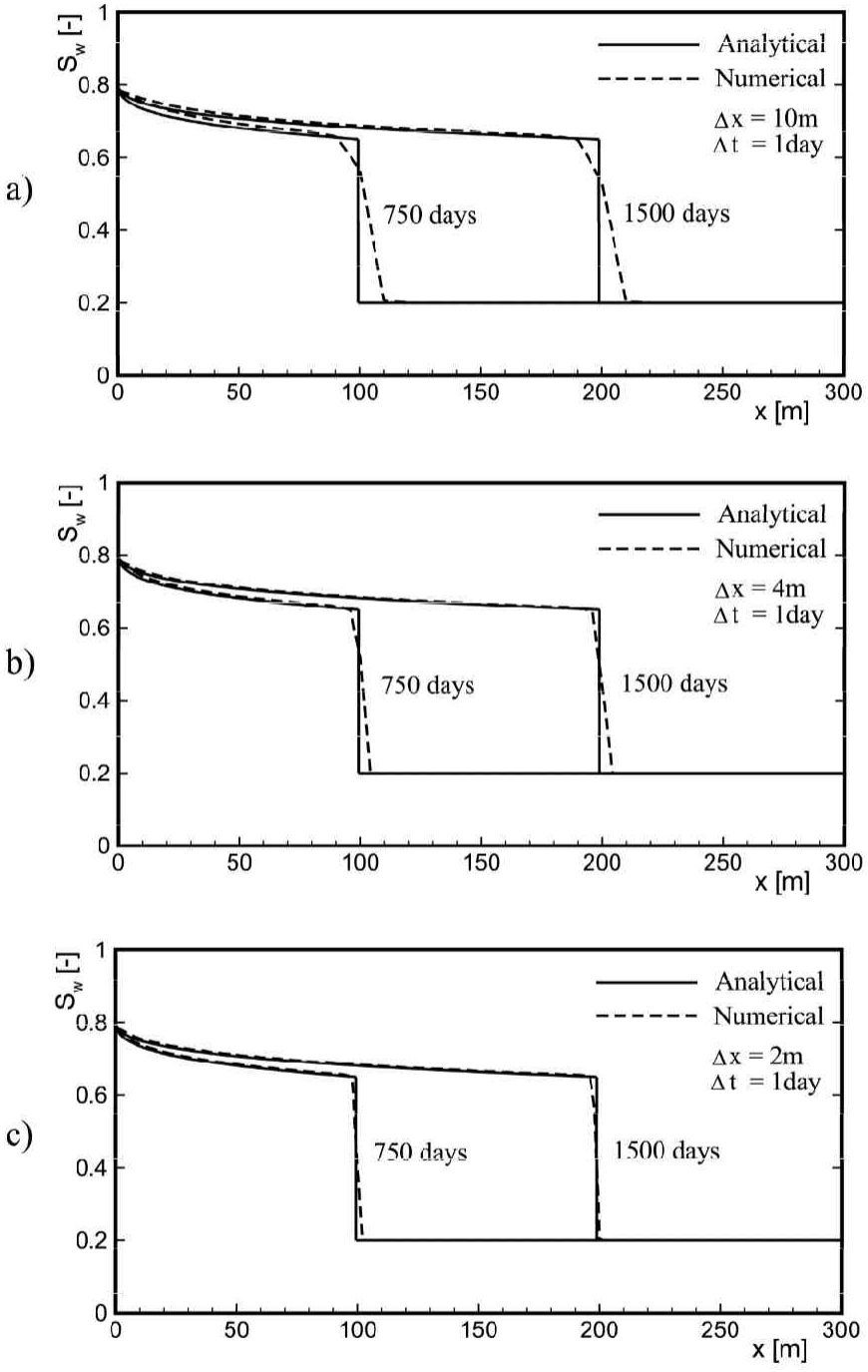

Figure 3.20: Comparison of numerical and analytical solution - Mulder's limiter: a) 10m space discretization, b) 4m space discretization, c) 2m space discretization.

flow through the porous medium is applied. The existence of analytical solution and sharp fronts of phase saturations is used for testing of different types of limiter functions. All limiter functions tested here showed very similar results. Generally, developed model produced excellent behavior in advective dominated problem, with minimal diffusive effects at sharp fronts. Therefore, it is assumed that presented model can be applied for reliable analysis of multiphase flow problems which are described in following chapters.

Chapter 4

Model Application: Analysis of acceleration effects on the flow in a low-permeable soil

4.1 Preliminaries

In this chapter the developed model is utilized to analyze the role of acceleration terms in momentum equations in the process of pressure redistribution during the deep tunnel excavation. The role of local acceleration term in flow in porous media is investigated by several authors [Bear, 1972], and general conclusion can be summarized that this term is important only at the onset of fluid motion, and very fast it becomes negligible. However, the exact comparisons, where its effects could be clearly seen are lacking.

According to Whitaker [1969, p.25], conceptualizing a saturated flow in porous media as a creep flow in a tube :

> If a tube filled with fluid is subjected to a sudden change in the pressure drop, essentially steady flow occurs for time greater than t_0 where $t_0 = d^2/4\nu$. Here d is the tube diameter and ν is the kinematic viscosity. For the purpose of estimating microscopic transient times in porous media, a practical lower bound on ν is $10^{-2} cm^2/s$, and an upper bound on d might be on the order of $10^{-1} cm$. This gives a microscopic transient time time on the order of 1 second, and if the

> transient time for the macroscopic process is much larger (say on the order of minutes), we should be able to treat the flow as quasi steady...

Similarly concluded Philip [1957] by analytical analysis of 1D diffusion equation. He found that the transient time in a saturated porous medium is proportional to the permeability and inversely proportional to the kinematic viscosity. However, he also found that in the case of periodic change of boundary conditions, the effects of inertia term can be significant, even if the frequency is quite low, e.g. order of one cycle per minute.

Since the study case will be applied for the soil with relatively low hydraulic permeability, it is expected that convective inertia term will not play an important role. Choudhary *et al.* [1976] have numerically analyzed the role of convective inertia for the steady gas flow through the packed beds by comparing the streamline patterns and the velocity profiles of two models: with and without the inertia terms. They used Ergun formula [Ergun, 1952] for the drag term in momentum equations. In the case of uniform packing, they observed practically negligible difference. However, in the case of nonuniform packing, they have observed the effects on the streamlines in the near zone of abrupt change of the packed material, i.e. in the zone of change of hydraulic permeability. Nevertheless, they concluded that even in highly permeable packed beds, the convective inertia terms are small enough to be experimentally detected.

In addition, the intention of this study case was to test the performance of the model in highly unsteady conditions by comparison with developed analytical solution of transient pressure distribution along the symmetry line above the excavation and also by comparison with FEM solution of Darcy-law (Laplace equation). Here, the same finite element model is used as described in the previous chapter.

4.2 Analytical solution of transient pressure distribution

Figure 4.1 schematically shows the flow domain considered in this study. Boundary conditions are constant hydraulic heads on the vertical domain boundaries, and zero pressure on the walls of excavation. Initially, hydrostatic pressure distribution is assumed everywhere.

The analytical solution of transient pressure distribution along the symmetry line is based on the assumption that vertical velocity distribution, above the tunnel excavation,

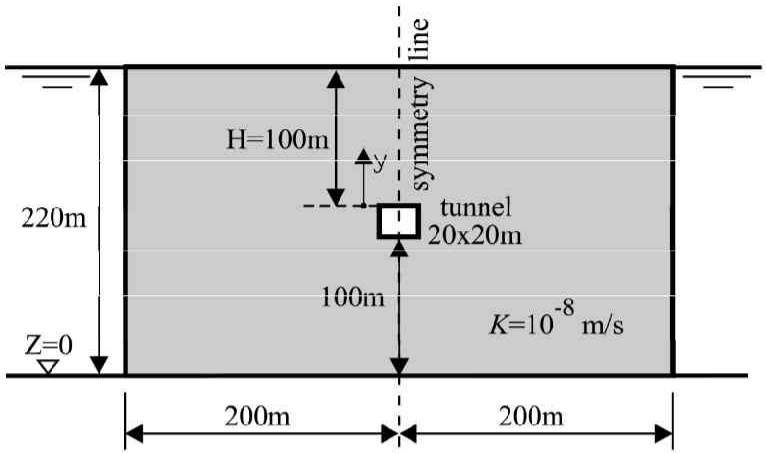

Figure 4.1: Study case of deep tunnel excavation ($K = 1x10^{-8}$ m/s, $\phi = 0.5$)

is linear:

$$v(t, y) = v_0(t)\left(1 - \frac{y}{H}\right) \tag{4.1}$$

Here, $v(t, y)$ is the vertical velocity, $v_0(t)$ is the vertical velocity at the tunnel boundary ($y = 0$), y is the vertical coordinate (positive upward), H is the water height above the tunnel excavation and t is the time.

Neglecting the viscous term in momentum equation, and assuming the homogeneous and rigid porous media, the momentum equation 2.50 in the y direction can be written as:

$$\frac{\partial v}{\partial t} + v\frac{\partial v}{\partial y} = -g - \frac{1}{\rho}\frac{\partial p}{\partial y} - R_y v \tag{4.2}$$

with, the drag term coefficient expressed according to the Darcy law:

$$R_y = \phi\frac{g}{K} \tag{4.3}$$

Substituting (4.1) into (4.2) yields:

$$\left(\frac{dv_0}{dt} - \frac{v_0^2}{H} + R_y v_0\right)\left(1 - \frac{y}{H}\right) = -g - \frac{1}{\rho}\frac{\partial p}{\partial y} \tag{4.4}$$

which can be integrated from $y = 0(p = 0)$ to $y = H(p = 0)$ in order to obtain following ordinary differential equation (ODE) for velocity at the top of excavation:

$$H\frac{dv_0}{dt} = v_0^2 - HR_y v_0 - 2gH \tag{4.5}$$

Equation (4.5) cen be rewritten in a more appropriate way to obtain a solution:

$$\frac{dv_0}{(v_0-a)(v_0-b)} = \frac{dt}{H} \tag{4.6}$$

where a and b are defined as:

$$a = \frac{HR_y}{2} - \sqrt{\left(\frac{HR_y}{2}\right)^2 + 2gH} \tag{4.7}$$

$$b = \frac{HR_y}{2} + \sqrt{\left(\frac{HR_y}{2}\right)^2 + 2gH} \tag{4.8}$$

During the calculation of a and b by computer, it is essential to note that $2gH \ll (HR_y/2)^2$, and that computer roundoff error in this case can produce significant errors. In such cases, the solution of quadratic equation $ax^2 + bx + c$ should be obtained from:

$$x_1 = \frac{c}{q} \quad x_2 = \frac{q}{a} \tag{4.9}$$

where q is given as:

$$q = -\frac{1}{2}\left[b + sgn(b)\sqrt{b^2 - 4ac}\right] \tag{4.10}$$

Now, considering that $v_0(0) = 0$, the solution of equation (4.5) can be easily found as:

$$v_0(t) = ab\frac{1 - e^{-\frac{t}{cH}}}{b - ae^{-\frac{t}{cH}}} \tag{4.11}$$

in which the coefficient c is defined as:

$$c = \frac{1}{b-a} = \left(2\sqrt{\left(\frac{HR_y}{2}\right)^2 + 2gH}\right)^{-1} \tag{4.12}$$

It can be noted that from equation (4.11) follows that $v_0 \to a$ when $t \to \infty$, i.e. that steady-state velocity at the top of excavation is given by:

$$v_0(\infty) = \frac{HR_y}{2} - \sqrt{\left(\frac{HR_y}{2}\right)^2 + 2gH} \tag{4.13}$$

which is always negative, as it should be.

Now, one can obtain solution for the pressure. From equation (4.5) it follows that:

$$\frac{dv_0}{dt} - \frac{v_0^2}{H} + R_y v_0 = -2g \tag{4.14}$$

Integrating (4.4) from $y = 0(p = 0)$ to $y = y(p = p)$, the pressure height can be expressed as:

$$\frac{p(t,y)}{\rho g} = \frac{p(y)}{\rho g} = y - \frac{y^2}{H} \tag{4.15}$$

Equation (4.15) shows that, for the incompressible fluid and rigid porous media, the pressure is adjusted to the boundary conditions instantaneously, while the velocity needs "some time" to obtain the steady condition. It should be also noted that, strictly speaking, infinity velocity from equation (4.13) will never be reached, due to change of surface level with the time. Since this change is very slow process for the most practical cases, this velocity can be considered as quasi-steady velocity.

Obtained pressure distribution for assumed linear velocity distribution has parabolic shape with maximum value at the height $H/2$, where the pressure value is $\rho g H/4$, independently of soil permeability and porosity. Soil parameters influence, however, the velocity and time to obtain the quasi-steady conditions.

4.3 Case with the less permeable lining

Similar analysis will be conducted for the case of tunnel excavation lined by less permeable material (as shown in Figure 4.2). In this case, one more condition is required in order to obtain the solution. Since the width of the lining is small comparing to tunnel depth (H), velocity through the lining can be assumed as constant and equal to the velocity v_0 at the top of the excavation.

Hence, the velocity distribution can be expressed as:

$$v(t,y) = v_0(t)\,, \quad 0 \le y \le H_1 \tag{4.16}$$

$$v(t,y) = v_0(t)\frac{H}{H - H_1}\left(1 - \frac{y}{H}\right)\,, \quad H_1 \le y \le H \tag{4.17}$$

Substituting (4.16) and (4.17) into equation (4.2) gives:

$$\frac{dv_0}{dt} + R_{y1}v_0 = -g - \frac{1}{\rho}\frac{\partial p}{\partial y}, \qquad 0 \le y \le H_1 \tag{4.18}$$

$$\left(\frac{dv_0}{dt} - \frac{v_0^2}{H - H_1} + R_{y2}v_0\right)\frac{H}{H - H_1}\left(1 - \frac{y}{H}\right) = -g - \frac{1}{\rho}\frac{\partial p}{\partial y}, \quad H_1 \le y \le H \tag{4.19}$$

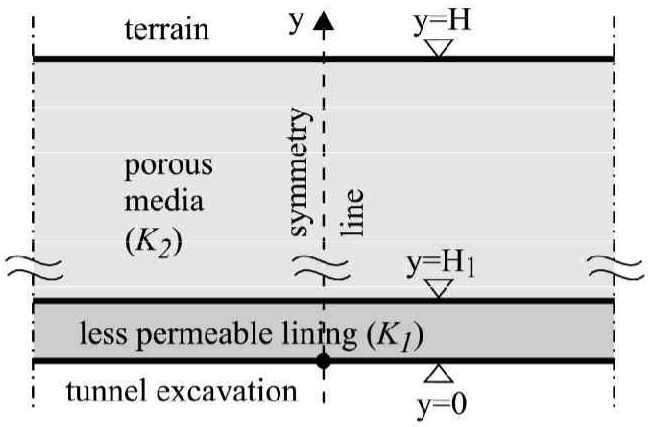

Figure 4.2: Schematic cross-section of tunnel excavation lined by less permeable material

where R_{y1} and R_{y2} are defined as:

$$R_{y1} = \phi_1 \frac{g}{K_1}, \quad R_{y2} = \phi_2 \frac{g}{K_2} \tag{4.20}$$

Integrating again along the symmetry line, one obtains:

$$(H + H_1) \frac{dv_0}{dt} = v_0^2 - v_0 \left[2R_{y1}H_1 + R_{y2}(H - H_1)\right] - 2gH \tag{4.21}$$

for which the solution can be found as:

$$v_0(t) = a_1 b_1 \frac{1 - e^{\frac{t}{c_1(H+H_1)}}}{b_1 - a_1 e^{\frac{t}{c_1(H+H_1)}}} \tag{4.22}$$

where parameters a_1, b_1 and c_1 are defined as:

$$a_1 = \frac{\left[2R_{y1}H_1 + R_{y2}(H - H_1)\right]}{2} - \sqrt{\left[\frac{2R_{y1}H_1 + R_{y2}(H - H_1)}{2}\right]^2 + 2gH} \tag{4.23}$$

$$b_1 = \frac{\left[2R_{y1}H_1 + R_{y2}(H - H_1)\right]}{2} + \sqrt{\left[\frac{2R_{y1}H_1 + R_{y2}(H - H_1)}{2}\right]^2 + 2gH} \tag{4.24}$$

$$c_1 = \frac{1}{b_1 - a_1} \tag{4.25}$$

Similarly as in the case without the lining, the quasi-steady velocity is given by $v_0(t = \infty) = a_1$.

Substituting the obtained velocity solution (4.22) and its time derivative into equation (4.21), and then integration along the symmetry line, gives solution for the transient pressure:

$$g\left(y + \frac{p}{\rho g}\right) = -\left[R_{y1}v_0 + \frac{a_1}{c_1(H + H_1)} \frac{w}{-b_1 + a_1 w}(v_0 - b_1)\right] y, \quad 0 \le y \le H_1 \tag{4.26}$$

$$g\left(y+\frac{p}{\rho g}\right)=\left[gH+\left(\frac{dv_0}{dt}+R_{y1}v_0\right)H_1\right]\left[1+\frac{2H}{(H-H_1)^2}\left(y-\frac{y^2}{2H}\right)\right.$$
$$\left.-\frac{H^2}{(H-H_1)^2}\right]+\left(\frac{dv_0}{dt}+R_{y1}v_0\right)H_1\,,\quad H_1\leq y\leq H \tag{4.27}$$

where the term dv_0/dt can be expressed as:

$$\frac{dv_0}{dt}=\frac{a_1(v_0-b_1)}{c_1(H+H_1)}\frac{e^{\frac{-t}{c_1(H+H_1)}}}{-b_1+a_1e^{\frac{-t}{c_1(H+H_1)}}} \tag{4.28}$$

From equations (4.26)and (4.27), it can be concluded that in this, heterogeneous case, the pressure is the function of time, i.e. it is not reached instantaneously as was shown in the the homogeneous case.

4.4 Numerical results and discussion

For the numerical solution, due to the problem symmetry, only a half of the domain shown in Figure 4.1 is modeled. Along the symmetry line the slip velocity condition is imposed. Discretization of the flow domain is shown in Figure 4.3, with the smallest grid size near the tunnel (10cmx10cm) and gradually increasing size far from the tunnel. In the case of lined tunnel with lower permeability material, the lining width is 30cm. Similar discretization is also used for the FEM model.

Figure 4.4 shows calculated pressure distribution for the homogeneous case, where the quasi-steady pressure distribution is obtained instantaneously. It can be seen that FV and FEM models produce identical results. It can be also noticed that analytical solution slightly differs from the numerical ones. The deviation can be attributed to the assumed linear velocity distribution along the symmetry line. Nevertheless, the pressure distribution near the excavation (about 20m) is in a very good agreement. The maximum pressure is overestimated by the analytical solution, and according to the numerical results its position is approximately at one third of the water depth above the excavation. It can be concluded that local inertia term does not influence the pressure distribution in a homogeneous porous media.

Figure 4.5 shows results comparison of the analytical and the FV model for the homogeneous case, after obtaining the quasi-steady condition. The deviation from the linear

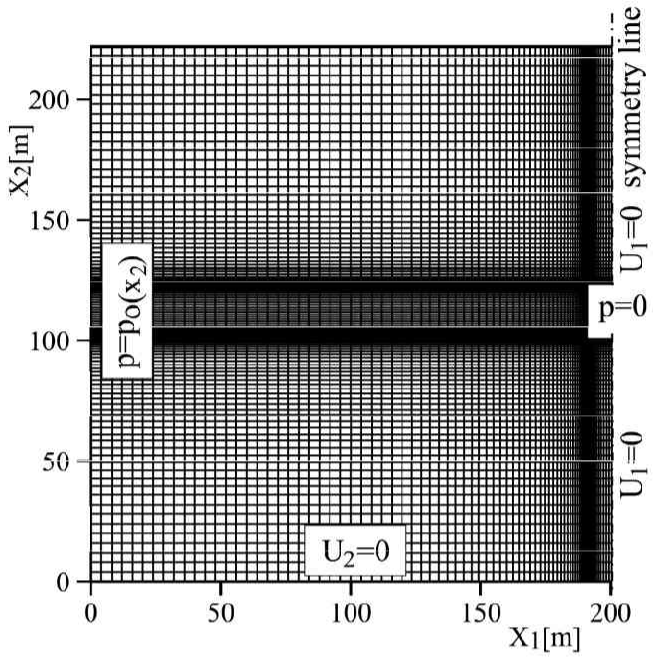

Figure 4.3: Flow around the tunnel excavation: discretization and boundary conditions

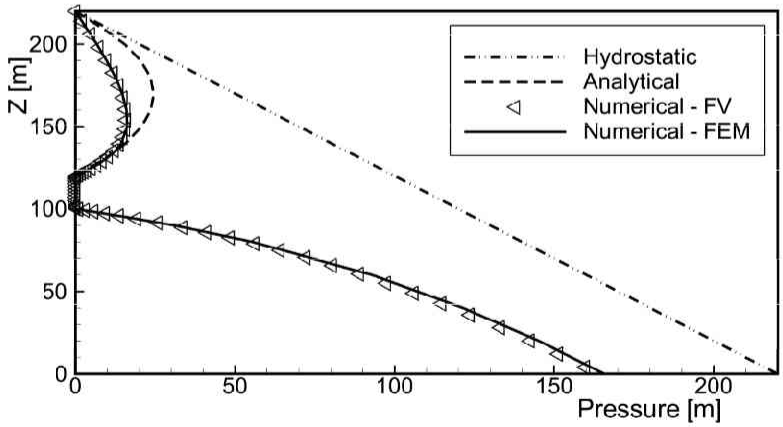

Figure 4.4: Results of the pressure distribution along the symmetry line: FV - finite volume model, FEM - finite element model

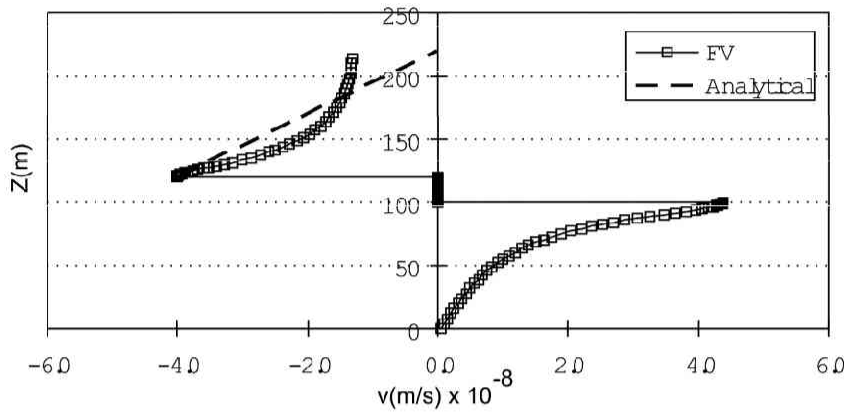

Figure 4.5: Calculated quasi-steady velocity distribution along the symmetry line

velocity distribution, assumed in the analytical solution can be clearly observed. However, there is an excellent match of the quasi-steady velocity on the top of the excavation.

Significantly more interesting is a diagram of transient velocity change at the top of the excavation. Time wise development of the velocity v_0, for the case of hydraulic permeability $K = 1 \cdot 10^{-5}$, is shown in the Figure 4.6, where numerical and analytical results are compared. Very good agreement is observed. It can be seen that quasi-steady condition is achieved very fast. The FEM model, naturally, can not predict this transient behavior of velocity due to omission of the local inertia. The FEM quasi-steady solution match completely with the FV profile shown in Figure 4.5.

Figure 4.7 shows different times required to obtain the quasi-steady velocity at the top of the excavation for different values of hydraulic permeabilities. It can be concluded that required time is is increasing with the increase of hydraulic permeability with order of value of hydraulic permeability, which is in agreement with results of Philip [1957].

For the inhomogeneous case (the case with the low permeable lining), according to equations (4.26) and (4.27), the pressure distribution is not readily reached. This is showed in Figure 4.8, where it can be seen that, instantaneously, the pressure distribution as in the homogeneous case is developed, and afterward, with the increase of the velocity, the pressure distribution is reaching the quasi-steady condition.

For the higher hydraulic permeabilities, but with the same ratio of two permeabil-

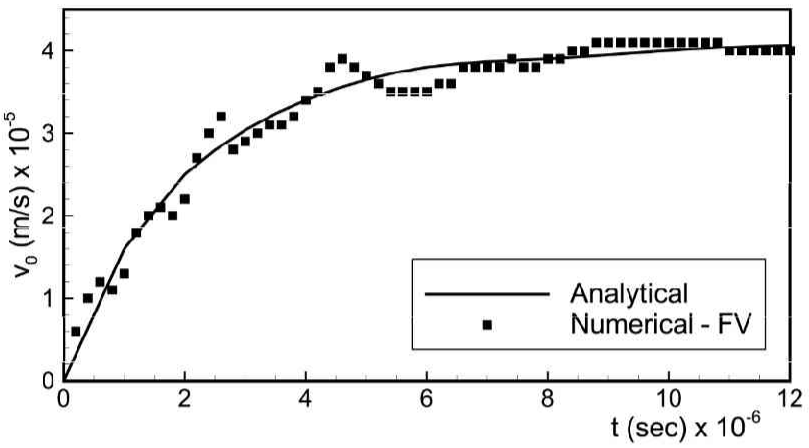

Figure 4.6: Calculated velocity change at the top of excavation

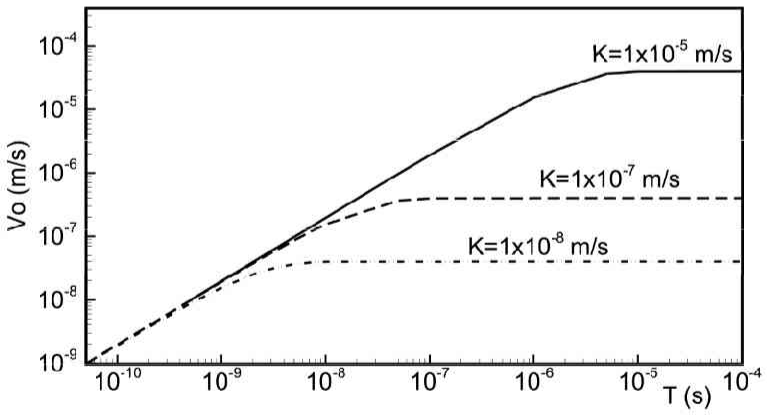

Figure 4.7: Required time to obtain the quasi-steady velocity in the function of soil permeability

ities, the time for reaching the quasi-steady condition is increased for the exact order as for which the permeability is increased. This can be seen in Figure 4.9, which shows the analytical results for 100 times increased hydraulic permeabilities of the lining and the soil in comparison with figure 4.8. The exactly same diagram is obtained, but two orders shifted in the time. If the ratio of the permeabilities is changed, the final pressure distribution is significantly changed, as shown in Figure 4.10.

The proof that the pressure distribution depends only on the ratio of permeabilities and not on their absolute values, can be easily derived by neglecting the acceleration terms in equation (4.2) and considering the equations (4.16) and (4.17). For the pressure at the point A ($y_A = H_1$) the obtained pressure expression in this case is:

$$\frac{p_A}{\rho g} = \frac{H}{1 + \frac{\phi_2 K_1}{\phi_1 K_2} \frac{H - H_1}{2H_1}} - H_1 \tag{4.29}$$

Figure 4.11 shows comparison of analytical and numerical transient solution. The deviation can be again prescribed to the assumption of linear velocity distribution in the soil, but also to some extent, to the additional assumption of constant velocity in the tunnel lining. Nevertheless, relatively good agreement is obtained in the zone near the excavation. Similarly as in the homogeneous case, the FEM model gives only a quasi-steady solution, which is in excellent agreement with the FV model due to negligible effect of convective acceleration term (Figure 4.12).

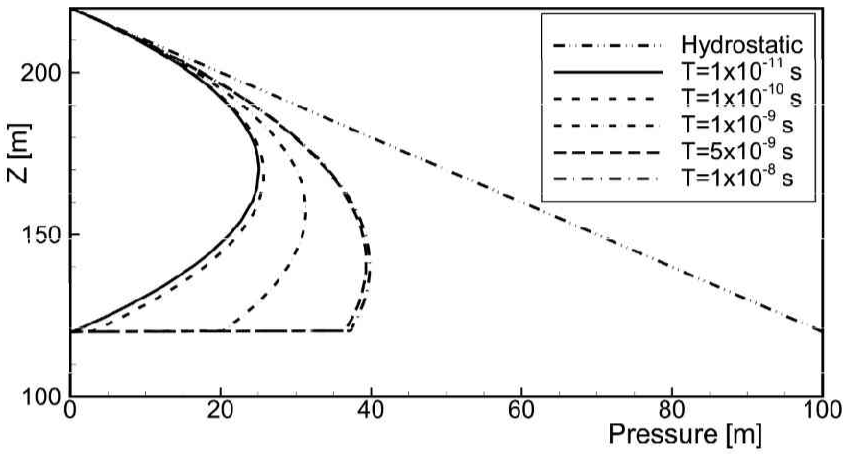

Figure 4.8: Analytical solution for the pressure distribution ($K_1 = 1 \cdot 10^{-10}$, $K_2 = 1 \cdot 10^{-8}$, $H_1 = 0.3m$)

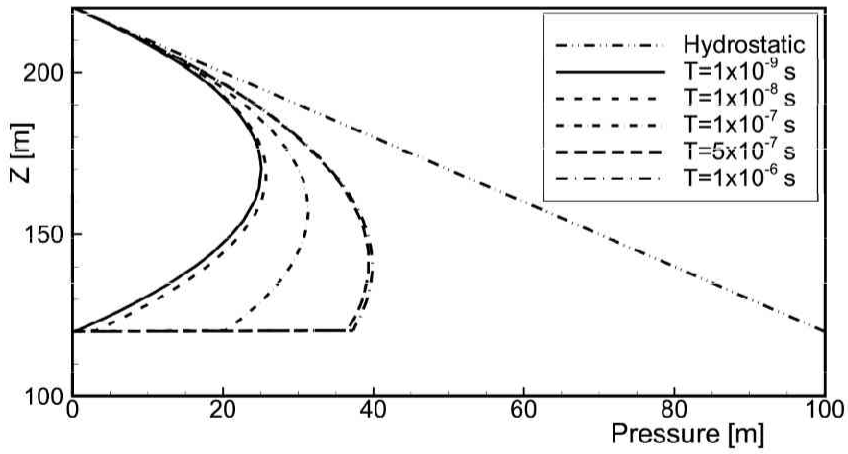

Figure 4.9: Analytical solution for the pressure distribution ($K_1 = 1 \cdot 10^{-8}$, $K_2 = 1 \cdot 10^{-6}$, $H_1 - 0.3m$)

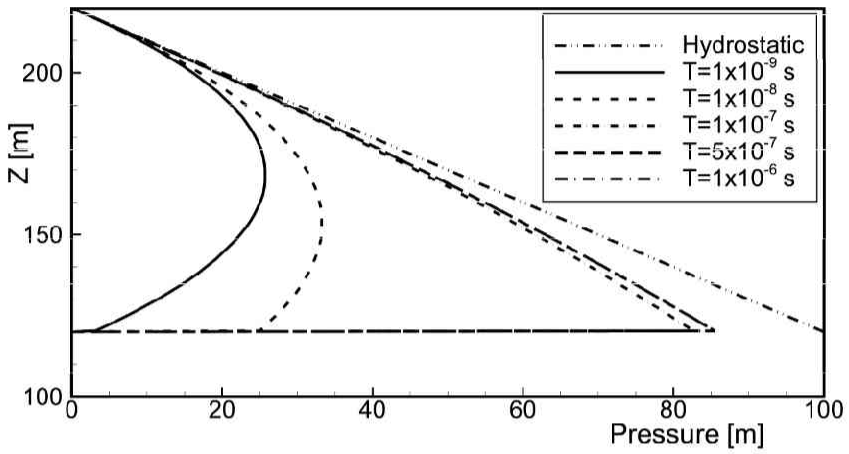

Figure 4.10: Analytical solution for the pressure distribution ($K_1 = 1 \cdot 10^{-9}$, $K_2 = 1 \cdot 10^{-6}$, $H_1 = 0.3m$)

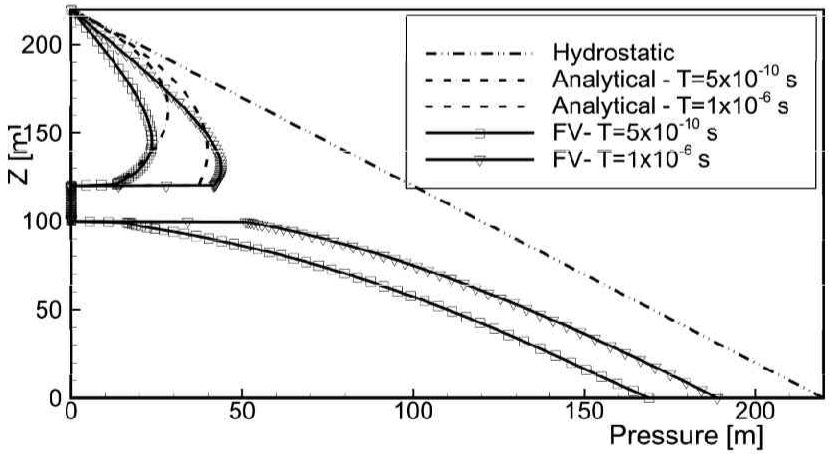

Figure 4.11: Comparison of analytical and FV solution for the transient pressure distribution ($K_1 = 1 \cdot 10^{-10}$, $K_2 = 1 \cdot 10^{-8}$, $H_1 = 0.3m$)

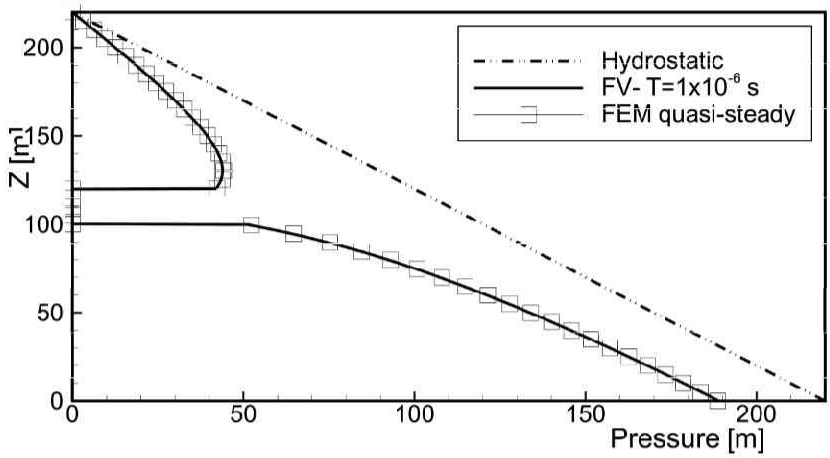

Figure 4.12: Comparison of the FEM and FV solution for the pressure distribution along the symmetry line ($K_1 = 1 \cdot 10^{-10}$, $K_2 = 1 \cdot 10^{-8}$, $H_1 = 0.3m$)

4.5 Summary

In this Chapter, the influence of the local inertia term on the process of pressure redistribution in a deep soil is analyzed numerically and analytically. Two cases are considered: (1) the case of homogeneous medium and (2) the case with less permeable lining around the tunnel excavation. For both cases analytical solution for the symmetry line above the excavation has been derived, under assumption that vertical velocity distribution along this line is linear and that water and soil are incompressible.

In the homogeneous case it is found that pressure adapts to the new boundary conditions instantaneously, while the velocity profile develops from zero to quasi-steady condition very fast. Only during this period, the acceleration term plays a role. It can be concluded that required time to quasi-steady condition is proportional to hydraulic permeability value. As expected, the pressure distribution is not influenced by soil permeability. Obtained analytical pressure distribution is in good agreement with numerical results, especially near the excavation, while the calculated velocities are in excellent agreement.

In the heterogeneous case with the less permeable lining, there is a transient period for the pressure, as well as for the velocity distribution. Pressure changes from the homogeneous solution toward the quasi-steady distribution in a short time proportional to

the hydraulic permeability of the soil. It is found that quasi-steady pressure distribution depends on the permeability ratio between the lining and the medium, not on their absolute values. Again, a good agreement between the numerical and analytical results is observed.

Chapter 5

Model application: Simulation of air sparging

5.1 Introduction

Introduced in the early's 1990's, the air sparging (AS) is probably the most practiced engineered remediation option when targeting the treatment of hydrocarbon-contaminated aquifers [Johnson *et al.*, 2001]. Its widespread use comes from its simplicity, cost effectiveness and reported affirmative results. Its principle is quite simple; the air is injected under the contaminated zone (Figure 5.1), and during its buoyancy induced flow toward the surface, there are two mechanisms which promote the remediation: volatilization of contaminants into the air plume and enhancement of biodegradation processes by increasing the dissolved oxygen in ground water. As showed in Figure 5.1, the (AS) system can be combined with the soil vapor extraction (SVE) system, in order to remove the contaminated air from the vadose zone.

Biosparging is practically the name for the same technology, however, it usually implies low air injection rates, emphasizing the aerobic biodegradation mechanism. The relative contribution between the volatilization and microbial degradation is influenced by many factors, such as air velocity, contaminant volatility, microbial preference factors, contaminant composition and distribution, etc.

In this chapter, the developed model will be applied for numerical simulation of air

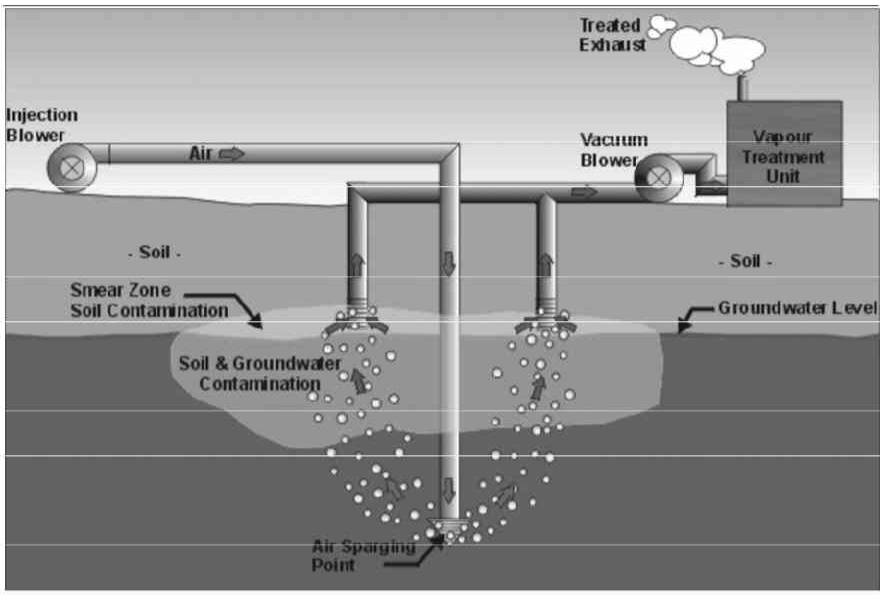

Figure 5.1: Conceptual scheme of AS technology with SVE system for remediation of saturated/unsaturated soils, contaminated by volatile organic compounds, after unknown author

sparging. As will be shown in the literature review of air sparging modeling, the acceleration effects in all, by now reported, models have always been neglected. Due to existence of strong buoyancy force, here it is assumed that acceleration can influence the model results and its modeling can provide more reliable simulations. In addition, the air sparging has been shown to be applicable only in relatively permeable soils [e.g. Johnson *et al.*, 2001], where it can be expected higher magnitudes of air/water velocities. This, in turn, increases acceleration effects. Therefore, the first motivation of this study was to numerically investigate the acceleration effects during the air sparging.

Generally, modeling of air sparging includes two issues: modeling of transient air-water distribution and modeling of contaminant removal. The letter issue is also here considered by model extension and its verification by comparison with several reported experiments. This chapter is therefore divided into two parts: In the next section the problem of air-water distribution modeling will be treated where the main goal was to investigate the acceleration effects, and after that, in the following section, the model extension for the simulation of contaminant removal will be described and verified.

5.2 Modeling of air-water distribution during the air sparging

5.2.1 Literature review of applied multiphase models

Probably the first attempt to numerically model the air sparging was by Unger *et al.* [1995]. They assumed horizontal sparging wells and analyzed mechanisms which influence the dense non-aqueous phase liquids (DNAPLs) removal from heterogeneous porous medium, representative of the Borden aquifer. They used a CompFlow, three-dimensional, three-phase compositional model for a hypothetical sparging scenario. In their analysis, a heterogeneous permeability field (10mx10mx5m) with appropriate mean, variance and spatial correlation was first generated, then, the surface spill of $0.8m^3$ of trichloroethylene (TCE) is simulated, after which the AS is applied, accompanied with SVE. The simulation results revealed that the primary mechanism of contaminant removal in the early stage of air sparging is direct volatilization of non-aqueous phase to the air phase. Later, the contaminant removal is restricted by the dissolution process into the water phase. They also found that degree of heterogeneity impacted the AS performance less in comparison with effects of operating conditions. It should be noted, however, that they assumed an equilibrium of the contaminant partitioning between the phases, which has been shown in the later researches as inapplicable for air sparging simulation.

Lundegard and Andersen [1996] used modified version of the TETRAD finite difference model to investigate the performance of air sparging systems, measured by the predicted region of air flow (zone of influence). All reported simulations were applied on axisymmetric domain with a radius nearly 120m and a depth of about 30m and with neglected capillary effects. They were able to reconstruct the evolution of air distribution after start of air injection and before the attainment of steady conditions. They defined two distinct stages in this process: expansion stage and collapse stage. During the expansion stage the region of air flow increases in volume and reaches the vadose zone. After that, the zone of higher air saturations is forming around the sparging well, leading to second stage in which the zone of airflow begins to collapse until reaching the steady condition. Their sensitivity analysis showed that zone of influence of sparging well will not change with the injection depth, will increase with an increase of air injection rate and will increase with increase of the anisotropy ratio.

McCray and Falta [1997] used a multiphase model T2VOC to simulate the two-dimensional laboratory experiments reported by Ji *et al.* [1993]. In a 2D, rectangular domain with approximately size of 0.7 x 0.9 m, several materials, with different sizes of glass beads were simulated for homogeneous and inhomogeneous cases. Since not all parameters required for numerical simulation were reported by Ji *et al.*, authors used semi-empirical methods to estimate values of intrinsic permeability for each specific size of glass beads. They also used power function of the respective phase saturation to estimate relative permeabilities and Van Genuchten's two-phase formulation for the capillary pressure function. Parameters for these functions were estimated based on the reported air-entry pressures. Qualitative comparison of calculated air distributions with the observed ones showed a good agreement. Due to lack of reported data, no quantitative comparison were possible. They concluded that multiphase models can be used for simulation of air sparging with appropriately characterized heterogeneity of the porous media.

Chen *et al.* [1996] used 1D numerical model for interpretation of their experimental results. Details of used numerical model are referenced in other papers. They used tomography imaging to measure air distribution during the air sparging in saturated sand packs. They observed two classes of behavior: (1) In highly permeable sand packs (106 Darcy) they observed relatively few discrete air pathways with steady conditions rapidly attained, and (2) in low permeability sand packs (3 Darcy) they observed delayed attainment of steady state with higher air saturations. They reported excellent agreement between calculated and measured air saturations.

Hein *et al.* [1997] used the numerical model (T2VOC) for simulation of their own AS experiments in the cylindrical vessel 1.2m in diameter and 1m deep, filled with silica sand. During the AS experiments, the air flow measurements were conducted above the water surface, along the two orthogonal transects at six radial distances from the center. For the numerical model, the capillary pressure parameters were independently measured, while the relative permeability function was assumed. Comparison of simulated and measured fluxes showed that, near the sparging well, model under predicts the air flux up to 40%, which authors explained by incorrect representation of capillary pressure - saturation relation. Away from the sparging well, much better agreement was observed. From the experimental results they also concluded that zone of influence of the sparging well increases only slightly with

increase of injection flow rate.

Van Dijke *et al.* [1995] used axisymmetric, finite element model based on the mixed form of the Richards equation for the air and the water phase, to validate proposed semi-analytical model for steady air distribution in the homogeneous media. Proposed analytical solution can be used for estimation of zone of influence of the sparging well. However, proposed analytical solution is relatively accurate only in the case of low air saturations. Later, Van Dijke and van der Zee [1998] proposed similar analytical solution for a layered soil. In this case, they recognized three air flow regions that occur at the steady state: (1) the region between the injection point and a lower permeability layer, with primarily vertical flow, (2) the narrow region below the lower permeability layer where lateral flow dominates and where capillary forces are of the same order as gravity forces, and (3) the region above the lower permeability layer and below the water table where also buoyancy-driven vertical flow dominates.

Dror *et al.* [2004] utilized MODFLOW (U.S. Geological Survey) code to quantify the effects of air injection on reduction of hydraulic permeability and effective porosity in aerated regions of their experimental setup. The goal was to investigate applicability of air injection as an alternative hydraulic barriers in order to prevent saline intrusion in coastal areas, or to prevent a contaminant transport. They concluded that air injection provides stable, low conductivity barriers that reduce the water discharge by, at least, an order of magnitude. However, the question remained whether obtained laboratory results are applicable on the field scale.

It can be concluded that all aforementioned models are basically very similar. The main difference is in the numerical method applied to solve governing equations. They all assume Darcy law as governing relation between the phase flux and hydraulic gradient, where the effects of other available phases are expressed through the relative permeability concept. Capillarity effects are introduced through a smooth empirical functions of phase saturations (only in the model of Lundegard and Andersen [1996], the capillarity is neglected). In general, all reported results of application of multiphase models to air sparging have been encouraging. The air flow zone is very well reproduced, in agreement with observed patterns at laboratory or in situ experiments. However, it is also clear that for accurate modeling of real sites, the amount of data required to support the multiphase models usually exceeds the available data.

All of these models neglect in start acceleration effects, and therefore, that was the motive for this study; to analyze acceleration effects on the air/water distribution during the air sparging.

5.2.2 Literature review of experimental facts about air flow pattern during air sparging

Multiphase models inherently produce continuous air phase distribution in the aeration zone of porous media. However, many experiments, conducted at laboratory or in situ scales, revealed that this is not an actual case. Therefore, in this section the reported results on air flow pattern will be summarized and implications on numerical modeling will be discussed.

The laboratory study of Ji *et al.* [1993] was the pioneering work of air flow visualization after its injection into saturated porous medium. They conducted experiments in a 2D transparent tank with approximate dimensions of 29 inch x 34 inch x 1 inch. The tank was filled with various sizes of glass beads in a homogeneous or heterogeneous way, with intention to observe how the injected air is distributed in previously saturated medium, and how is that distribution influenced by bead size, injection flow rate or heterogeneity. Two different flow patterns were reported, depending on the size of the glass beads: (1) for the 0.75mm glass beads or less, the air flows through the bush-like system of discrete channels, and (2) for 4mm glass beads or larger, they observed bubbly flow characterized by the plume of discrete bubbles. The transition zone was reported between 0.75mm and 4mm glass beads implying that in the most natural subsurface conditions, the channel flow regime can be expected. They also found that the air flow pattern is strongly influenced on medium heterogeneity. Increase of the air flow rate expands the air flow region up to some extent, after which, the increase of injection rate increases density of air channels and flux through the existent channels, while the aeration region remains nearly the same.

Other air flow visualization studies, conducted on packed beads or granular soils, are consistent with findings of Ji *et al.* [1993] [Lundegard and LaBrecque, 1995; Leeson *et al.*, 1995; Chen *et al.*, 1996; Semer *et al.*, 1998; Roosevelt and Corapcioglu, 1998; Elder and Benson, 1999; Peterson *et al.*, 1999; Marulanda *et al.*, 2000; Krauss *et al.*, 2003]. Brooks *et al.* [1999] summarized the published experimental observations and, in addition, conducted their

own experiments on glass beads. They characterized the flow pattern through the modified, nondimensional Bond number, as the ratio of buoyancy and capillary forces:

$$N_B = \frac{\Delta\rho\, g\, r_b^2}{\sigma} \frac{r_b}{r_c} \tag{5.1}$$

where r_b is the pore body radius, assumed as equal as the grain radius, σ is the air-water surface tension, and r_c is the pore throat radius. According to this theory, in the case where capillary forces are greater than buoyancy, an additional pressure is required to overcome the capillarity, which can be provided only through the continual air channel from the sparging well. They concluded that channel flow occurs in porous media up to 1 mm to 2 mm of grain size, and for coarser medium the bubble flow pattern is to be expected. According to the Unified Classification System, this transition zone occurs in medium sand. In addition, they admitted that identification of air flow pattern is subjective in nature, and cannot alway be clearly distinguished.

Provided observations have significant implications on numerical modeling of air sparging; above all, on the contaminant removal modeling. Since the air and the water phase are not completely mixed, it is reasonably to expect that the contaminant removal will be significantly overestimated by the numerical models in which complete mixing is inherently assumed. Furthermore, an adequate characterization of simulated site is critically important for reliable numerical modeling. Experiments showed that a minor change of soil structure have significant impact on air distribution. This means that considerable amount of data collection may be required for model input.

5.2.3 Capillary pressure and relative permeability models

Governing equations of motion of the air and the water phase in porous medium are coupled through the capillary pressure, defined as:

$$p_c = p_a - p_w \tag{5.2}$$

where p_c is the capillary pressure, p_a is the air pressure and p_w is the water pressure.

At the pore scale, the capillary pressure is a function of curvature radii of the air-water interface. However, at the macroscopic scale, the capillary pressure function is usually given as a empirical function of phase saturation and should be measured for each specific

location. There are a number of available capillary pressure functions that can be found in the literature, but most frequently used in multiphase models are expressions proposed by van Genuchten [1980] (VG) and Brooks and Corey [1964] (BC). Van Genuchten's expression has a form:

$$p_c = \frac{\rho_w g}{\alpha_{aw}} \left(S_{we}^{-1/m} - 1 \right)^{1/n} \tag{5.3}$$

where α_{aw} and $m = 1 - 1/n$ are the fitting parameters and S_{we} is the effective water saturation given by:

$$S_{we} = \frac{S_w - S_{wr}}{1 - S_{wr}} \tag{5.4}$$

where S_w is the water saturation and S_{wr} is the residual, or irreducible water saturation.

Brooks and Corey model has a form:

$$p_c = p_d \, S_{we}^{-1/\beta_{aw}} \tag{5.5}$$

where p_d is the air entry pressure and β_{aw} is the fitting parameter.

Figure 5.2 shows comparison of VG and BC capillary pressure curves, fitted for the measured drainage data of Borden sand [Demond and Roberts, 1992]. It can be seen that the greatest difference between these two curves is in the zone of full saturation (near $S_w = 1$). A BC curve has clearly defined air entry pressure, that must be exceeded before air can penetrate. In contrast, according to the VG curve, for any capillary pressure higher than zero, some amount of the air will enter the porous region. In the specific case of Borden sand, the BC curve clearly overestimates the air entry pressure, which will as a consequence in numerical simulations, have smaller capillary spreading of air. Rathfelder and Abriola [1998] have numerically analyzed the influence of two curves on the long term simulations of NAPL redistribution in saturated soils. They found that two curves yield different solution behavior, where BC solutions generally produced grater spreading of NAPL, less inclination to penetrate less-permeable layers and poorer spatial convergence behavior.

During the air sparging, air saturations are near full water saturation zone and therefore it can be expected that choice of representative capillary pressure model will have a great impact on simulation results. However, such analysis is lacking in the literature and it is not clear which curve is more appropriate for air sparging simulations.

Expressions for the relative permeability can be obtained by using the capillary pressure/saturation function in hydraulic permeability model of Burdine [1953], or Mualem

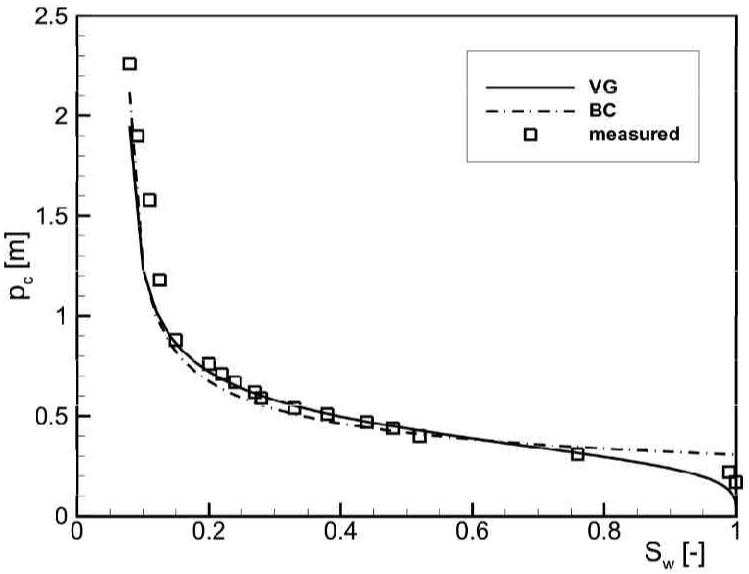

Figure 5.2: Comparison of VG and BC curves with measured capillary pressure/saturation data for Bordline sand

[1976]. VG and the Mualem model produce the following expression for the relative permeability [van Genuchten, 1980]:

$$k_{wr} = S_{we}^{1/2}\left[1-\left(1-S_{we}^{1/m}\right)^{m}\right]^{2} \tag{5.6}$$

$$k_{ar} = (1-S_{we})^{1/2}\left[1-S_{we}^{1/m}\right]^{2m} \tag{5.7}$$

where k_{wr} and k_{ar} are relative permeability functions for the water and the air phase, respectively.

BC and the Burdine model produce:

$$k_{wr} = S_{we}^{(2+3\beta_{aw})/\beta_{aw}} \tag{5.8}$$

$$k_{ar} = (1-S_{we})^{1/2}\left(1-S_{we}^{(2+\beta_{aw})/\beta_{aw}}\right) \tag{5.9}$$

In figure 5.3 the above given relative permeability relations are compared for the Bordine sand. The influence of one phase on the mobility of the other phase is introduced through the nonlinear dependency of phase saturation and its mobility. At the pore space it is a function of fluid properties of both phases, as well as the properties of the porous medium.

5.2.4 Numerical simulation of air sparging laboratory experiments

Numerical model developed in Chapter 3 will be applied for simulation of two dimensional air sparging experiments reported by Ji *et al.* [1993], with intention to analyze the acceleration effects on air flow and distribution. For the convenience, the governing equations solved here are written in the following form:

$$\frac{\partial \alpha_p}{\partial t} + \frac{\partial}{\partial x_j}(\alpha_p V_{pj}) = 0 \tag{5.10}$$

$$\alpha_p \frac{\partial (V_{pi})}{\partial t} + \alpha_p V_{pj}\frac{\partial V_{pi}}{\partial x_j} = -\frac{\alpha_p}{\rho_p}\frac{\partial p_\alpha}{\partial x_i} - \alpha_p g \frac{\partial x_3}{\partial x_i} + \frac{\partial}{\partial x_j}\left(\alpha_p \nu_p \frac{\partial V_{pi}}{\partial x_j}\right) - \lambda_p \alpha_p^2 V_{pi} \tag{5.11}$$

where subscript p denotes the phase (a - for the air and w - for the water). According to the relative permeability concept the parameter in the drag term in equation (5.11) is defined as:

$$\lambda_p = \frac{\mu_p}{\rho_p k}\frac{1}{k_{pr}} \tag{5.12}$$

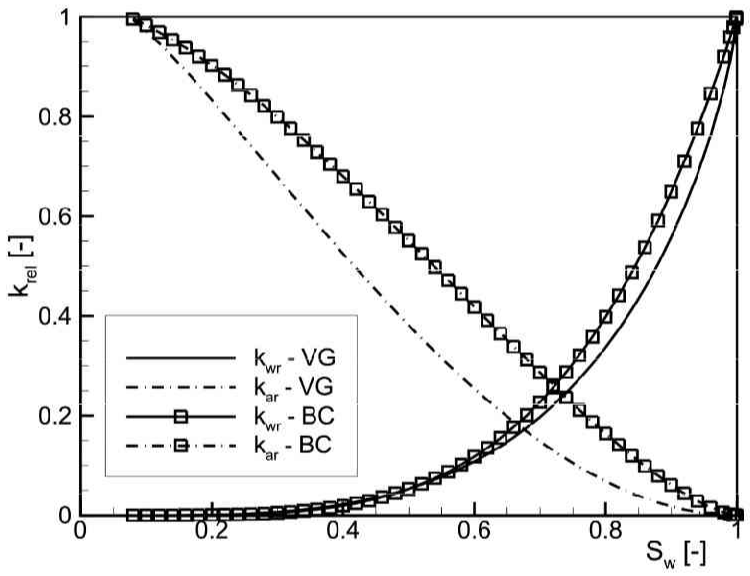

Figure 5.3: Comparison of VG and BC models for relative air/water permeabilities for Bordine sand

Table 5.1: Hydraulic parameters for 0.75 mm and 4.0 mm glass beads after McCray and Falta [1997].

Parameter/bead diameter	0.75 mm	4.0 mm	Units
Intrinsic permeability	$4.9 \cdot 10^{-10}$	$1.0 \cdot 10^{-7}$	[m^2]
Porosity	0.35	0.35	[-]
Water residual saturation	0.15	0.1	[-]
Air residual saturation	0.0	0.0	[-]
Parameter n in VG model	23.6	22.0	[-]
Parameter α_{aw} in VG model	5.99	150.0	[m^{-1}]

The homogeneous experiments with 0.75 mm and 4.0 mm glass beads diameter are chosen for numerical simulation. Hydraulic parameters, essential for numerical simulation, are taken from McCray and Falta [1997] and are shown in Table 5.1. As it can be seen from the presented parameters, the VG model for constitutive relations of capillary pressure and relative permeabilities is utilized.

It should be noted that in the original paper of Ji *et al.* [1993], there was no reported data about hydraulic properties of the glass beads used, except the bead size and porosity. The parameters used here are obtained by semi-empirical methods described in McCray and Falta [1997]. Namely, the intrinsic permeabilities are estimated utilizing the "ratio" method, according to which two permeabilities of different bead diameters are related as:

$$k_2 = k_1 \left(\frac{d_2}{d_1} \right)^2 \tag{5.13}$$

where k_1 is the known intrinsic permeability of glass beads with diameter d_1 and k_2 is the unknown intrinsic permeability of glass beads with diameter d_2. Here, known values of permeabilities from the literature were used. Parameters for capillary pressure/saturation relations where obtained from reported air entry pressures and utilizing the scaling method of Leverett [1941] on referenced data from the literature. Leverett [1941] established the following relation between the capillary pressure, permeability and porosity:

$$p_{cN} = \frac{p_c}{\sigma} \sqrt{\frac{k}{\phi}} \tag{5.14}$$

where p_{cN} is a dimensionless capillary pressure.

Simulation of 0.75mm glass beads experiment

In the case of 0.75mm glass beads experiment, the tank was uniformly filled up to 25 inch from the bottom and additional 4 inches of 4.0mm glass beads were added on the top to prevent the fluidization. From the reported drawings, initial water level is assumed at 24 inch from the tank bottom. The air injection rate chosen for simulation was 10.00 l./min.

For numerical solution, the domain is discretized by 1 inch cubes. To obtain the balance between gravity and capillary forces prior to air injection, the static water level was imposed at the 24 inch level and simulation without air injection was conducted until the equilibrium was reached. This state represented initial condition for the air sparging simulation. The bottom and the side walls are treated as "no flow" boundary condition. The nozzle cell at the bottom is treated as "inactive" cell with constant air flux at the upper face and no fluxes at the remaining faces.

In the experiments, depending on air injection rate and bead size, the water could exit the porous media at the top boundary and form a free water layer above the packing. To simulate this condition, after complete saturation of upper layer, the outwards flux is calculated and accordingly, the free water height above the domain is obtained. Under assumption of hydrostatic pressure in above free water layer, the pressure at the top boundary was imposed.

Figures 5.4 - 5.7 show simulation results of transient air/water distribution after start of air injection. The transient periods of air plume development, described by Lundegard and Andersen [1996], can be clearly observed from these figures: (1) an expansion stage until the air phase reaches the free surface (figures 5.4 and 5.5) and (2) an contraction stage, observed after reaching the free surface (figures 5.6 and Fig5-0-75-4). It can be also noted that the zone near injection point reaches the steady condition faster than the zone near the free surface.

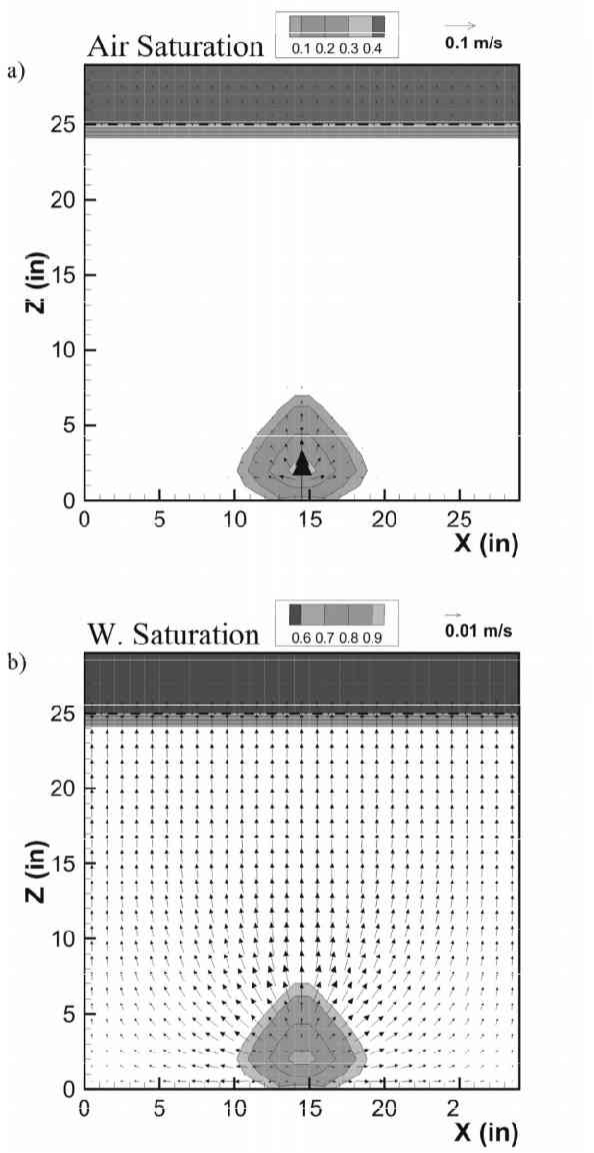

Figure 5.4: Simulation of air injection into saturated 0.75mm glass beads; 0.2s after start of injection: a) air saturation contours and velocity vectors, b) water saturation contours and velocity vectors

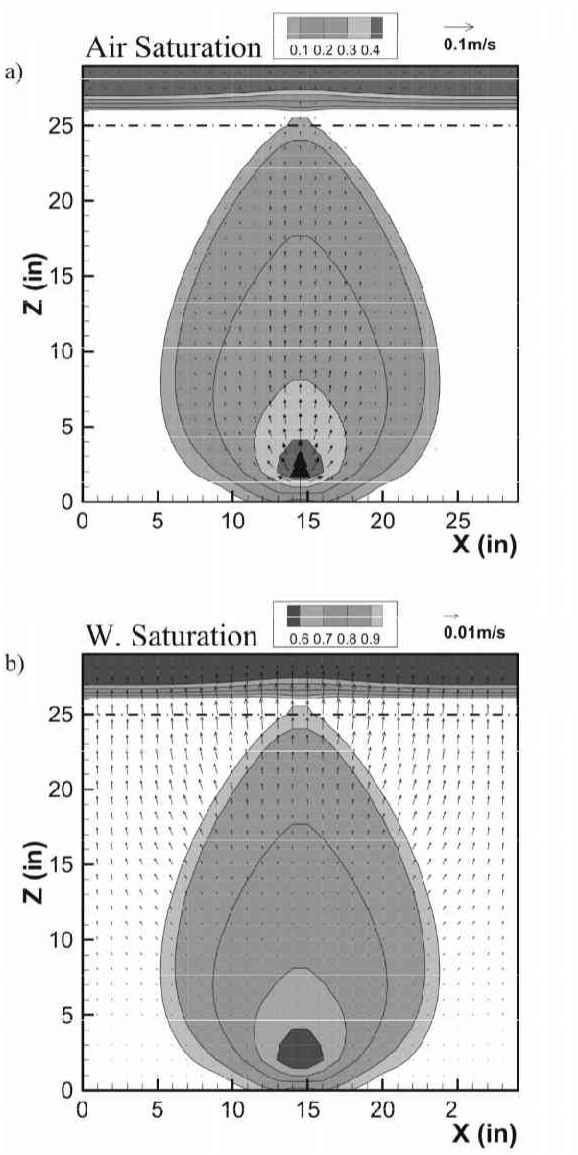

Figure 5.5: Simulation of air injection into saturated 0.75mm glass beads; 2s after start of injection: a) air saturation contours and velocity vectors, b) water saturation contours and velocity vectors

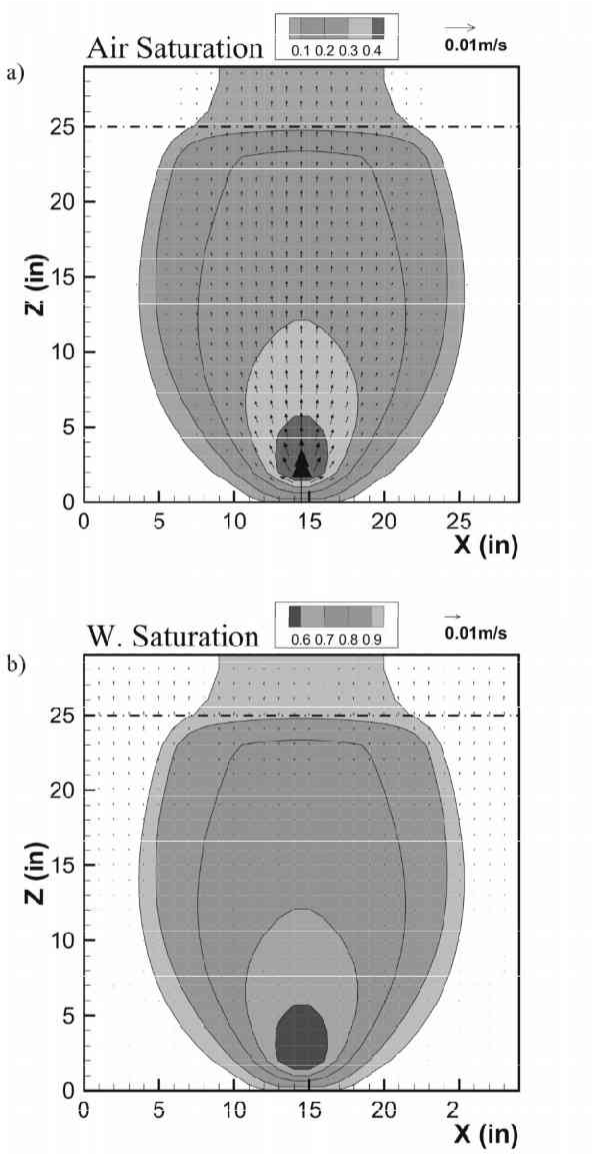

Figure 5.6: Simulation of air injection into saturated 0.75mm glass beads; 4s after start of injection: a) air saturation contours and velocity vectors, b) water saturation contours and velocity vectors

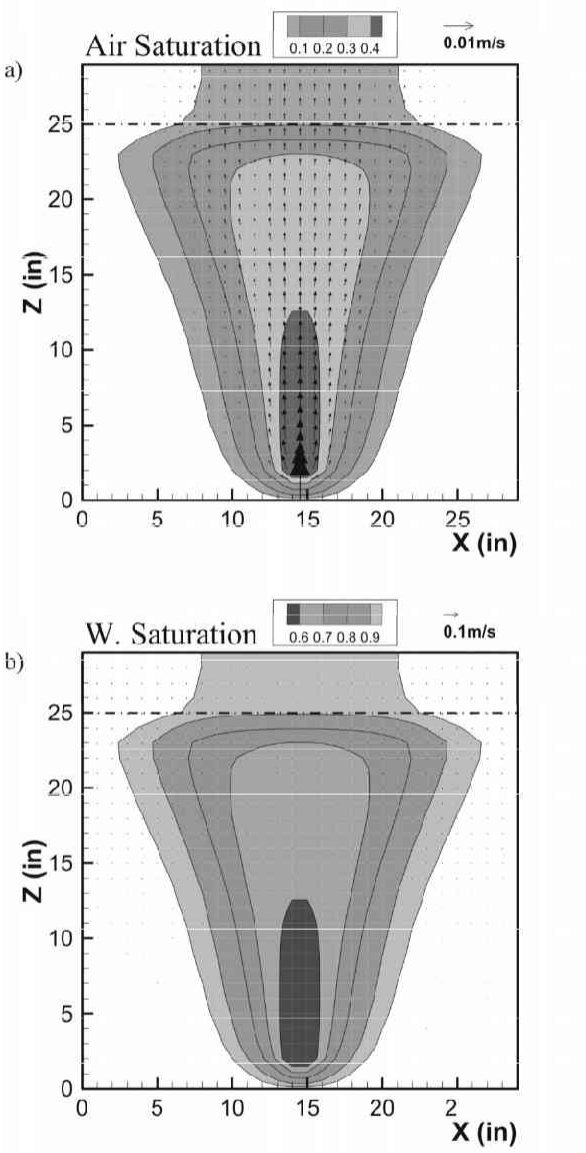

Figure 5.7: Simulation of air injection into saturated 0.75mm glass beads; 15s after start of injection: a) air saturation contours and velocity vectors, b) water saturation contours and velocity vectors

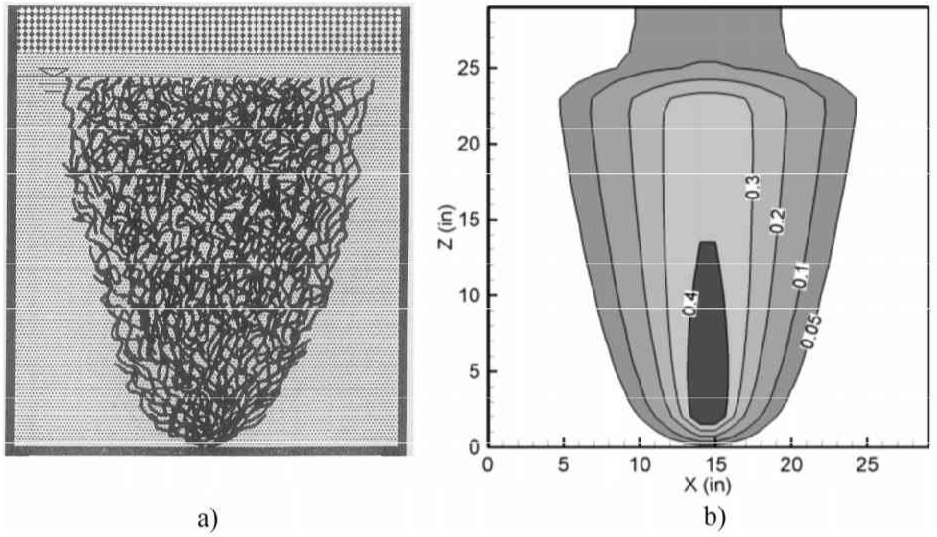

Figure 5.8: Comparison of observed flow pattern and numerical results for 0.75mm glass beads - steady conditions: a) observed flow pattern from Ji*et al.* [1993], b) numerical simulation - steady state air saturation contours (q_{air} = 10.0 L/min).

Qualitative comparison of steady condition air distribution with observed air distribution by Ji *et al.* [1993] is shown in Figure 5.8. Figure 5.4 a) is a drawing taken from the paper of Ji *et al.* [1993] which schematically represents air flow pattern and air phase distribution. The figure also shows initial water level condition. At the steady state, the glass beads above this level (4mm beads) are saturated and water layer over packing is formed. This can be clearly seen from the photographs in the paper. Figure 5.8 b) shows air phase saturation contours from the simulation. The air spreading area has a parabolic shape through the 0.75mm beads, very similar to the observed one. After reaching the 4.0mm beads, due to higher permeability, the air zone is contracted with decrease of air saturation.

Numerical simulations conducted with and without inclusion of acceleration terms revealed that, in this case, acceleration terms in momentum equations (5.11) have negligible influence on air saturation distribution (less than 1%), neither during the transient period of air plume development, or at the steady conditions.

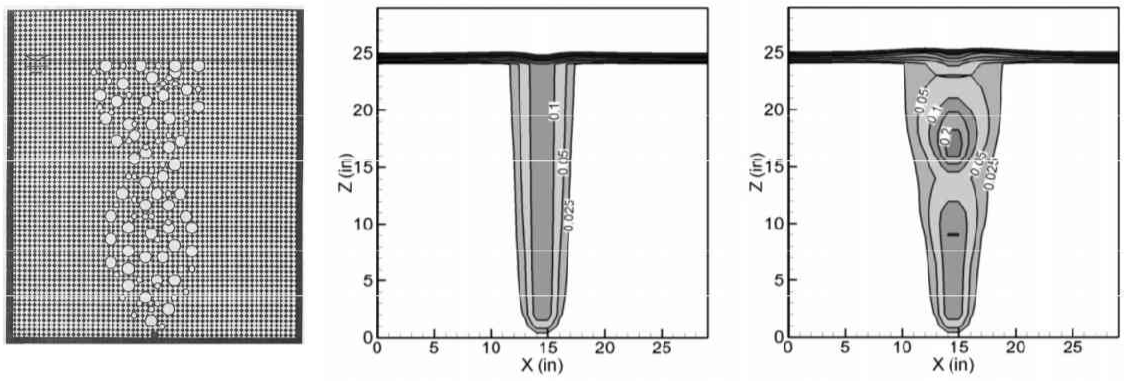

Figure 5.9: Comparison of observed flow pattern and numerical simulation results for 4.0mm glass beads: a) observed flow pattern from Ji *et al.* [1993], b) numerical simulation without acceleration terms in equations (5.11), c) steady pulsation - simulation with acceleration terms. (Contours in b) and c) represent air saturations)

Simulation of 4.0mm glass beads experiment

In the 4mm glass beads experiment, the packing was homogeneous with initial water level at 24 inch from the tank bottom. Simulated injection air flow rate was again $q_{air} = 10.0$ L/min, with the same boundary conditions as in the previous case. In this case the bubbly flow pattern is reported. After increasing the air flow rate and reaching the specific value, the steady pulsation was observed. Pulsation manifested as bubbly stream oscillation shown in Figure 5.9-a). Authors described this behavior as a jet pulsation.

Here, two numerical simulations were conducted: (1) without modeling the acceleration terms in equations (5.11), and (2) simulation with included acceleration terms. Figures 5.9-b) and 5.9-c) show simulation results 5s after the start of air injection for two cases, respectively. The pulsation, observed in experiments, could only be produced by modeling the acceleration terms (Fig. 5.9-c)). Comparison of the figures also shows higher air saturations in the letter case and wider zone of aeration, which better reproduce the experimental results. Numerical results clearly show that inertial forces have the key role in the inception of instability.

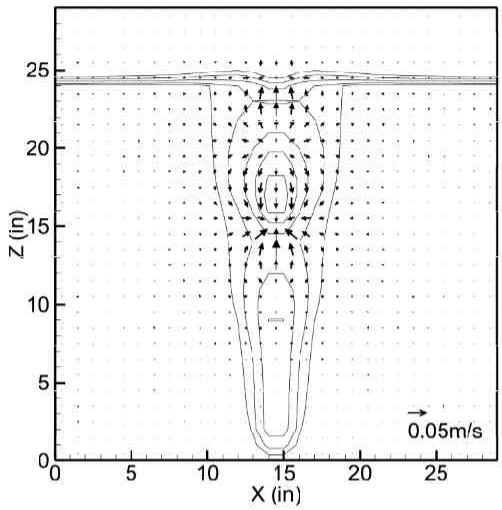

Figure 5.10: Macroscopic water velocities in a case of pulsating air flow. Contour lines represent air saturations from Fig. 5.9-a)

Without the pulsation, the steady state implies that water phase is at hydrostatic condition. However, in the pulsation case, water oscillates as air pulses are passing. At the front of the air pulse, water is moving upward, circulating around the pulse, and replacing the air at the pulse tail. This is shown in Figure 5.10, where the macroscopic fluxes of the water phase are drawn. This behavior certainly has consequences on contaminant removal, due to promoted mechanical mixing.

Inception of instability is reported at air injection rate of about 10 L/min. However, numerical model produced instability significantly earlier, at about 2 L/min. This is attributed to modeling of drag term in momentum equations. As discussed in Chapter 2 of this thesis, it is well known that at higher Raynold's numbers, which can be expected in coarser materials, the Darcy law does not describe well the relation between the hydraulic gradient and fluid velocities. Therefore, the drag term is changed by using the Ergun's [1952] expression which combines Kozeny-Carman equation for viscous loss and Burke-Plummer equation for kinetic loss. The relative permeability function is kept in order to express the influence of other present fluids on the drag term:

$$\frac{R_{pi}}{\rho_p} = -\frac{1}{k_{pr}}\left[\frac{150\nu_p(1-\phi)^2}{\phi^3 D^2} + \frac{1.75(1-\phi)}{\phi^3 D}\left|\alpha_p V_p\right|\right](\alpha_p V_{pi}) \tag{5.15}$$

where D represents the bead diameter.

It should be emphasized here that reliable expressions for the drag force in the case of high velocity multiphase flows and bubbly flows in porous media are still lacking, and that additional experimental work is required to obtain such relations. In the theoretical study of Corapcioglu *et al.* [2004], forces on single bubble in porous media are analyzed and the relative permeability function is taken as a constant. However, in analysis of gas-liquid concurrent flow, Seaz and Carbonell [1985] concluded hat relative permeability is exponential function of the phase content. Wu [2001] obtained analytical solution for a Buckley-Leverett problem for the conditions of non-Darcy flow of immiscible fluids, where he utilized Forchheimer-type equation for the drag terms, very similar in form to equation (5.15). The main difference is that for the viscous term is used a standard relative permeability function and for the kinetic loss term, a empirical expression which is a function of permeability, relative permeability, porosity and effective phase saturation. Equation (5.15) represents extension of Darcy-law equation and can be easily replaced in the developed model with, eventual, more reliable expression.

It is also of interest to examine the influence of instability modeling on the amount of dynamically trapped air as a result of simulation, since it has a great importance in overall efficiency of air sparging technology. Here, three models are compared, which differ only in momentum equations:

Model I (full equations):

$$\alpha_p \frac{\partial (V_{pi})}{\partial t} + \alpha_p V_{pj} \frac{\partial V_{pi}}{\partial x_j} - - \frac{\alpha_p}{\rho_p} \frac{\partial p_p}{\partial x_i} - \alpha_p g \frac{\partial x_3}{\partial x_i} + \frac{\partial}{\partial x_j} \left(\alpha_p \nu_p \frac{\partial V_{pi}}{\partial x_j} \right) - \frac{1}{k_{pr}} \left[\frac{150 \nu_p (1-\phi)^2}{\phi^3 D^2} + \frac{1.75(1-\phi)}{\phi^3 D} |\alpha_p V_p| \right] (\alpha_p V_{pi}) \tag{5.16}$$

Model II (acceleration terms neglected):

$$0 = -\frac{\alpha_p}{\rho_p} \frac{\partial p_p}{\partial x_i} - \alpha_p g \frac{\partial x_3}{\partial x_i} + \frac{\partial}{\partial x_j} \left(\alpha_p \nu_p \frac{\partial V_{pi}}{\partial x_j} \right) - \frac{1}{k_{pr}} \left[\frac{150 \nu_p (1 \quad \phi)^2}{\phi^3 D^2} + \frac{1.75(1-\phi)}{\phi^3 D} |\alpha_p V_p| \right] (\alpha_p V_{pi}) \tag{5.17}$$

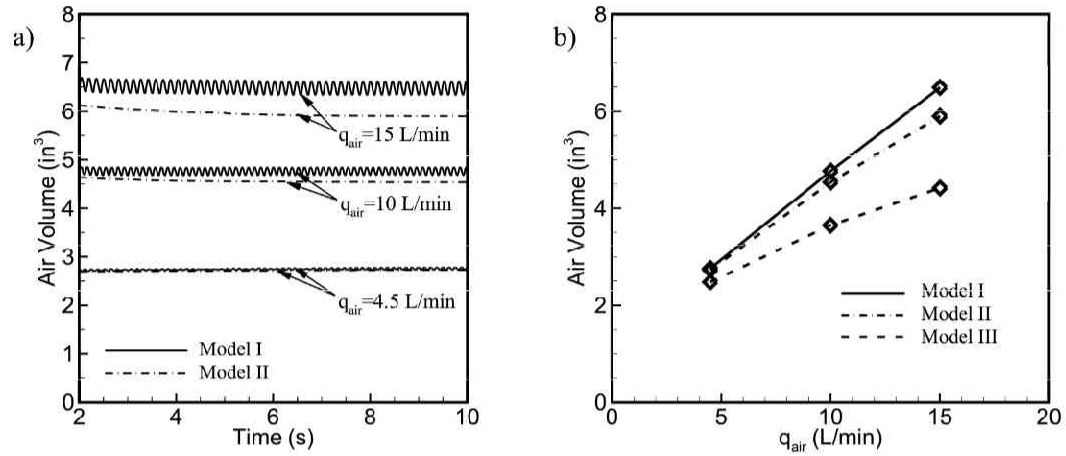

Figure 5.11: Calculated dynamically trapped air volume: a) effect of acceleration terms in momentum equations, b) comparison of Model I, Model II and Model III for different air injection flow rates

Model III (acceleration terms and kinetic drag term neglected):

$$0 = -\frac{\alpha_p}{\rho_p}\frac{\partial p_p}{\partial x_i} - \alpha_p g\frac{\partial x_3}{\partial x_i} + \frac{\partial}{\partial x_j}\left(\alpha_p \nu_p \frac{\partial V_{pi}}{\partial x_j}\right) - \frac{1}{k_{pr}}\left[\frac{150\nu_p(1-\phi)^2}{\phi^3 D^2}\right](\alpha_p V_{pi}) \qquad (5.18)$$

Calculated results are compared in Figure 5.11. It can be seen that effects of acceleration terms start with inception of instability and increase with higher air flow rate and that Model III significantly underestimates dynamically trapped air volume. Inception of instability, which is experimentally observed around 10 L/min of air flow rate, is now in agreement with numerical results. The mechanism of inception of instability will be theoretically analyzed in the following section.

5.2.5 An one-dimensional linear stability analysis of air sparging

A similar instability phenomena, as described in the previous section, has been observed at the downward cocurrent flow of gas and liquid through packed columns, often used in chemical engineering for reactions such as oxidation or hydrogenation [e.g. Grosser *et al.*, 1988; Dankworth *et al.*, 1990]. A linear stability analysis of an one-dimensional macroscopic model described by equations very similar to equations numerically solved in this study, first conducted by Grosser *et al.* [1988] and later in a more detail by Dankworth *et al.* [1990], revealed the role of inertial terms on inception of the instability. They concluded that acceleration promotes growth of perturbations while capillary pressure counteracts the inertial effects. At sufficiently high flow rates, when inertial effects become dominant, the instability occurred. Similar analysis will be conducted here, for the case of air sparging.

Starting point for the stability analysis are 1D governing equations for the air and the water phase in vertical direction:

$$\frac{\partial \alpha_p}{\partial t} + \frac{\partial}{\partial x_3}(\alpha_p V_{p3}) = 0 \tag{5.19}$$

$$\alpha_p \frac{\partial (V_{p3})}{\partial t} + \alpha_p V_{p3} \frac{\partial V_{p3}}{\partial x_3} = -\frac{\alpha_p}{\rho_p}\frac{\partial p_p}{\partial x_3} - \alpha_p g - \frac{R_{p3}}{\rho_p} \quad (p = w,\ a) \tag{5.20}$$

where x_3 is the vertical axis (positive upward), and V_{p3} is the vertical velocity of phase p. System of equations is closed by inclusion of two additional conditions:

$$\alpha_a + \alpha_w = \phi \tag{5.21}$$

$$p_a - p_w = p_c = f(\alpha_w) \tag{5.22}$$

Now, an uniform, steady state can be assumed, around which a perturbation will be imposed. The steady state for the case of air sparging implies that water phase is stagnant, and can be characterized by following set of equations:

$$\overline{V_{w3}} = 0 \tag{5.23}$$

$$\frac{d}{dx_3}(\overline{\alpha_a}\,\overline{V_{a3}}) = 0 \tag{5.24}$$

$$0 = -\frac{\overline{\alpha_a}}{\rho_a}\frac{d\overline{p_a}}{dx_3} - \overline{\alpha_a} g - \frac{\overline{R_{a3}}}{\rho_a} \tag{5.25}$$

where the overline represents a steady variable value.

A perturbation around the uniform, steady condition can be imposed by introducing:

$$\alpha_p(x_3,t) = \overline{\alpha_p} + \alpha'_p(x_3,t) \tag{5.26}$$

$$V_{p3}(x_3,t) = \overline{V_{p3}} + V'_{p3}(x_3,t) \tag{5.27}$$

$$p_p(x_3,t) = \overline{p_p} + p'_p(x_3,t) \tag{5.28}$$

where α'_p, V'_{p3} and p'_p are infinitesimal disturbances for phase content, velocity and pressure, respectively.

By substitution of equations (5.26) ... (5.28) into equations (5.19) and (5.20) and after linearisation, two continuity and two momentum equations can be reduced to a single equation, e.g. in terms of perturbation from the uniform state of the water content:

$$A\frac{\partial \alpha'_w}{\partial t} + B\frac{\partial \alpha'_w}{\partial x_3} + C\frac{\partial^2 \alpha'_w}{\partial t^2} + D\frac{\partial^2 \alpha'_w}{\partial t\,\partial x_3} + E\frac{\partial^2 \alpha'_w}{\partial x_3^2} = 0 \tag{5.29}$$

where coefficients $A \ldots E$ depend on uniform state variables and are given as:

$$A = -\frac{1}{\overline{\alpha_w}^2}\overline{\left(\frac{\partial R_{w3}}{\partial V_{w3}}\right)} - \frac{1}{\overline{\alpha_a}^2}\overline{\left(\frac{\partial R_{a3}}{\partial V_{a3}}\right)} \tag{5.30}$$

$$B = \frac{1}{\overline{\alpha_w}}\overline{\left(\frac{\partial R_{w3}}{\partial \alpha_w}\right)} - \frac{1}{\overline{\alpha_a}}\overline{\left(\frac{\partial R_{a3}}{\partial \alpha_a}\right)} - \frac{\overline{R_{w3}}}{\overline{\alpha_w}} - \frac{\overline{R_{a3}}}{\overline{\alpha_a}} - \frac{\overline{V_{w3}}}{\overline{\alpha_w}^2}\overline{\left(\frac{\partial R_{w3}}{\partial V_{w3}}\right)} - \frac{\overline{V_{a3}}}{\overline{\alpha_a}^2}\overline{\left(\frac{\partial R_{a3}}{\partial V_{a3}}\right)} \tag{5.31}$$

$$C = \frac{\rho_w}{\overline{\alpha_w}} + \frac{\rho_a}{\overline{\alpha_a}} \tag{5.32}$$

$$D = 2\left(\overline{V_{w3}}\frac{\rho_w}{\overline{\alpha_w}} + \overline{V_{a3}}\frac{\rho_a}{\overline{\alpha_a}}\right) \tag{5.33}$$

$$E - \overline{V_{w3}}^2\frac{\rho_w}{\overline{\alpha_w}} + \overline{V_{a3}}^2\frac{\rho_a}{\overline{\alpha_a}} + \overline{\left(\frac{\partial p_c}{\partial \alpha_w}\right)} \tag{5.34}$$

A perturbation from the uniform state can be imposed in a sinusoidal form as:

$$\alpha'_w = \widehat{\alpha}\,\exp\left[i(\chi x_3 - \omega t)\right] \tag{5.35}$$

where χ is the wave number of the perturbation, ω is the frequency and $i = \sqrt{-1}$. By requiring that imaginary part of ω equals zero, and taking into account that uniform condition implies stagnant water phase, a neutral condition can be obtained in a form:

$$A^2E - ABD + B^2C = 0 \tag{5.36}$$

or, by substitution of equalities (5.30) ... (5.34) into (5.36), the same can be expressed as:

$$\frac{\rho_a}{\alpha_a}\overline{V_{a3}}^2 + F^2\left(\frac{\rho_a}{\alpha_a} + \frac{\rho_w}{\alpha_w}\right) + \overline{\left(\frac{\partial p_c}{\partial \alpha_w}\right)} - 2F\frac{\rho_a}{\alpha_a}\overline{V_{a3}} = 0 \tag{5.37}$$

in which $F = B/A$.

Analysis of terms in equation (5.37) shows that first two terms are always positive, promoting the instability, and that last two terms on the left side are always negative, opposing the instability. It can be concluded that significance of these terms, in each specific case, determines the occurrence of the instability.

Denoting the left side of equation (5.37) as Ω, its value can be calculated for several air injection flow rates. This is shown in Figure 5.12, where calculation is conducted for 0.75mm and 4.0mm glass beads. Uniform, steady state variables are obtained numerically, solving the equations (5.23) ... (5.25).

From the Figure 5.12, it can be concluded that for the 0.75mm glass beads case, the flow is always stable, regardless of air flow injection rate. However, in the case of 4.0mm glass beads, instability occurs for the air pore velocities higher than $\approx$ 0.15m/s. This is in accordance with numerical experiments, but also with experimental results where no pulsation is reported for 0.75mm glass beads.

In order to delineate more precisely the bead sizes associated with instability, the same procedure is conducted for 2mm and 3mm beads. Parameters for capillary pressure and relative permeability curves are scaled from the estimated values for 0.75mm beads, by using the Leverett [1941] scaling procedure. Obtained values of those parameters, as well as the value of estimated permeabilities, are shown in Table 5.2. The permeability is calculated from the Ergun equation of viscous drag in a packed bed, assuming the same porosity as in the case of 0.75mm beads:

$$k = \frac{D^2}{150}\frac{\phi^3}{(1-\phi)^2} \tag{5.38}$$

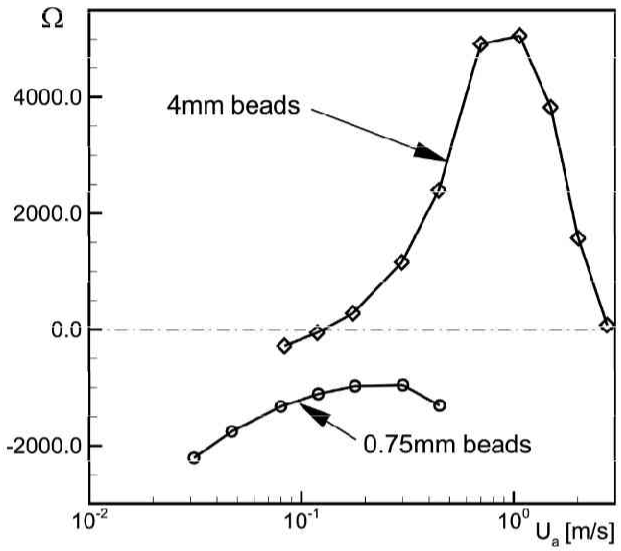

Figure 5.12: Diagram of Ω values in function of air pore velocity for 0.75mm and 4.0mm glass beads

Table 5.2: Approximated parameter values for 2mm and 3mm glass beads.

Parameter/bead diameter	2.0 mm	3.0 mm	Units
Intrinsic permeability	$2.71 \cdot 10^{-9}$	$6.1 \cdot 10^{-9}$	[m^2]
Porosity	0.35	0.35	[-]
Water residual saturation	0.1	0.1	[-]
Air residual saturation	0.0	0.0	[-]
Parameter n in VG model	23.0	23.0	[-]
Parameter α_{aw} in VG model	16.0	23.0	[m^{-1}]

Figure 5.13 shows calculation of Ω for 2mm and 3mm beads. Values of specific terms on the left side of equation (5.37) are also shown, where "Term1" ..."Term4" denote the first, second, third and the fourth term, respectively. It can be observed that the first and the fourth term are negligible in comparison with the second and the third, where the second term comprises inertial and drag forces, and the third term represents the capillary force.

According to Figure 5.13, the instability may occur for beads larger than 2mm. For 3mm glass beads, the instability occurs for air pore velocity larger than 0.3m/s, which is quite large for flow in porous medium. As the bead diameter increases, the critical pore air velocity decreases (0.3m/s for 3mm beads and 0.15m/s for 4mm beads), as indeed should be, due to lower capillary forces for larger beads. The role of capillary pressure in prevention of instability can easily be proved by neglecting the third term in equation (5.37), which shows that the flow would always be unstable.

Numerical experiments, for the conditions as in the experiments of Ji *et al.* [1993], revealed that instability occurs for bead diameters larger than 3mm. Considering that theoretical analysis was conducted for 1D case, and that numerical solution inherently dampens the occurrence of instability, the agreement can be considered as quite encouraging.

Clearly, the shape (gradient) of the capillary pressure curve has important role on instability inception. Moreover, the shape in the near full saturation zone is the most important for the coarser materials, where instability can be expected. As it has been shown earlier, the most significant difference between BC and VG functions is exactly in this zone. Since the above analysis was conducted using the VG curve, the applicability of the BC curve will also be examined. Parameters for the BC capillary pressure curves are fitted to best match with obtained VG curves. Table 5.3 shows fitted parameters for 0.75 mm, 2.0 mm, 3.0 mm and 4.0 mm glass beads, respectively. Comparison of capillary curves for 0.75 mm beads is shown in Figure 5.14. Relative permeability curves are kept the same as before, in order to analyze only the effects of capillary model on calculated results. Therefore, only the third term in equation (5.37) is changed, while the other, unform, steady state variables are the same as in the previous calculations with VG model. The fact that steady variables do not change with the change of capillary pressure curve can be easily seen from equation (5.25).

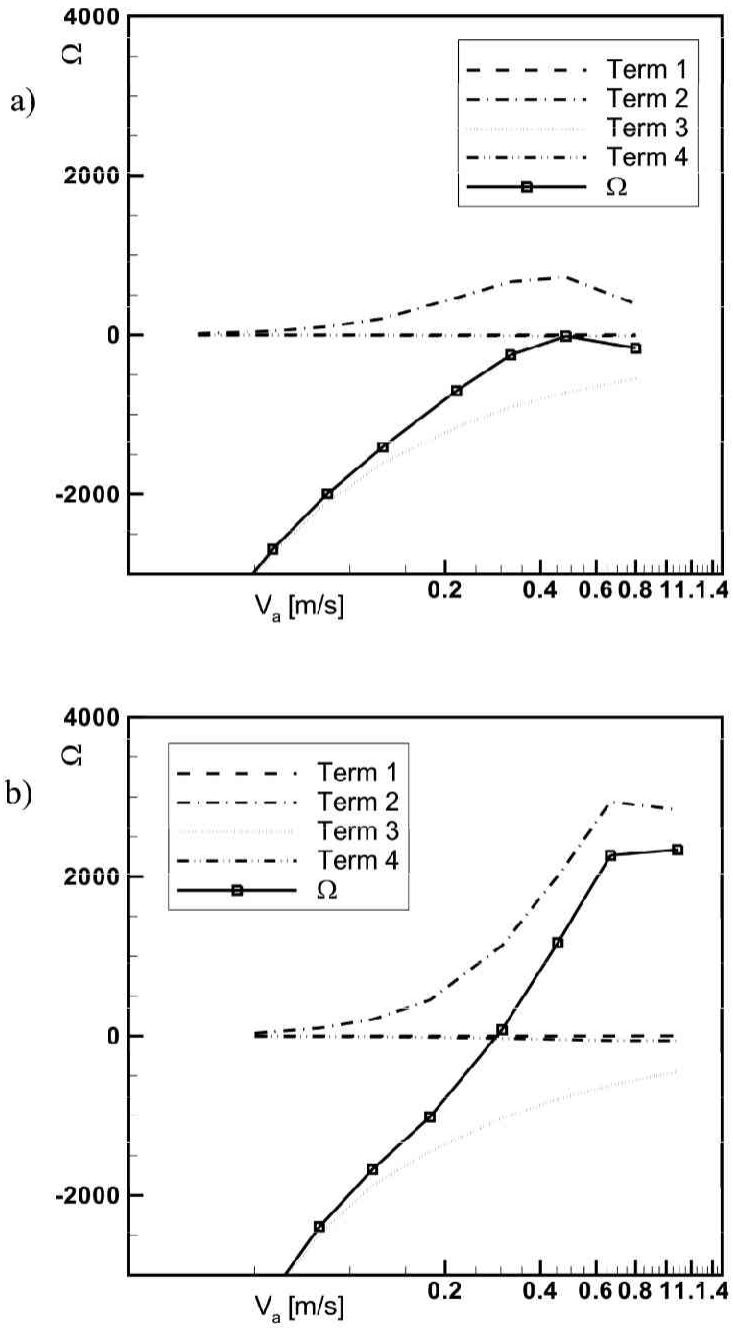

Figure 5.13: Diagram of Ω values in function of air pore velocity for 2.0mm and 4.0mm glass beads: a) 2.0mm glass beads, b) 3.0mm glass beads.

Table 5.3: Fitted parameters of the Brooks-Corey capillary pressure curve for 0.75mm, 2mm, 3mm and 4mm glass beads.

Parameter/bead diameter	0.75 mm	2.0 mm	3.0 mm	4.0 mm
Parameter p_d in BC model	0.15	0.055	0.037	0.028
Parameter β_{aw} in BC model	9	9	9	9

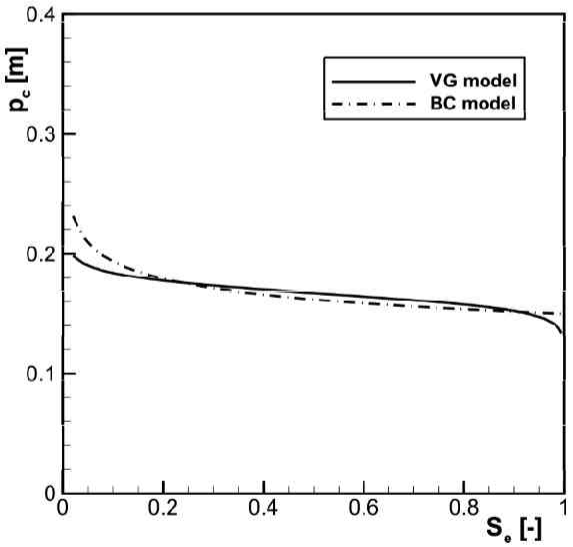

Figure 5.14: Comparison of fitted VG and BC capillary pressure curves for 0.75mm glass beads.

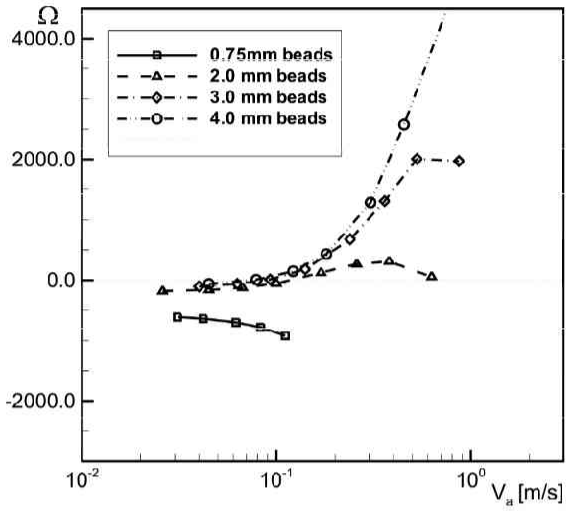

Figure 5.15: Calculated values of neutral stability function for different diameter glass beads, using the BC capillary pressure model.

Figure 5.15 shows calculated values of Ω function for different sizes of glass beads. Generally, critical values of air pore velocities are decreased in comparison with VG model. This was expected, considering the shapes of characteristic capillary pressure curves. However, the general conclusion remains the same, that instability may occur for 2mm beads and larger. Recalling reported transition zone between the channel and the bubble flow between 1mm and 2mm bead size [Brooks *et al.*, 1999], it can be concluded that instability can be expected in the bubble flow regime only.

Considering experimentally obtained capillary pressure curves for different types of materials [e.g. van Genuchten, 1980], especially in the zone near complete saturation, it is reasonable to assume that the VG model produces better matching. Therefore, here obtained results, using this model can be considered as more reliable in comparison with the BC model.

It is well known that the capillary pressure function is a multiple value function, depending on saturation history, i.e. of wetting/drying process [e.g. Luckner *et al.*, 1989]. Therefore, the question arises which particular curve is relevant in terms of instability inception, since different curve would produce different stability criteria (as showed previously

for VG and BC models). Argumentation presented by Grosser *et al.* [1988] for trickling to pulsing transition during the downward, cocurrent gas/water flow can be also applied for the air sparging analysis. They concluded that drainage curve produces the loss of stability for the lowest gas/water fluxes, and therefore, should be taken as adequate. Indeed, the term $\overline{\partial p_c/\partial \alpha_w}$ in equation (5.37) has minimal values for the drainage curve, and therefore will provide the minimal stabilizing resistance to inertial effects.

5.3 Modeling of contaminant removal during air sparging

In order to simulate application of the air sparging (AS) system, an appropriate contaminant transport model has to be applied concurrently with the air/water flow model. This is the topic of this section; firstly, the literature review of reported modeling and experimental studies of mass transfer during AS will be presented, and secondly, the presented model will be extended by inclusion of all important phenomena in relation with contaminant transport during the AS.

5.3.1 Literature review of reported numerical models

There are generally two categories of models for simulation of contaminant removal during AS [Rabideau and Blayden, 1998; McCray, 2000]: (1) mechanistic, multiphase models, based on multidimensional governing flow and transport equations, and (2) simplified, so called "reactor" models, where mass removal is related to the quantity of fluids circulating in the reactor zone. Both approaches offer some advantages, but also have some inherent drawbacks.

Multiphase (mechanistic) models potentially offer better understanding and more accurate air/water flow and transport processes under sparging conditions. However, they require a substantial amount of input data, which include detailed physical soil properties, such as porosity, permeability, relative permeability characteristics and capillary pressure functions. Reliable parameters of contaminant transfer between the phases are also required, although some processes, such as diffusion/dispersion of contaminant toward air channels, are not resolved satisfactorily at the pore scale yet. Earlier mentioned models of Unger *et al.* [1995], and McCray and Falta [1996] are mechanistic ones. In these models, hydrodynamics

and mass transport within each phase is simulated for hypothetical (study) cases with intention to resolve the main mechanisms which influence the effectiveness of the AS system. Although, the applications of these models have provided a valuable insight into governing mechanisms of contaminant removal, both are based on assumption of complete mixing and equilibrium partitioning of contaminant between the phases, which can be expressed by Henry's law:

$$C_a - K_H C_w \tag{5.39}$$

where C_a and C_w are the contaminant concentrations in the air and the water phase, respectively, and K_H is the Henry's constant (nondimensional). It has been showed in several studies that equilibrium partitioning assumption may not be applicable [e.g. Cho and Jaffe, 1990; Elder *et al.*, 1999; Rabideau *et al.*, 1999].

Reactor (lumped parameter) models are significantly simpler. Generally in models reported in the literature, the AS zone is divided into two or three compartments, for which a simple mass conservation equations are solved. Compartments represent a water, air (two compartments) and mass interchange compartment (three compartments). Mass interchange compartment is usually introduced in order to account some processes, such as diffusion toward air channels, biodegradation, sorption and desorption from the soil phase etc. Transfer of contaminants between the phases are modeled by equilibrium assumption, or through the lumped parameters of mass transfer rate between the compartments.

Rabideau *et al.* [1999] proposed a reactor model which takes into account diffusion of contaminant toward the air channels. They succeeded to reconstruct source zone tailing and rebound behavior, often observed at the air sparging sites, as well as in laboratory experiments [Semmer and Reddy, , 1998; Chao *et al.*, 1998; Adams and Reddy, 1999; Kirtland and Aelion, 2000; Benner *et al.*, 2000; Peterson *et al.*, 2000; Braida and Ong, 2000, Rogers *et al.*, 2004]. In this model the sparging region is modeled as a reactor consisting of two mixed compartments, where only one of these compartments exchanges mass with the air phase. They assumed two main processes affecting the mass removal: desorption from the soil phase and diffusion of contaminant in the water phase. Model was applied on in situ AS system, where the system of 36 sparging wells, distributed on approximately 2500 m^2, is simulated as a single one. Model parameters were calibrated from the early stage of air sparging course, and applied for

prediction of sparging effects over 3-years operating period. They concluded that about 18% of pore space was influenced by AS, and the remaining was not, with the diffusion toward air channel as limiting factor. They also showed that pulsing strategy of AS system is beneficial in terms of remediation efficiency. Proposed model, however, does not include (as the most of other reported reactor models) transport of contaminants by the air phase and advection by the water phase.

Somewhat different approach is proposed by Elder *et al.* [1999]. This model considers air flow in discrete air channels, diffusion between the air channels and rate limited mass transfer into the air phase. Water phase is assumed as stationary and sorption is neglected. Air phase distribution is assumed in this model, based on air injection flow rate. Model was applied to simulate reported experimental air sparging results from literature, where it showed a good agreement with measured mass removal. In the model, water phase is also considered as stagnant.

Several lumped-parameter models were proposed to simulate one-dimensional laboratory experiments conducted on soil columns. By their calibration with measured mass removal, important model parameters can be obtained, such as air-water mass transfer coefficient [e.g. Chao *et al.*, 1998; Braida and Ong, 2000] , or diffusion/dispersion coefficient of contaminants in saturated soil.

Described models proposed by Rabideau *et al.* [1999] and Elder *et al.* [1999] are typical reactor models, and models proposed by other authors are conceptually very similar. Some of them include an additional processes which may effect contaminant removal. Wilson *et al.* [1994] and Wilson *et al.* [1997]. for example, accounted a dissolution process of NAPL droplets into the water phase and its diffusion toward the air channels.

These models, inherently cannot predict air distribution in the zone of aeration, and therefore, it has to be assumed. This in turn, may produce difficulties in the cases with significant heterogeneity. In addition, water phase is treated as stagnant and effects of groundwater flow can not be simulated; for example, when air sparging also serves to prevent migration of contaminant due to existence of natural hydraulic gradient.

Many laboratory and in-situ experimental studies conducted since the early 1990's provided better understanding on factors and mechanisms controlling mass removal of contaminants during the AS. Some of them were focused on removal of trapped, non-aqueous

phase [Braida and Ong, 2000; Rogers *et al.*, 2004] and some were focused on remediation of dissolved contaminants [Chao *et al.*, 1998; Reddy and Adams, 2000; Peterson *et al.*, 2000; Braida and Ong, 2001]. Considering reported experimental results, several common points can be emphasized:

- Air sparging is more effective in coarser soils. Chao *et al.* [1998] argued that this can be attributed to higher number of air channels which develop in coarser soil in comparison with fine materials, and faster diffusion of VOCs in coarser materials.
- In the early stage of air sparging, contaminants within air channels are removed first. Therefore, volatility characteristics of contaminants (vapor pressure, Henry's constant) govern sparging efficiency.
- After an initial period, contaminant removal is limited by in water mass transport. Here, most of researches agree that contaminant diffusion in water phase is limiting process. Therefore, the volatility of contaminant does not significantly influence sparging efficiency, but dissolved contaminant concentrations [Johnson *et al.*, 2001].
- Increase of the air flow rate, enhances sparging efficiency up to some limit. After that, the mass removal is not influenced by air injection rate.

5.3.2 Model formulation

Mechanisms affecting volatile contaminant removal during an in-situ AS include: air advection, air diffusion/dispersion, volatilization, water advection, water diffusion/dispersion, sorption/desorption and chemical/biological reactions. Depending on soil and contaminant properties, as well as sparging strategy, some of these processes can be more or less significant.

It is assumed that a continuous film of water, as a wetting fluid, coats the soil grains sot that mass transfer between the soil and air is possible only via the water phase [e.g. Armstrong *et al.*, 1994]. Water phase is divided into two compartments, which coincide with the "clear" and the "dirty" zones in the conceptual model of Rabideau *et al.* [1999]. As shown in Figure 5.16, the immobile water compartment is in contact with the air phase, while the mobile water compartment is not. Partitioning of contaminant between the water and the soil phase is assumed as an instantaneous equilibrium for both water compartments.

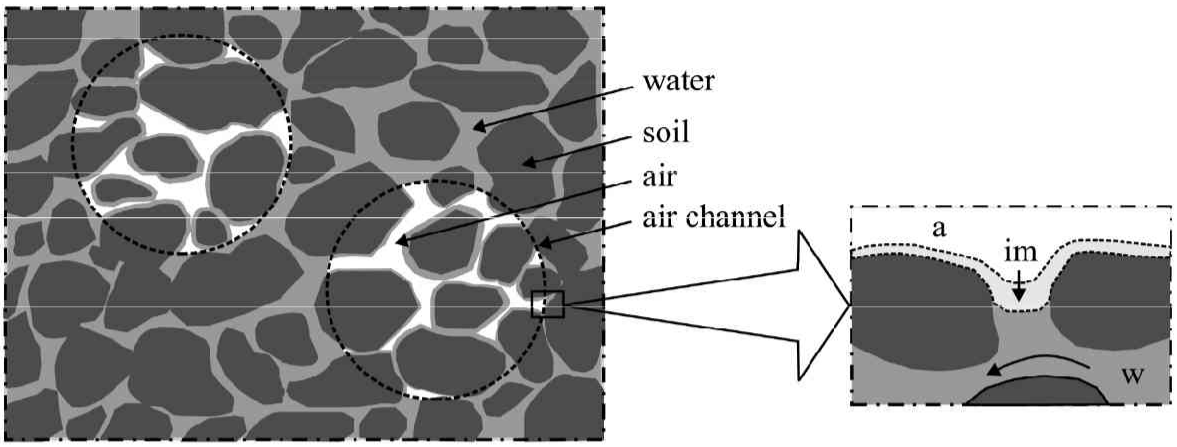

Figure 5.16: Schematic representation of air channels and air (a), immobile (im) and mobile water (w) phases.

The mass conservation equations for the air, immobile water and mobile water phase in Cartesian coordinates can be written as:

$$\frac{\partial(\alpha_a C_a)}{\partial t} = -\frac{\partial(C_a \alpha_a V_{ai})}{\partial x_i} + K_{wa} A (K_H C_{wi} - C_a) \tag{5.40}$$

$$\frac{\partial(\alpha_{im} C_{im})}{\partial t} = -K_{wa} A (K_H C_{im} - C_a) + K(C_w - Cim) - \rho_b f K_d \frac{\partial C_{im}}{\partial t} \tag{5.41}$$

$$\frac{\partial(\alpha_w C_w)}{\partial t} = -\frac{\partial(C_w \alpha_w V_{wi})}{\partial x_i} + \frac{\partial}{\partial x_i}\left(\alpha_w D_{ij} \frac{\partial C_w}{\partial x_j}\right) - K(C_w - Cwi) - \rho_b (1-f) K_d \frac{\partial C_w}{\partial t} \tag{5.42}$$

where C_a, C_{im} and C_w are the air, immobile water and mobile water contaminant concentrations, K_{wa} is the air-water mass transfer coefficient, A is the contact surface between air and water phase, per unit volume of porous media, K_H is the Henry's constant, K is the immobile-mobile water transfer coefficient, ρ_b is the soil dry bulk density and D_{ij} is the water dispersion tensor. The contaminant dispersion tensor in the water phase is given by [Bear, 1972]:

$$\alpha_w D_{ij} = (a_l - a_t)\frac{\alpha_w V_{wi}\ (\alpha_w V_{wj})}{|\alpha_w V_w|} + a_t\,|\alpha_w V_w|\,\delta_{ij} + \alpha_w \tau D^* \delta_{ij} \tag{5.43}$$

where a_l and a_t are the longitudinal and transverse dispersivities, respectively, and δ_{ij} is the Kronecker delta. The product τD^* represents the effective diffusion coefficient for the porous media, comprising the effects of nonlinearity of diffusive paths, where the tourtosity factor

(τ) can be calculated according to Millington and Quirk [1959] expression:

$$\tau = \phi^{4/3} \tag{5.44}$$

As can be seen from equations (5.41) and (5.42), the transfer of mass between the immobile and mobile water compartment is represented by first-order kinetic relation, where the driving force is concentration gradient between two compartments. Since the thickness of immobile zone can not be explicitly measured, the mass transfer coefficient K represents a lumped parameter, comprising all nonlinearities and non-equilibrium processes in this diffusive transport of contaminant toward the air phase.

The air-water mass transfer coefficient can be estimated (K_{wa}) according to the two-film theory [Elder *et al.*, 1999]. According to this theory, the resistance for mass transfer at the interface comprise the resistance of the air and the water film. The air film resistance can be calculated from the empirical function of the Sherwood number:

$$N_{Sh} = \frac{k_a d_c}{D_a} = 1.615 \left(\frac{d_c}{L}\right)^{1/3} (N_{Re} N_{Sc})^{1/3} \tag{5.45}$$

where k_a is the mass transfer coefficient of the air film, d_c is the air channel diameter, L is the air channel length, D_a the air diffusion coefficient, and N_{Re}, N_{Sc} are the Reynolds and Schmidt numbers, respectively, defined as:

$$N_{Re} = \frac{V_a d_c}{\mu_a} \tag{5.46}$$

$$N_{Sc} = \frac{\mu_a}{\rho_a D_a} \tag{5.47}$$

where μ_a is the air viscosity, ρ_a the air density and .

For the calculation of the water film resistance, the penetration theory (Bird *et al.*, 1960) can be utilized:

$$\frac{1}{k_w} = \frac{\pi d_c}{4} \left(\frac{L}{D_L \alpha_a V_a}\right)^{1/2} \tag{5.48}$$

Now, the air-water mass transfer coefficient can be derived as:

$$K_{aw} = \left(\frac{1}{k_a} + \frac{K_H}{k_w}\right)^{-1} = \left[\frac{d_c^{2/3} L^{1/3}}{1.615 D_a \left(N_{Re} N_{Sc}\right)^{1/3}} + \frac{d_c \pi K_H}{4} \left(\frac{L}{D_L \alpha_a V_a}\right)^{1/2}\right]^{-1} \tag{5.49}$$

The air-water interface area can be estimated by assumption that air channels are evenly distributed in the horizontal plane of one calculation cell:

$$A = \frac{4\alpha_a}{d_c \sqrt{\tau_c}} \tag{5.50}$$

where τ_c it the channel tortuosity, the ratio of the effective linear channel length and its apparent length [Elder and Benson, 1999].

Equilibrium partitioning between the dissolved and the solid phase (sorpiton/desorption) is modeled as a Freundlich isotherm:

$$C_s = K_d [f C_{im} + (1 - f) C_w] \tag{5.51}$$

where C_s is the soil concentration (mass per unit mass), K_d is the distribution coefficient, usually expressed as a product of mass fraction of organic carbon in the soil and organic carbon partitioning coefficient ($K_d = f_{oc} K_{oc}$). It is also assumed that sorbent is uniformly distributed between immobile and mobile water, resulting that fraction of sorbent associated with immobile water can be calculated as:

$$f = \frac{\alpha_{im}}{\alpha_{im} + \alpha_w}. \tag{5.52}$$

The immobile water compartment, conceptually introduced in this model, mimics the mass transfer zone (MTZ), or zone directly influenced by the air channel. This zone is experimentally investigated by Braida and Ong [2001] on a single air channel experimental setup. Their unique setup consists of an air tunnel (representing the air channel), 1.58mm high, over saturated, uniformly contaminated porous media placed in an acryl tank, so that air-water contact surface is known. For given air flow rate, transient concentration changes were measured at the different lengths from the air channel. They arbitrarily defined this zone as a distance from the air channel to where the contaminant concentration was 90% of the bulk concentration for quasi-steady conditions. Reported MTZ ranged from 17mm to 41mm. However, in another paper [Braida and Ong, 2000], authors tried to numerically simulate conducted experiments on a soil column, by simulation of a system of air channels. Reported MTZ zone was about an order of magnitude less than in the single air channel case. Considering that both experiments were conducted with stagnant water phase (no mixing by advection), with saturated air (no water advection toward air channels due to evaporation), it is reasonable to assume that in near field conditions, the MTZ zone is significantly smaller. Therefore, in the presented model, the immobile water compartment is taken as the residual water content.

As it can be seen from equation (5.40), the diffusion transport in the air phase is not included, although, the diffusion coefficient in the air is usually three orders of magnitude

higher than in the water phase. Conceptually, presented model does not treat the air phase as completely continuous, but distributed in a number of discrete air channels, surrounded by the water phase. Therefore, there is no contaminant diffusion/dispersion between the channels. Considering the longitudinal dispersion, and recalling that concentration source is distributed along the air channel, it is assumed as negligible in comparison with air advection, which was confirmed by numerical experiments.

5.3.3 Validation of the air-water mass transfer estimate

There are two important parameters in the mass transport/transfer model: the air-water mass transfer coefficient (K_{wa}) and mobile-immobile water mass transfer (K). Generally, the air-water interface area (A) can not be experimentally determined. Therefore, it is a common practice to measure the lumped value of mass transfer (K_{wa}A). The same approach for the $K_{wa}A$ modeling is used in the conceptual model of Elder et al. (1999), however, no explicit validation of equations (5.49) and (5.50) is published in the literature yet. That was the main motive of the study described in this section.

In order to validate adopted method for estimation of the air-water mass transfer, it will be applied on published experimental results. Chao et al. [1998] reported one-dimensional experiments in order to investigate air-water mass transfer of VOCs. Their experimental setup consisted of a Plexiglas column, 9.5 cm in diameter and 40.6 cm in height, in which the clean soil was placed. The soil was then saturated with contaminated water, sealed and allowed to equilibrate before air injection. Air was injected into the bottom of the column and concentration of VOCs in the effluent air was measured periodically. From the simple mathematical model, the best fitting values of the air-water mass transfer were reported. For model validation in this study, the experiments with coarse sand are used.

The one-dimensional numerical model is used to calculate a steady air saturation for a given air injection flow rate. The hydraulic permeability and porosity of the soil are reported by the authors, however, parameters of capillary pressure and relative permeability curves are calibrated from the reported values of total volume of air channels for a given air flow rate. For example, in the case of coarse sand, at the air flow rate of 5.0 L/min, reported total volume of the air channels was 0.089 L. The VG model is utilized for these functions, and adopted parameters are shown in Table 5.4.

Table 5.4: Soil parameters used for calculation of air-water mass transfer coefficients.

Parameter	Value
Hydraulic permeability	$5.49 \cdot 10^{-4}$ [m/s]
Porosity	0.41 [-]
Residual water content	0.06 [-]
α_{aw} parameter in the VG model	10.0 [1/m]
n parameter in the VG model	1.2 [-]
Soil column length	0.305 [m]
Air channel diameter	0.01 [m]
Air channel tortuosity	0.9 [-]
Organic carbon content (f_{oc})	0.3 [%]

Assuming the average value of the air channel diameter from the reported values in the literature, the air-water interface area is calculated from equation (5.50) and transfer coefficient from the equation (5.49). Figure 5.17 shows comparison between calculated and measured values of lumped mass transfer coefficients as a function of air Darcy-velocities for several VOCs. Considering complexity of the process and a number of approximations adopted, a good overall agreement is achieved. Sensitivity analysis showed that air channel diameter has the greatest influence on obtained results. In the experimental work of Elder and Benson [1999], reported air channel diameters for several types of the soil were between 1mm and 11.5mm. In the absence of more reliable information, it can be recommended to use a higher values, in which case the error is conservative.

5.3.4 Simulation of a two-dimensional air sparging experiment

Presented model is verified by application on 2D air-sparging experiments reported by Reddy and Tekola [2004]. Their 2D apparatus consisted of 111cm x 72cm x 10cm Plexiglas tank which was divided into three compartments. The middle compartment was soil chamber, 91cm in length. Two other compartments, each measuring 10 cm in length, were placed on two sides of the middle one, representing reservoirs with fixed water level (Figure 5.18). By changing the water level in the reservoirs, natural groundwater flow can be simulated in the

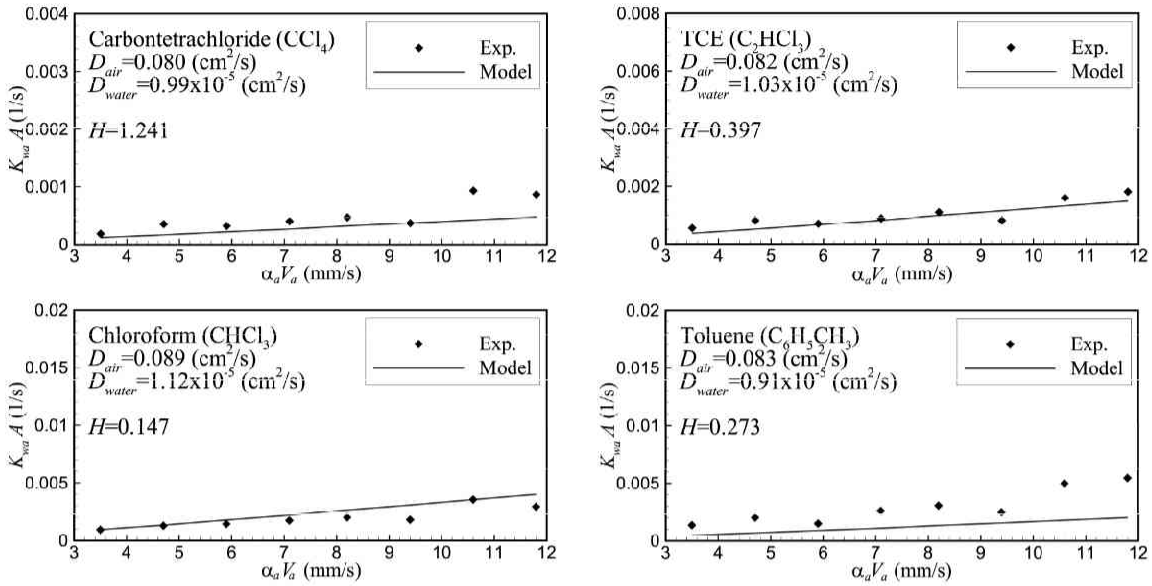

Figure 5.17: Comparison of calculated (lines) and measured (dots) values of lumped air-water mass transfer coefficients.

soil chamber.

Uniform coarse sand with hydraulic permeability of 0.05 cm/s and porosity 0.4 was used. As VOC contaminant, trichloroethylene (TCE) solution was prepared and injected into the soil profile prior the air sparging. During the air sparging course, a TCE concentration was measured in the sampling points (SP) showed in Fig. 5.18.

The numerical grid consists of elements that represent one-inch squares. Constant atmospheric gas pressure is maintained at the top boundary and hydrostatic pressure is imposed at the side walls of the soil chamber. The initial condition for air sparging simulation is obtained by imposing prescribed water level and running the simulation until the equilibrium between gravity and capillary forces is reached. Soil parameters, which are not reported by the authors are assumed as typical for the sand soil (Table 5.5), and calibrated to obtain an agreement of calculated lateral spreading of air phase with reported one. Characteristics of a TCE contaminant are taken the same as in the previous section.

The only calibrated parameter is the mobile-immobile water transfer coefficient (K). This parameter represents diffusion and advection of the contaminants toward the air chan-

nels. Since the representative diffusion length depends on the number of air channels, i.e. the distance between them, the K coefficient must depend on the air saturation. Approximating the K as a inversely proportional to the square of channel distance [Rabideau et al., 1999] and the air channels as uniformly distributed in the horizontal plane of calculation cell, it can be easily shown that K is proportional to the air phase content. Therefore, here is proposed following dependence for the coefficient K:

$$K = K_0 \left(1 + \frac{\alpha_a}{\alpha_{a0}}\right) \tag{5.53}$$

where K_0 is a mass transfer coefficient, calibrated at the referent air phase content (α_{a0}) for specific soil.

(1) Simulation in static groundwater conditions

Firstly, model is applied to the case of static groundwater condition. Figure 5.18 shows SP initial concentrations [Reddy and Tekola, 2004]. In this study, an air injection rate of 7.125 L/min is simulated, for which the steady air saturation distribution is shown in Figure 5.19. Calibrated value of mobile-immobile transfer coefficient is estimated as $K_0 - 2.1x10-4$ 1/s at the air phase content of $\alpha_0 - 0.11$.

Comparison of simulated and measured TCE concentrations at SP 's12' and 's13' is shown in Figure 5.20. As it can be seen from the Figure 5.20-b), the agreement of simulated concentrations at the point 's13' is very good. At the SP 's12', however, there is some discrepancy, but overall agreement is still very well. There are two possible reasons for this discrepancy: (1) values of initial concentrations between sampling points are linearly interpolated, which probably was not the real case; (2) initial concentrations between sampling points and the free surface is unknown and it is possible that density driven flow occurred, which caused almost constant concentration in the period between 20 and 100 min. after start of air injection.

As a comparison, the same scenario is simulated with instant equilibrium assumption between air and the water phase ("Eq. model"). Results for the SP 's12' are showed in Fig. 5.20-a). At the SP 's13' the mass removal is even faster, because of higher air saturation at this point. The assumption of equilibrium partitioning produced a significant overestimate of contaminant removal, and therefore, it is inapplicable for simulation of AS systems.

Table 5.5: Soil parameters used for simulation.

Parameter	Value
Residual water content	0.06 [-]
α_{aw} parameter in the VG model	9.0 [1/m]
n parameter in the VG model	3.2 [1/m]
Air channel diameter	0.01 [m]
Air channel tortuosity	0.9 [-]
Longitudinal dispersivity	0.01 [m]
Longitudinal dispersivity	0.001 [m]
Organic carbon content (f_{oc})	0.1 [%]

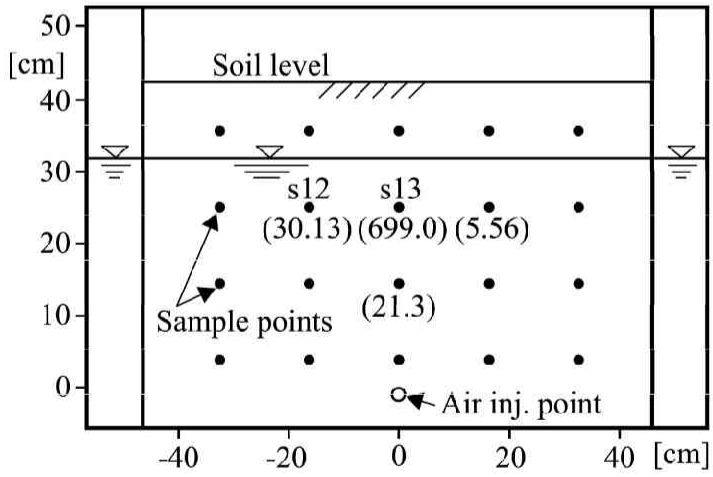

Figure 5.18: Laboratory setup for air sparging simulation. Values in brackets represent initial TCE concentrations (mg/L) for air sparging simulation (Reddy and Tekola, 2004)

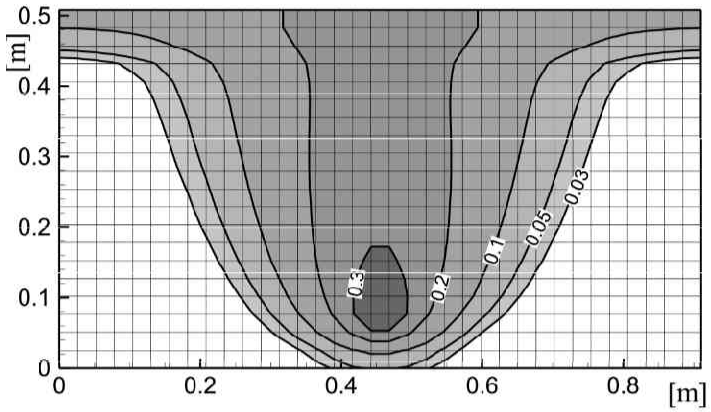

Figure 5.19: Calculated steady-state air saturation contours for no groundwater flow conditions

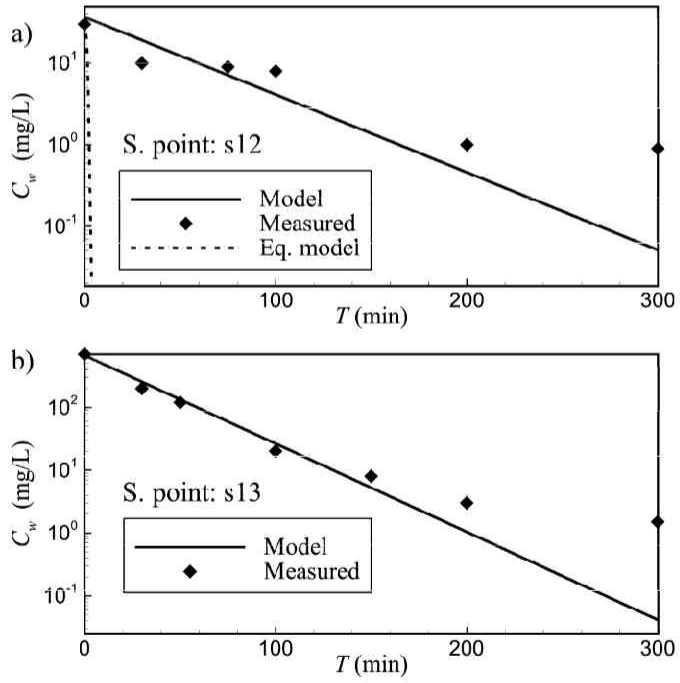

Figure 5.20: Comparison of calculated and measured TCE transient concentrations in water: a) Sampling point 's12', b) Sampling point 's13'.

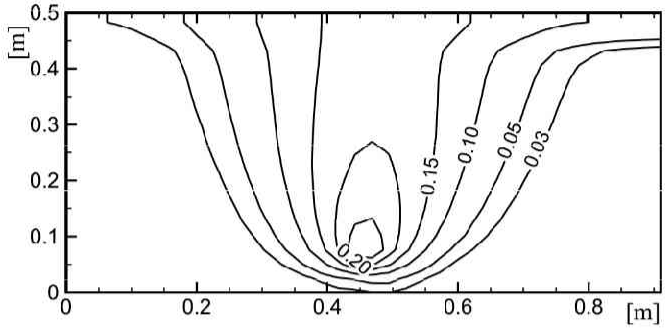

Figure 5.21: Calculated steady-state air saturation contours for groundwater flow conditions

(2) Simulation in groundwater flow conditions

As an illustration of the groundwater flow effect on air sparging performance, two simulations are conducted with different air injection flow rates. Initial conditions, as well as computational parameters are the same as the previous case with stagnant groundwater. The only difference is the 0.03 hydraulic gradient, imposed by rising the water level of the left reservoir. Two air injection flow rates are simulated: 1.5 L/min and 4.0 L/min. Air saturation contours for the case of 4.0 L/min air flow rate is shown in Fig. 5.21. It can be observed that water flow slightly affects air distribution, so it is not symmetric. Concentration distribution, 2.5 hours after start of air sparging, is shown in Fig. 5.22. It can be seen that some amount of contamination "escapes" the zone of influence of the sparging well. At the air flow rate of 1.5 L/min the observed concentrations are about 70% higher than in the case of 4.0 L/min air flow rate. Clearly, natural ground water flow has to be considered in the air sparging simulations.

In another paper, Reddy and Adams [2000] have reported air sparging experiments in the groundwater flow conditions. In the same laboratory setup as described above, benzene-contaminated uniform sand ($K = 4.64 \cdot 10^{-4}$ m/s) was subjected to groundwater hydraulic gradient and two air injection flow rates (2.5 L/min and 4.75 L/min). For both experiments, hydraulic gradient of 0.011 was applied by increasing the water level in the left reservoir.

These experiments are utilized in this study in order to investigate applicability of proposed model for simulation of air sparging in groundwater flow conditions. The first

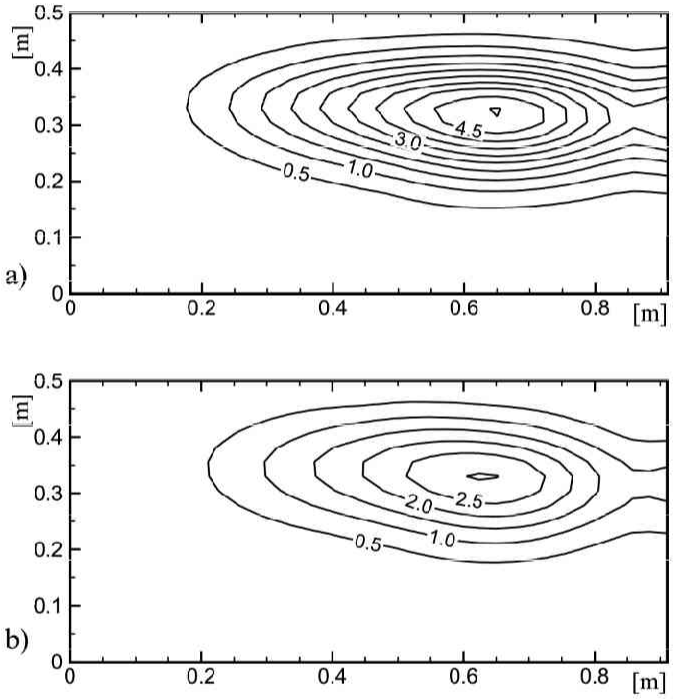

Figure 5.22: Comparison of calculated TCE concentrations (mg/L), 2.5h after start of air injection in groundwater flow conditions: a) 1.5 L/min air flow rate, b) 4.0 L/min air flow rate.

Table 5.6: Soil parameters used for simulation of benzene removal in groundwater flow conditions.

Parameter	Value
Hydraulic permeability	$4.64 \cdot 10^{-4}$ [m/s]
Porosity	0.40 [-]
Residual water content	0.06 [-]
α_{aw} parameter in the VG model	6.0 [1/m]
n parameter in the VG model	2.7 [-]
Air channel diameter	0.01 [m]
Air channel tortuosity	0.9 [-]
Longitudinal dispersivity	0.01 [m]
Transverse dispersivity	0.001 [m]
Organic carbon content (f_{oc})	0.7 [%]

experiment (2.5 L/min air flow rate) is used for calibration of the mass transfer coefficient between mobile and immobile water compartments, while the second experiment (4.75 L/min air flow rate) is utilized for model validation. Characteristic parameters, used in simulations, are shown in Table 5.6.

Figure 5.23 shows initial benzene concentrations for lower air injection experiment. Contaminant plume is concentrated in the center region with initial dissolved benzene concentrations up to 193 mg/L. For numerical simulation, values between sampling points are linearly interpolated. Comparison of measured and simulated transient contaminant concentrations is shown in Fig. 5.24. Calibrated value of the mobile-immobile mass transfer coefficient is $K_0 = 8.1 \cdot 10^{-5}$ 1/s at the air phase content of $\alpha_0 = 0.04$. Figure 5.24-a) shows comparison of measured and simulated initial benzene mass remaining in the soil, as well as the mass of the benzene volatilized into the air plume. It is worthwhile to note that sum of these two curves is not 100% soon after start of air injection, meaning that some amount of benzene is transported downstream by groundwater.

Initial concentrations for increase air flow rate experiment ($q_{air} = 4.75$ L/min) is shown in Fig. 5.25. In the numerical simulation, increased air flow rate only slightly increased sparging zone of influence, while the air saturations are increased. This is in agreement with

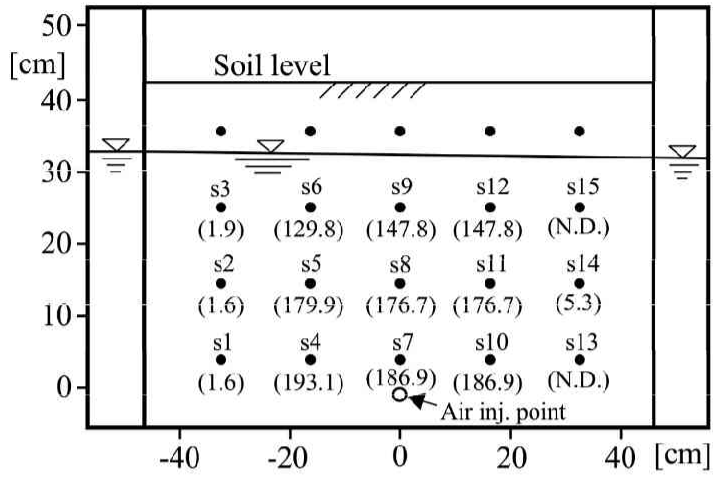

Figure 5.23: Initial benzene concentrations (mg/L) for air sparging simulation in groundwater flow conditions (q_{air} = 2.5 L/min) (Reddy and Adams, 2000).

visually observed experimental air plume. All parameters of the model are kept as same as in the previous case.

Comparison of measured and simulated results for increased air flow rate are shown in Fig. 5.26. It can be seen that overall model results are in very well agreement with measured ones. Comparison of measured and simulated initial benzene mass removal and benzene mass volatilization is shown in Fig. 5.26-a). By comparison with lower air injection rate (5.24-a) it can be seen that higher air flow rate did not accelerate overall benzene removal from the soil. However, the amount of volatilized benzene has been increased (from about 68% to nearly 80%). This implies that increased air flow has as a consequence higher air saturations, and in turn, reduced hydraulic permeability, due to which the amount of benzene transported downstream has been decreased. Nevertheless, in in-situ application, one has to be carefull with increase of air flow rate, which can eventually cause the contaminat plume to circumvent the zone of aeration due to significant reduction of hydraulic permeability.

Application of obtained mobile-immobile mass transfer coefficient for the conditions with groundwater flow to experiment without hydraulic gradient could not reproduce well observed benzene removal. It can be concluded that natural groundwater flow significantly affects diffusive transport of contaminants toward the air channels. This, however, is to be expected, due to increased advective/dispersive transport processes. This also means that

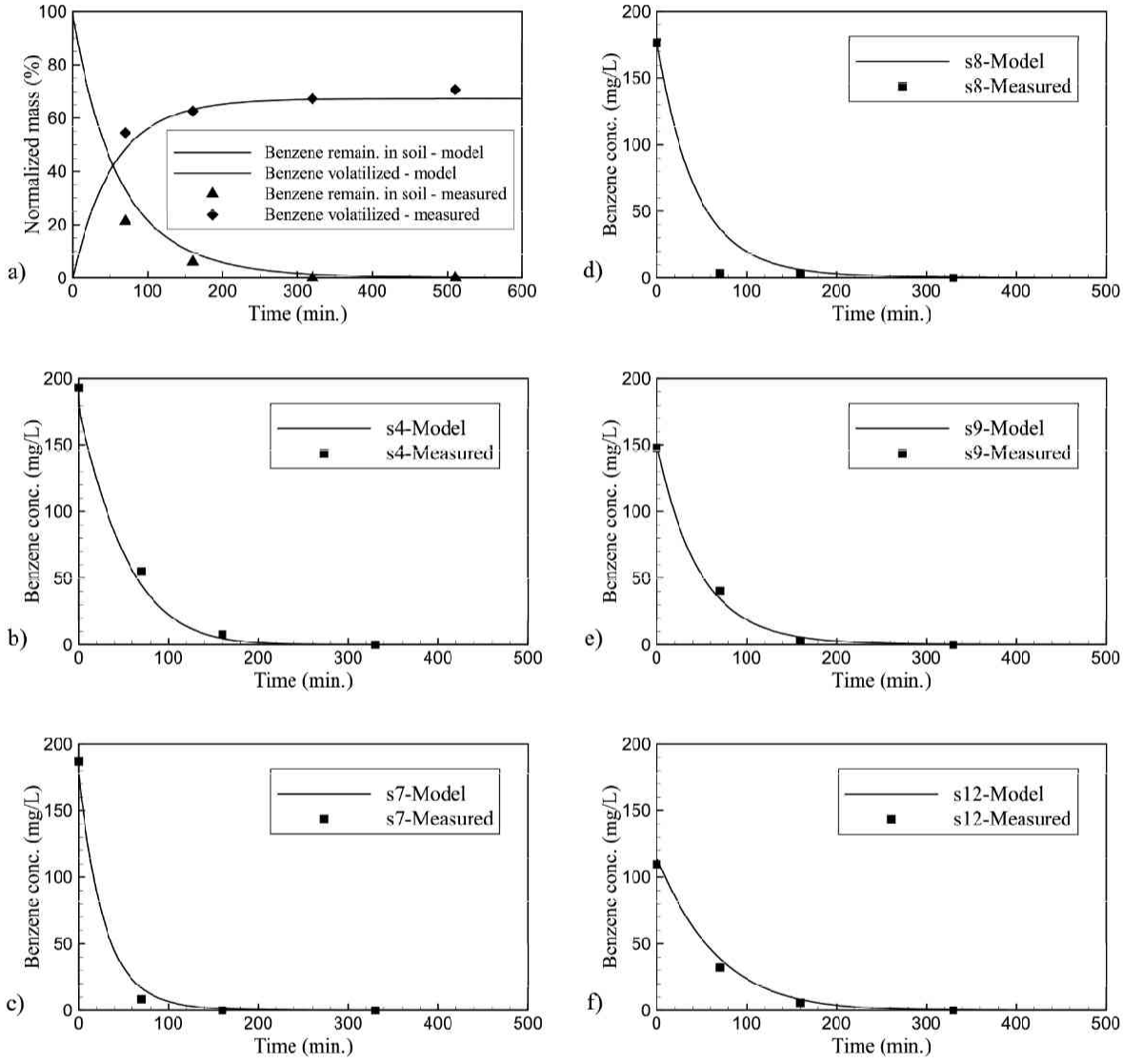

Figure 5.24: Comparison of measured and simulated benzene concentrations (q_{air} = 2.5 L/min): a) initial benzene mass remaining in the soil and mass volatilized, b) sampling point s4, c) sampling point s7, d) sampling point s8, e) sampling point s9, f) sampling point s12.

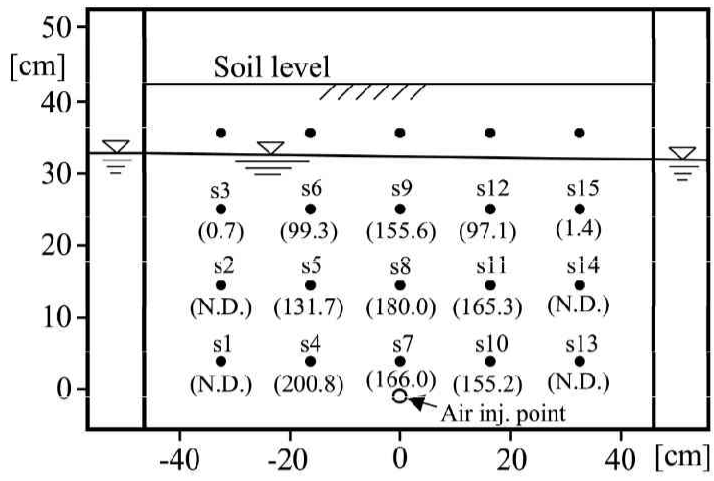

Figure 5.25: Initial benzene concentrations (mg/L) for air sparging simulation in groundwater flow conditions ($q_{air} = 4.75$ L/min) (Reddy and Adams, 2000).

laboratory transport parameters estimated in laboratory conditions with stagnant water are inapplicable for sites with natural hydraulic gradients. Further experimental and numerical investigations are required in order to characterize this dependence.

5.4 Summary

In this chapter, developed multiphase model is applied for simulation of air sparging. Two related topics are covered: (1) modeling of air flow and distribution in saturated/unsaturated soils, and (2) modeling of contaminant transport. In the former case presented model extends the traditional multiphase theory by inclusion of acceleration terms in governing equations, with intention to expand the applicability of the model to porous media with higher hydraulic permeability, such as medium to coarse sands or gravels. Accuracy of the presented model is verified on the benchmark test problem, earlier in the thesis, where it showed excellent agreement with analytical solution.

The simulation of two-dimensional laboratory experiments for homogeneous porous media is used to investigate the role of acceleration terms in governing equations. Two experiments are simulated. In the case of 0.75mm glass beads, the effect of acceleration terms on dynamically trapped air volume is found to be negligible. However, in the case of 4mm

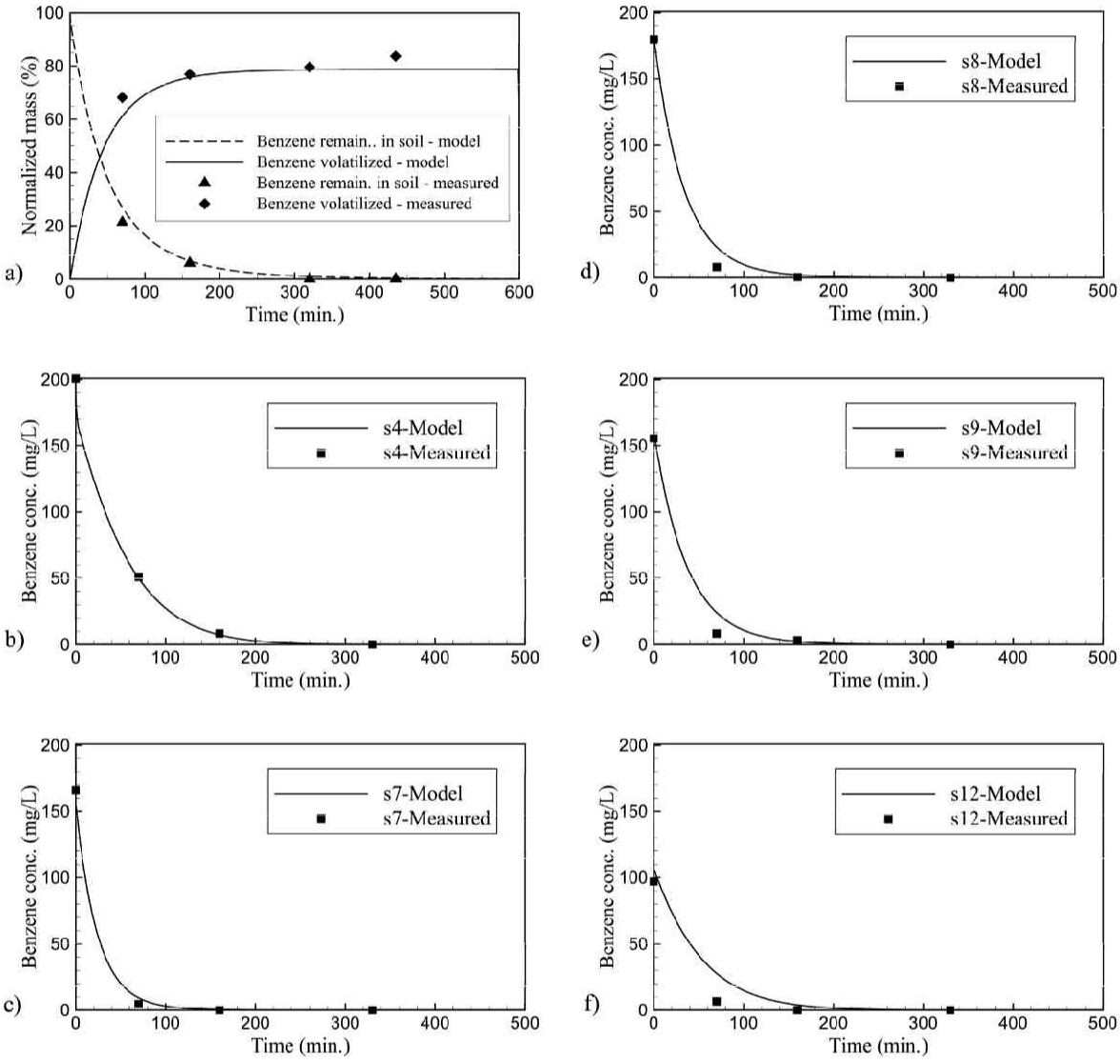

Figure 5.26: Comparison of measured and simulated benzene concentrations (q_{air} = 4.75 L/min): a) initial benzene mass remaining in the soil and mass volatilized, b) sampling point s4, c) sampling point s7, d) sampling point s8, e) sampling point s9, f) sampling point s12.

glass beads, the effect is significant with difference exceeding 20% in total air volume for simulated air flow rates. Knowing that the dynamically trapped air volume is in direct relation with efficiency of air sparging, these results have significant practical consequences. It can also be noted that acceleration effects coincide with a change of air flow pattern. Comparison of simulated and observed air distributions are encouraging and indicate that presented model can be used for simulation of both air flow patterns recognized in the literature: the channel and bubble air flow pattern. In addition, the instability, observed at experiments as steady pulsation, can be reproduced by presented model. The observed instability is also theoretically analyzed. It is shown that instability can be expected in materials with particle diameter greater than 2 mm. Both used models for capillary pressure function confirmed this conclusion.

A novel, mechanistic model for simulation of mass transfer/transport during air sparging has been proposed. Model combines the multiphase model for prediction of air saturations, and three compartment approach to simulate contaminant transport. Application to reported experiments showed capability of the presented model to simulate observed contaminant removal. It is confirmed that equilibrium assumption is inadequate for air sparging simulations. It is also shown that natural groundwater flow has to be considered during the design of optimal air sparging system.

Chapter 6

Model application: Modeling of bubble plumes

6.1 Preliminaries

Thermal stratification is a common problem in terms of water quality in deep lakes and reservoirs [Shladow, 1992; Wuest *et al.*, 1992; Sahoo and Luketina, 2003]. Generally, it produces three layers: (1) a well mixed top, surface layer, (2) deep hypolimnion layer with relatively uniform temperature and density, and (3) middle metalimnion barrier which prevents mixing between the top and the bottom layer. A metalimnion layer is characterized by strong thermal and density gradients. As a consequence, the concentrations of oxygen in a bottom layer becomes low due to biochemical consumption, and eventually, becomes anoxic.

A restoration technology, often used as artificial destratification, is injection of compressed air or oxygen into hypolimnion, inducing a buoyancy driven bubble plume which in time attenuates the thermal gradient. The induced plume entrains the ambient, heavy water and carries it toward the surface. At the same time, oxygen from the injected gas is dissolved in the water. There are two reported strategies for lake restoration [Wuest *et al.*, 1992]: (1) mixing of the water during the cold season to promote and extend the natural mixing, and (2) injection of oxygen for hypolimnion oxygenation during the hot season in a way to preserve the stratification. These two strategies, obviously, have different goals in terms of mixing. In the former case, the air injection flow rate, and designed bubble size have to provide the

complete mixing, up to the water surface. In the letter case, however, the bubble size has to be minimal in order to provide complete dissolution before reaching the surface. Numerical modeling potentially represents a valuable tool for optimal design of bubble plume strategy.

In this chapter, developed numerical model will be applied for simulation of bubble plumes. Problem requires several model refinements in order to simulate involved processes. Firstly, the assumption of gas/air incompressibility does not hold in the case of deep lakes which greatly affects the numerical procedure described earlier, and secondly, the mass transfer/dissolution of one phase (air/oxygen) to water phase has to be considered, and appropriate change of the continuity equations has to be considered.

6.2 Literature review

Probably the first theoretical analysis of bubble plumes has been reported by Kobus [1968], where he utilized the assumption of Gaussian distribution of water velocity, spreading linearly in vertical direction. His theoretical conclusions were supported by experimental investigations of round bubble plumes in a laboratory basin, 8 m wide and 4.7 m high. He also found as necessary to average experimental data over five-minute intervals, due to significant fluctuations. These fluctuations were caused by turbulence, but also by lateral wandering of the plume [Milgram, 1983].

Ditmars and Cardewall [1974] developed and integral theory of bubble plumes, based on horizontal integration of conservation equations for mass, momentum and buoyancy. The main hypothesis in this, and later developed similar theories, is that entrainment of ambient water is proportional to the centerline velocity of the plume and to the plume circumference.

Milgram [1983] extended the same theory by inclusion of turbulent transport, defining the momentum amplification factor as the ratio of total momentum flux to the momentum flux of the mean flow. The same, a horizontal integration of conservation equations, approach was utilized by McDougall [1978] to consider bubble plumes in stratified ambient water. He introduced a double-plume model, consisting of inner circular plume, and outer annular plume. As also shown in experiments, in stratified environment there is an eventual terminal height to which the buoyant plume will rise. Due to neutral buoyancy, at some point, the water phase is detrained, while the gas phase starts to build a new plume. This

phenomena may be repeated, before reaching the water surface [McDougall, 1978; Asaeda and Imberger, 1989]. The model proposed by McDougall, is utilized by Schladow [1992] to analyze dynamics of cascade plumes, and its effects on mixing efficiency.

The same model formulation, with some improvements, has been used by many authors for simulation of lake restoration. Wuest *et al.* [1992], for example, included exchange of gases (oxygen and nitrogen) between bubbles and water, and conservation of dissolved gases in the water phase. They assumed an uniform distribution of plume water velocity, temperature and dissolved gases in horizontal plane. Similar model, but with Gaussian distribution of these variables is proposed by Sahoo and Luketina [2003].

Although this approach provided a valuable insight of governing mechanisms in bubble plumes, some phenomena can not be simulated with these models, such as effects of moving air source on water restoration, or simulation of multiple injection points with overlapping zones of influence. For simulation of these effects, a multidimensional approach is required.

Multidimensional, mechanistic models for simulation of bubble plumes are successfully utilized for simulation of flows in bubble column and loop reactors, used in chemical engineering [Durst *et al.*, 1984; Becker *et al.*, 1994; Sokolichin and Eigenberger, 1994; Sokolichin and Eigenberger, 1999; Borchers *et al.*, 1999]. A comprehensive review of these models is given by Sokolichin *et al.* [2004]. As they concluded, the main open question in modeling of bubble plumes is proper treatment of turbulence. The importance of this issue is emphasized by Sokolichin and Eigenberger [1999], where they showed that only a full 3D turbulent model produced a good agreement with measurements of bubble plume in a experimental water tank with dimensions 50cm x 150cm x 8cm.

6.3 Refinements of the numerical model

6.3.1 Refinement of the HSMAC iterative procedure

Assuming the gas (air/oxygen) phase as compressible, and considering the mass transfer between the gas and water phase, continuity equations (2.49) can be rewritten as:

$$\frac{\partial\left(\rho_a \alpha_a\right)}{\partial t} + \frac{\partial\left(\rho_a \alpha_a V_{ai}\right)}{\partial x_i} = -G_{aw} \tag{6.1}$$

$$\frac{\partial \alpha_w}{\partial t} + \frac{\partial \left(\alpha_w V_{wi}\right)}{\partial x_i} = \frac{G_{aw}}{\rho_w} \tag{6.2}$$

$$\alpha_a + \alpha_w = 1 \tag{6.3}$$

where G_{aw} represents a mass transfer between the gas and liquid, per unit time. Subscripts a and w denote the gas and the water phase, respectively.

It can be assumed that density of the gas phase comply to ideal gas law:

$$\rho_a = \frac{p_a m_a}{RT} \tag{6.4}$$

where p_a is the gas pressure, m_a is the gas molar mass, T is the absolute temperature, and R is the gas constant ($= 0.08206\, L\, atm\, K^{-1} mol^{-1}$).

Summation of equations (6.1) and (6.2), with minor manipulation, gives the following expression equivalent to divergence, defined in Chapter 3. of this thesis:

$$\frac{\partial \left(\alpha_a V_{ai}\right)}{\partial x_i} + \frac{\partial \left(\alpha_w V_{wi}\right)}{\partial x_i} + \frac{\alpha_a}{\rho_a}\left(\frac{\partial \rho_a}{\partial t} + V_{ai}\frac{\partial \rho_a}{\partial x_i}\right) + G_{aw}\left(\frac{1}{\rho_a} - \frac{1}{\rho_w}\right) = D = 0 \tag{6.5}$$

where the third term is introduced due to compressibility of the gas phase, and the fourth term due to mass transfer.

Recalling the pressure correction equation in the HSMAC iterative procedure:

$$p_a^{n+1,r+1} = p_a^{n+1,r} - \omega \frac{D^{r+1}}{\left(\frac{\partial D^{r+1}}{\partial p_a^{n-1}}\right)}, \tag{6.6}$$

the divergence derivative has to be obtained as:

$$\frac{\partial D}{\partial p_a^{n+1}} = \underbrace{\frac{\partial}{\partial p_a^{n+1}}\left[\frac{\partial \left(\alpha_a V_{ai}\right)}{\partial x_i} + \frac{\partial \left(\alpha_w V_{wi}\right)}{\partial x_i}\right]}_{(I)} + \overbrace{\frac{\partial}{\partial p_a^{n+1}}\left\{\frac{\alpha_a}{\rho_a}\frac{m_a}{RT}\left[\frac{\partial p_a}{\partial t} + V_{ai}\frac{\partial \rho_a}{\partial x_i}\right]\right\}}^{(II)}$$

$$+ \underbrace{\frac{\partial}{\partial p_a^{n+1}}\left[G_{aw}\left(\frac{1}{\rho_a} - \frac{1}{\rho_w}\right)\right]}_{(III)} \tag{6.7}$$

where the first term on the right side is the same as in the incompressible case. Two additional terms, for convenience here denoted by (II) and (III), can be expressed as follows:

$$(II) = \left(\frac{1}{\rho_a}\frac{m_a}{RT}\right)^2\left[\alpha_a\frac{\partial p_a}{\partial t} + \alpha_a V_{ai}\frac{\partial p_a}{\partial x_i}\right] + \frac{1}{\rho_a}\frac{m_a}{RT}\left[\frac{\alpha_a}{\Delta t} + \frac{\partial \left(\alpha_a V_{ai}\right)}{\partial p_a^{n+1}}\frac{\partial p_a}{\partial x_i}\right] \tag{6.8}$$

$$(III) = \frac{\partial G_{aw}}{\partial p_a^{n+1}}\left(\frac{1}{\rho_a} - \frac{1}{\rho_w}\right) + \frac{G_{aw}}{\rho_a^2}\frac{m_a}{RT} \tag{6.9}$$

The term $\frac{\partial(\alpha_a V_{ai})}{\partial p_a^{n+1}}$ in equation (6.8) can be expressed as in the incompressible case, and the term $\frac{\partial G_{aw}}{\partial p_a^{n+1}}$ in equation (6.9) depends on modeling formulation of the mass transfer process. Usually, it is a first-order kinetic formulation:

$$G_{aw} = K_{aw} A \left(K_H p_a \quad C_w \right) \tag{6.10}$$

where K_{aw} is the mass transfer coefficient (function of bubble size), A is the air-water surface area, K_H is the dimensional Henry's constant, and C_w is the gas concentration in the water phase. Therefore:

$$\frac{\partial G_{aw}}{\partial p_a^{n+1}} = K_{aw} A K_H \tag{6.11}$$

In the discretized form, the divergence derivative is now:

$$\begin{aligned}
\left(\frac{\partial D^{r+1}}{\partial p_a^{n+1}} \right) = \Delta t \Bigg[& \frac{\left(\frac{\alpha_a}{M_a}\right)_{i-\frac{1}{2}} + \left(\frac{\alpha_a}{M_a}\right)_{i+\frac{1}{2}}}{(\Delta x_1)^2} + \frac{\left(\frac{\alpha_a}{M_a}\right)_{j-\frac{1}{2}} + \left(\frac{\alpha_a}{M_a}\right)_{j+\frac{1}{2}}}{(\Delta x_2)^2} \\
& + \frac{\left(\frac{\alpha_a}{M_a}\right)_{k-\frac{1}{2}} + \left(\frac{\alpha_a}{M_a}\right)_{k+\frac{1}{2}}}{(\Delta x_3)^2} \Bigg] + \Delta t \Bigg[\frac{\left(\frac{\alpha_w}{M_w}\right)_{i-\frac{1}{2}} + \left(\frac{\alpha_w}{M_w}\right)_{i+\frac{1}{2}}}{(\Delta x_1)^2} \\
& + \frac{\left(\frac{\alpha_w}{M_w}\right)_{j-\frac{1}{2}} + \left(\frac{\alpha_w}{M_w}\right)_{j+\frac{1}{2}}}{(\Delta x_2)^2} + \frac{\left(\frac{\alpha_w}{M_w}\right)_{k-\frac{1}{2}} + \left(\frac{\alpha_w}{M_w}\right)_{k+\frac{1}{2}}}{(\Delta x_3)^2} \Bigg] \frac{\rho_a}{\rho_w} + \\
& \left(\frac{1}{\rho_a} \frac{m_a}{RT} \right)^2 \left[\alpha_a \frac{p_a^{n+1} - p_a^n}{\Delta t} + \alpha_a V_{a1} \frac{\widetilde{\partial p_a}}{\partial x_1} + \alpha_a V_{a2} \frac{\widetilde{\partial p_a}}{\partial x_2} + \alpha_a V_{a3} \frac{\widetilde{\partial p_a}}{\partial x_3} \right] + \\
& \frac{1}{\rho_a} \frac{m_a}{RT} \left\{ \frac{\alpha_a}{\Delta t} + 0.5 \cdot \left[\frac{\left(\frac{\alpha_w}{M_w}\right)_{i+\frac{1}{2}}}{\Delta x_1} - \frac{\left(\frac{\alpha_w}{M_w}\right)_{i-\frac{1}{2}}}{\Delta x_1} \right] \frac{\widetilde{\partial p_a}}{\partial x_1} + \right. \\
0.5 \cdot & \left[\frac{\left(\frac{\alpha_w}{M_w}\right)_{j+\frac{1}{2}}}{\Delta x_2} \quad \frac{\left(\frac{\alpha_w}{M_w}\right)_{j-\frac{1}{2}}}{\Delta x_2} \right] \frac{\widetilde{\partial p_a}}{\partial x_2} + 0.5 \cdot \left. \left[\frac{\left(\frac{\alpha_w}{M_w}\right)_{k+\frac{1}{2}}}{\Delta x_3} \quad \frac{\left(\frac{\alpha_w}{M_w}\right)_{k-\frac{1}{2}}}{\Delta x_3} \right] \frac{\widetilde{\partial p_a}}{\partial x_3} \right\} + \\
& K_{aw} A K_H \left(\frac{1}{\rho_a} - \frac{1}{\rho_w} \right) + \frac{G_{aw}}{\rho_a^2} \frac{m_a}{RT}
\end{aligned} \tag{6.12}$$

where M_a and M_w are defined as same as in the incompressible case:

$$M_a = 1 + \Delta t C_a \quad M_w = 1 + \Delta t C_w \tag{6.13}$$

These expressions for M_a and M_w are slightly different in comparison with equations in Chapter 3. (the factor 0.5 is omitted), since in the case of bubble flow the resistance force

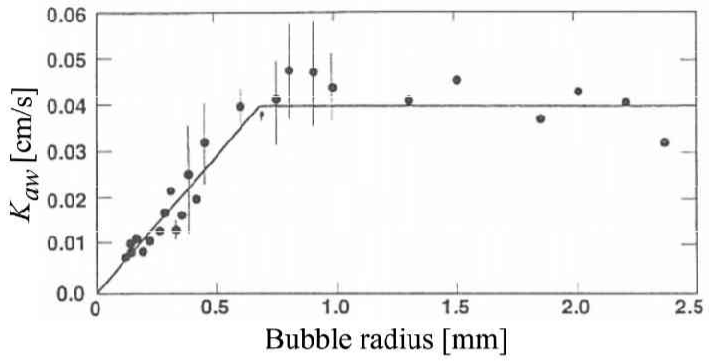

Figure 6.1: Mass transfer coefficient for oxygen measured in tap water as a function of bubble radius. Dots represent measured values, and line represents approximation used by [Wuest *et al.*, 1992]

has several components which are not constants. This will be clarified in the next section, in which refinement of the momentum equations will be discussed.

Pressure space derivatives in equation (6.12)can be approximated as:

$$\widetilde{\frac{\partial p_a}{\partial x_i}} \approx \frac{(p_a^{n+1})_{i+1} - (p_a^{n-1})_{i-1}}{x_{i+1} - x_{i-1}} \tag{6.14}$$

Calculation of mass transfer is introduced in each iteration and therefore, when D^{r+1} satisfy given criteria, the value of mass transfer at each time step is already obtained.

As stated earlier, the K_{aw} parameter in a mass transfer calculation (Eq. 6.10) is a function of bubble diameter, as shown in Figure 6.1 [Wuest *et al.*, 1992] for oxygen in a tap water. Figure also shows linear approximation used by authors. It can be seen that for bubble diameter larger than ≈1.4 mm, this coefficient is nearly constant (0.04 cm/s).

Henry's constant for oxygen can also be found in chemical literature. In this study, a temperature functional is utilized in a form [Wuest *et al.*, 1992]:

$$K_H(T) = K_{H0} + K_{H1} \cdot T + K_{H2} \cdot T^2 \tag{6.15}$$

where $K_{H0} = 2.125\, mol\, bar^{-1}\, m^{-3}$, $K_{H1} = -0.05021\, mol\, bar^{-1}\, m^{-3}\, {}^{\circ}C^{-1}$, and $K_{H2} = 5.77 \cdot 10^{-4}\, mol\, bar^{-1}\, m^{-3}\, {}^{\circ}C^{-2}$.

In order to allow the change of bubble diameter, due to density change and loss of mass by dissolution, a number of bubbles is tracked by solution of following advection

equation:

$$\frac{\partial N_b}{\partial t} + \frac{\partial \left(V_{ai} N_b\right)}{\partial x_i} = 0 \tag{6.16}$$

where N_b is the number of bubbles in calculation cell. It is essential here to avoid numerical dispersion as much as possible, and therefore, the higher order approach with TVD limiter is utilized as described in Chapter 3. of this thesis. From calculated gas content and advected number of bubbles, the bubble diameter is given by:

$$d_b = \sqrt[3]{\frac{\alpha_a \Delta x_1 \, \Delta x_2 \, \Delta x_3}{N_b} \frac{6}{\pi}} \tag{6.17}$$

Coalescence and bubble break-up are neglected in presented model.

6.3.2 Formulation of momentum equations

Application of momentum equation (2.50) on bubble plume flow gives for the gas and the water phase as follows:

$$\frac{\partial \left(\rho_a \alpha_a V_{ai}\right)}{\partial t} + \frac{\partial \left(\rho_a \alpha_a V_{ai} V_{aj}\right)}{\partial x_j} = -\alpha_a \frac{\partial p_a}{\partial x_i} - \rho_a \alpha_a g \frac{\partial x_3}{\partial x_i} - F_{aw} \tag{6.18}$$

$$\frac{\partial \left(\alpha_w V_{wi}\right)}{\partial t} + \frac{\partial \left(\alpha_w V_{wi} V_{wj}\right)}{\partial x_j} = -\frac{\alpha_w}{\rho_w} \frac{\partial p_w}{\partial x_i} - \alpha_w g \frac{\partial x_3}{\partial x_i} + \frac{1}{\rho_w} \frac{\partial (\alpha_w \tau_{ij}^w)}{\partial x_j} + \frac{1}{\rho_w} F_{aw} \tag{6.19}$$

where τ_{ij}^w, in general case, may include viscous and turbulent stresses.

The only difference in above two equations is in sign of the momentum interaction term F_{aw}. This term comprises interaction of bubbles and water, due to local variation of pressure and shear stress at the air/water interface. The resulting force can not be resolved at this (micro) scale for a general case, but averaged effects can be estimated from empirical correlations. In the literature, this term is usually divided into three components: drag force, added mass force and lift force:

$$F_{aw} = F_d + F_{adm} + F_l \tag{6.20}$$

The drag force represents a resistance to the bubble due to presence of the water phase. Both, the pressure and the shear stresses, contribute to the drag force and usually, it is expressed as a function of relative bubble velocity in respect to the water:

$$F_d = \frac{1}{2} C_d \rho_w \pi \frac{d_b^2}{4} \left|V_a - V_w\right| \left(V_a - V_w\right) \tag{6.21}$$

where C_d is the nondimensional drag coefficient. There are several empirical expressions for this coefficient utilized in the literature [Sokolichin *et al.*, 2004]:

$$C_d = \begin{cases} \frac{24}{Re}\left(1 + 0.15Re^{0.687}\right) & \text{if} \quad Re < 1000 \\ 0.44 & \text{if} \quad Re \geq 1000 \end{cases} \tag{6.22}$$

$$C_d = max\left[\frac{24}{Re}\left(1 + 0.15Re^{0.687}\right), \frac{8}{3}, \frac{Eo}{Eo+4}\right] \tag{6.23}$$

$$C_d = \frac{0.622}{\frac{1}{Eo} + 0.235} \tag{6.24}$$

$$C_d = \begin{cases} 24/Re, & \text{if} \quad Re < 0.49 \\ 20.68/Re^{0.643}, & \text{if} \quad 0.49 < Re < 100 \\ 6.3/Re^{0.385}, & \text{if} \quad Re > 100,\ We < 8 \quad \text{and} \quad Re < 2065.1/We^{2.6} \\ We/3, & \text{if} \quad Re > 100,\ We \leq 8 \quad \text{and} \quad Re > 2065.1/We^{2.6} \\ 8/3, & \text{if} \quad Re > 100,\ We > 8 \end{cases} \tag{6.25}$$

$$C_d = \frac{2}{3}\sqrt{Eo} \tag{6.26}$$

where nondimensional Eotwos and Weber numbers are defined as $Eo = \frac{g\rho_w d_b^2}{\sigma}$ and $We = \frac{\rho_l |V_a - V_w|^2 d_b}{\sigma}$.

Sokolichin *et al.* analyzed these relations for the case of stagnant water and found that correlation (6.21) significantly overestimates the terminal velocity of the bubbles larger than 3 mm in diameter, while other expressions produce similar results.

When bubbles accelerate in respect to the water, there is additional force required to accelerate the ambient water around the bubbles. This force is called an added mass force, and it can be estimated by following relation [Drew and Lahey, 1987]:

$$F_{adm} = C_v \rho_w \alpha_a \left(\frac{\mathcal{D}V_a}{\mathcal{D}t} - \frac{\mathcal{D}V_w}{\mathcal{D}t}\right) \tag{6.27}$$

where C_v is the parameter (0.5), and $\mathcal{D}/\mathcal{D}t$ is the material derivative. For the sake of simplicity, in presented numerical model evaluation of this term was conducted under incompressibility assumption. This way, the equation (6.27) can be expressed in term of fluxes (e.g. $\alpha_a V_a$) instead of velocities, which is more convenient for programming:

$$\frac{\mathcal{D}V_a}{\mathcal{D}t} - \frac{\mathcal{D}V_w}{\mathcal{D}t} = \frac{1}{\alpha_a}\left[\frac{\partial\left(\alpha_a V_a\right)}{\partial t} + \nabla \cdot \left(\alpha_a V_a^2\right)\right] - \frac{1}{\alpha_w}\left[\frac{\partial\left(\alpha_w V_w\right)}{\partial t} + \nabla \cdot \left(\alpha_w V_w^2\right)\right] \tag{6.28}$$

Knowing that the drag force is the dominant force, it is reasonable to assume that this approximation does not influence the resulting force significantly.

The lift force is directed perpendicular to the main flow direction, and is the consequence of bubble rotation (Magnus force) and asymmetrical pressure distribution around the bubble. It can be described as [Drew and Lahey, 1987]:

$$F_l = C_v \rho_w \alpha_a \left(V_a - V_w\right) \times \left(\nabla \times V_a\right) \tag{6.29}$$

For example, in the direction x_1, this force is calculated as:

$$F_{l1} = C_v \rho_w \alpha_a \left[\left(V_{a2} - V_{w2}\right)\left(\frac{\partial V_{w2}}{\partial x_1} - \frac{\partial V_{w1}}{\partial x_2}\right) - \left(V_{a3} - V_{w3}\right)\left(\frac{\partial V_{w1}}{\partial x_3} - \frac{\partial V_{w3}}{\partial x_1}\right)\right] \tag{6.30}$$

In the numerical model, the F_{l1} is calculated at each iteration (implicitly), the convective part of F_{adm} is calculated the same as the momentum advection (Adams-Bashforth scheme) and for the drag term an implicity factor pp is introduced, such as:

$$F_d = pp\, F_d^n + (1 - pp) F_d^{n+1} \tag{6.31}$$

Coefficients C_a and C_w in equations (6.13) can now be defined as:

$$C_a = (1 - pp)\frac{\rho_w}{\rho_a}\frac{3}{4}\frac{C_d}{d_b}\left|V_a - V_w\right| + C_v\frac{\rho_w}{\rho_a} \tag{6.32}$$

$$C_w = (1 - pp)\frac{\alpha_a}{\alpha_w}\frac{3}{4}\frac{C_d}{d_b}\left|V_a - V_w\right| + C_v\frac{\alpha_a}{\alpha_w} \tag{6.33}$$

6.3.3 Turbulence model

As pointed out by Sokolichin and Eigenberger [1999], in order to simulate conducted experiments of bubble flow in flat tanks, it is necessary to apply a fully 3D turbulent model. Therefore, here presented model is extended by inclusion of a standard $k-\epsilon$ model of turbulence [e.g. Ferziger, 1987]. The turbulent kinetic energy and dissipation equations, utilized herein, are as follows:

$$\frac{\partial k}{\partial t} + \frac{\partial\left(V_{wj}k\right)}{\partial x_j} = -\overline{V'_{wi}V'_{wj}}\left(\frac{\partial V_{wi}}{\partial x_j} + \frac{\partial V_{wj}}{\partial x_i}\right) - \epsilon + \frac{\partial}{\partial x_i}\frac{\nu_T}{\sigma_k}\frac{\partial k}{\partial x_j} \tag{6.34}$$

$$\frac{\partial \epsilon}{\partial t} + \frac{\partial\left(V_{wj}\epsilon\right)}{\partial x_j} = C_{1\epsilon}\frac{\epsilon}{k}\left(-\overline{V'_{wi}V'_{wj}}\right)\left(\frac{\partial V_{wi}}{\partial x_j} + \frac{\partial V_{wj}}{\partial x_i}\right) - C_{2\epsilon}\frac{\epsilon^2}{k} + \frac{\partial}{\partial x_i}\frac{\nu_T}{\sigma_\epsilon}\frac{\partial k}{\partial x_j} \tag{6.35}$$

where k is the turbulent kinetic energy, ϵ is the dissipation rate and ν_T is the eddy viscosity defined as:

$$\nu_T = C_\mu \frac{k^2}{\epsilon} \tag{6.36}$$

Incorporated constants are taken as: $C_{1\epsilon} = 1.44$, $C_{2\epsilon} = 1.92$, $\sigma_k = 1.0$, $\sigma_\epsilon = 1.3$ and $C_\mu = 0.09$.

Raynold's stress tensor in equations (6.34) and (6.35) is calculated as:

$$-\overline{V'_{wi}V'_{wj}} = \nu_T \left(\frac{\partial V_{wi}}{\partial x_j} + \frac{\partial V_{wj}}{\partial x_i} \right) - \frac{2}{3} k \delta_{ij} \tag{6.37}$$

At this stage, the bubble induced turbulence is not included in the presented model. Since usually bubble plumes imply a small volume fraction of the air phase, this effect is probably not significant in such cases. Since this point is not satisfactorily resolved yet in the literature, model extension requires further experimental and numerical research.

6.4 Simulation of reported laboratory experiments

In this section, the performance of developed model will be validated by comparison of simulation results with reported experimental data. Sokolichin and Eigenberger [1999], and Borchers *et al.* [1999] reported experiments of gas-liquid bubble flow in a flat bubble column with rectangular cross-section. The column was 50cm wide, 200cm high and 8cm deep, in which different water levels were imposed. Air sparger was centered at the tank bottom, through which different air injection flow rates were applied. Bubble plumes were visually observed through transparent column walls, but also a Laser Doppler Anemometer (LDA) was used to measure velocity magnitude of the water in the mid-plane of column depth (4cm from the walls), at regular grid points (10 or 20cm apart).

The same setup was also used by Becker *et al.* [1994] to conduct similar experiments, but with shifted injection point from the bottom center. This experiment will also be simulated herein.

Case 1:

The experiment in which the tank is filled with water up to 50cm is firstly simulated. For numerical simulation, the flow domain is discretized by 25x4x25 cells in, x_1, x_2 and x_3 direction, respectively. The adopted time step is 0.001 sec.

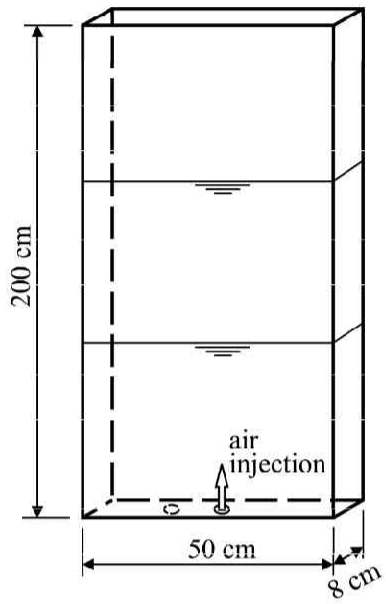

Figure 6.2: Schematic representation of simulated experiments, after Becker *et al.*, [1994]

Depending on the start-up conditions, in this case authors reported formation of a single vortex, near the center of the flow domain, in clockwise or counterclockwise direction. Figure 6.3 shows simulated water phase flow field at different times, in a process of reaching the steady conditions. Figure 6.4 compares observed bubble swarm, and simulated one for steady state. Although the agreement could be considered as very well, slightly larger volume of bubble swarm in the bottom part of the tank is a consequence of space discretization (2cm cubes). Finer discretization would probably produce even better agreement. It can be seen that simulation reproduced actual air distribution very well.

Quantitative comparison of simulated and measured velocities for steady conditions is shown in Figure 6.5. A very good overall agreement of developed flow field can be observed. Flow is characterized by single, almost in center placed vortex, with near-stagnant water in top and bottom right corners.

The same experiment is used to compare results of different numerical schemes utilized for convective acceleration terms in momentum equations for both phases. Figure 6.5 - a) shows results obtained with a MUSCL-TVD scheme described in Chapter 3. of this thesis, and Figure 6.5 - b) shows results with QUICK scheme. Despite quite similar results,

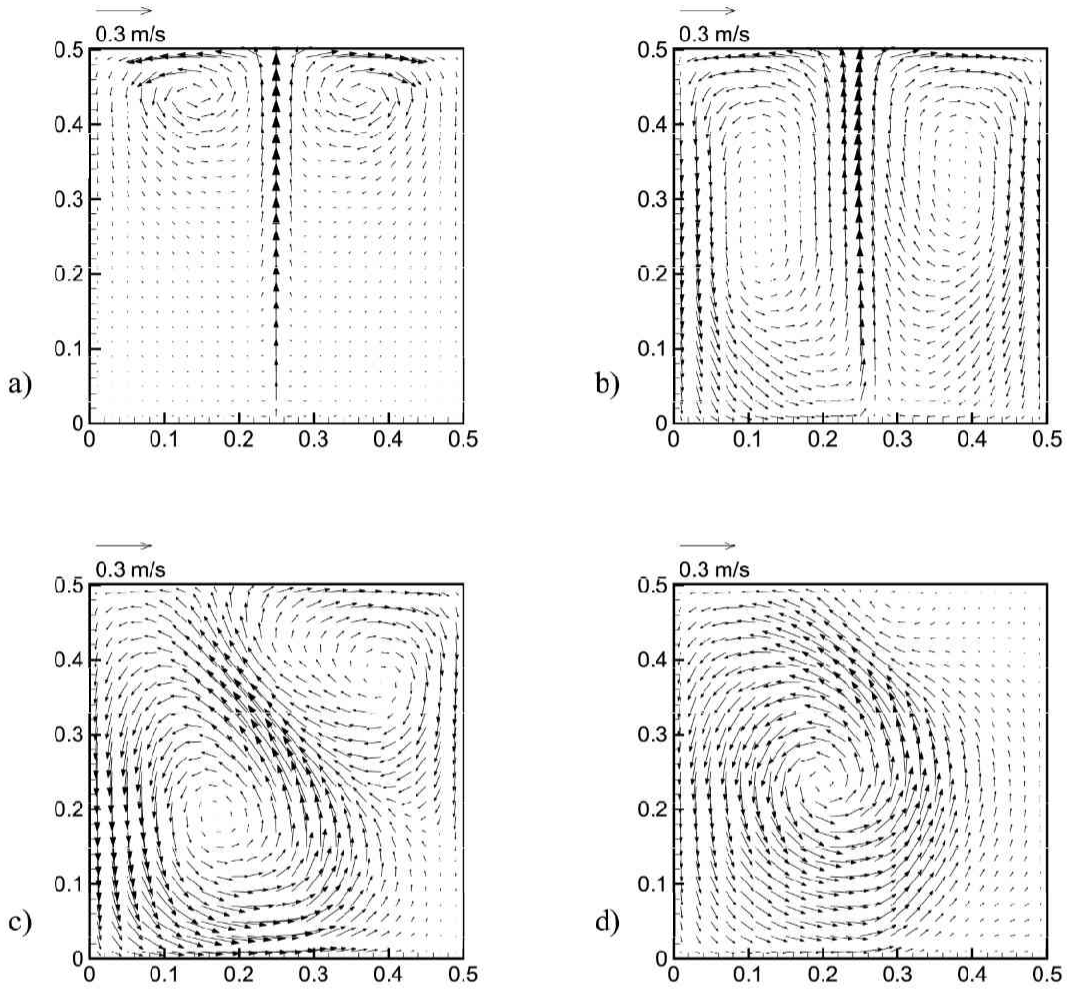

Figure 6.3: Simulation of 0.5m x 0.5m air injection experiment at air flow rate 1L/min: a) t=4 sec, b) t=20 sec, c) t=40 sec and c) t=60 sec.

it can be observed slightly better performance of the former scheme. In the letter case, the vortex is more centered, which is not observed experimentally. Also, the upper part of the flow field is better reproduced by the MUSCL-TVD scheme, where in the QUICK case the flow pattern is more horizontal directed. Therefore, for further simulations, the former scheme will be used.

Comparison of simulated and measured bubble swarm and water velocity distribution for the case of $2L/min$ air flow rate is shown in Figure 6.6. More intensive circulation can be observed, as well as increased air spreading, especially near the water surface.

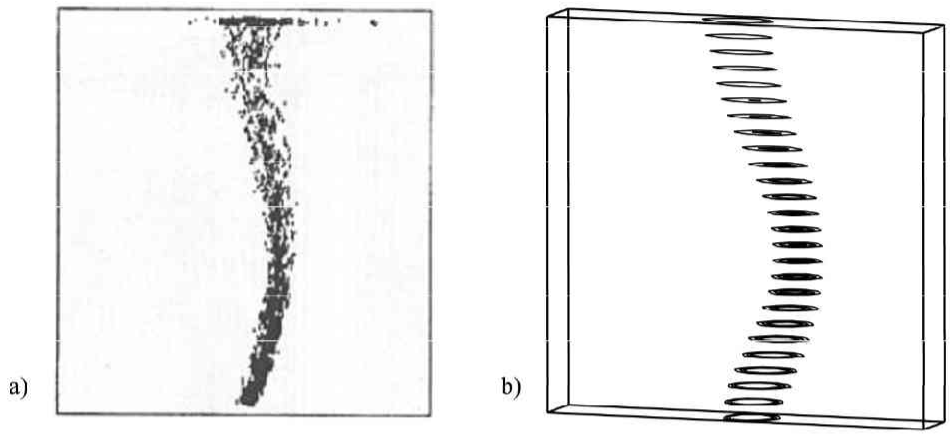

Figure 6.4: Comparison of observed air plume and simulated one for steady conditions: a) experimental observation [Borchers *et al.*, 1999], b) contours of simulated volume of the air plume.

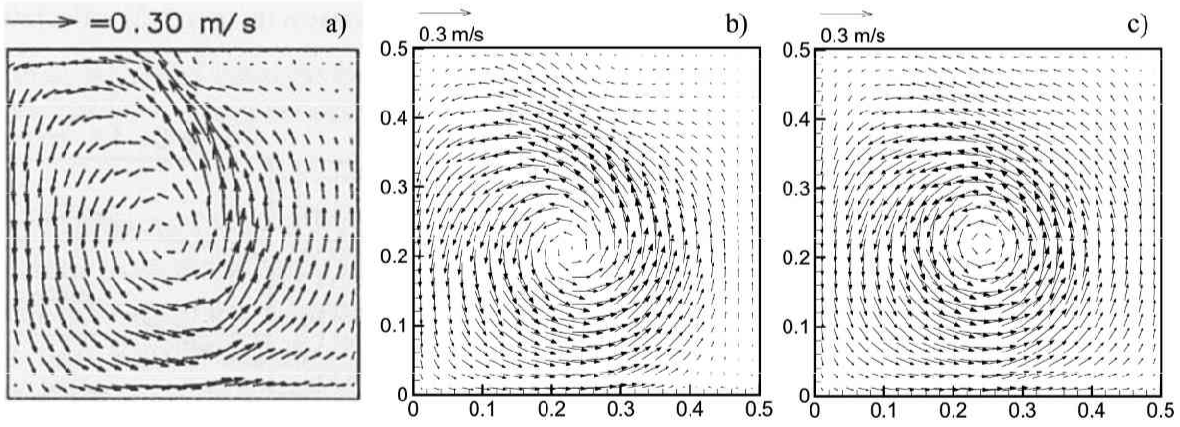

Figure 6.5: Comparison of observed and simulated velocity mid-profile for steady conditions: a) measured water phase velocities [Borchers *et al.*, 1999], b) simulation using the MUSCL-TVD scheme for convective acceleration, c) simulation using the QUICK scheme for convective acceleration.

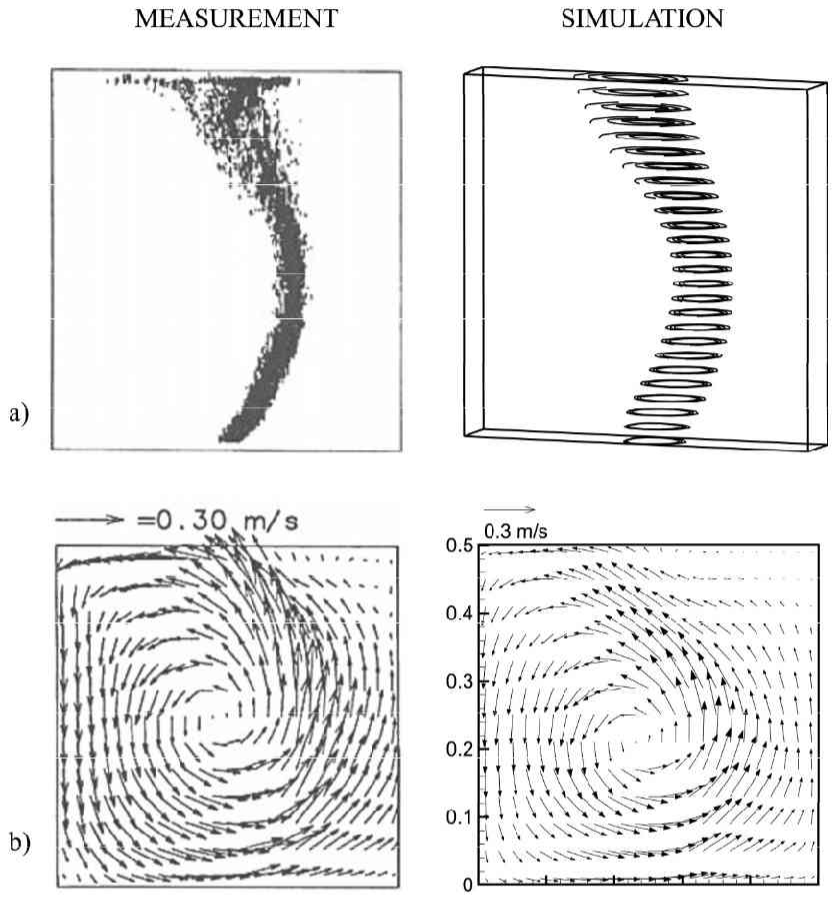

Figure 6.6: Comparison of observed and simulated air distribution and velocity mid-profile for steady conditions ($Q_{air} = 2L/min$): a) comparison of observed and simulated air distribution, b) comparison of velocity mid-profiles.

Simulations without turbulence modeling revealed that previously showed steady states, for both air flow rates, can not be obtained. This is in accordance with conclusions of Sokolichin and Eigenberger [1999].

Case 2:

In this case water column is 100 cm high, i.e. height/width = 2, with 1 L/min air flow rate. It is reported that for this case, no steady state could be established. Transient, periodic flow with two staggered rows of vorticies moving downward was observed. Due to moving vorticies, the bubble plume also periodically bends. Figure 6.7 shows observed and

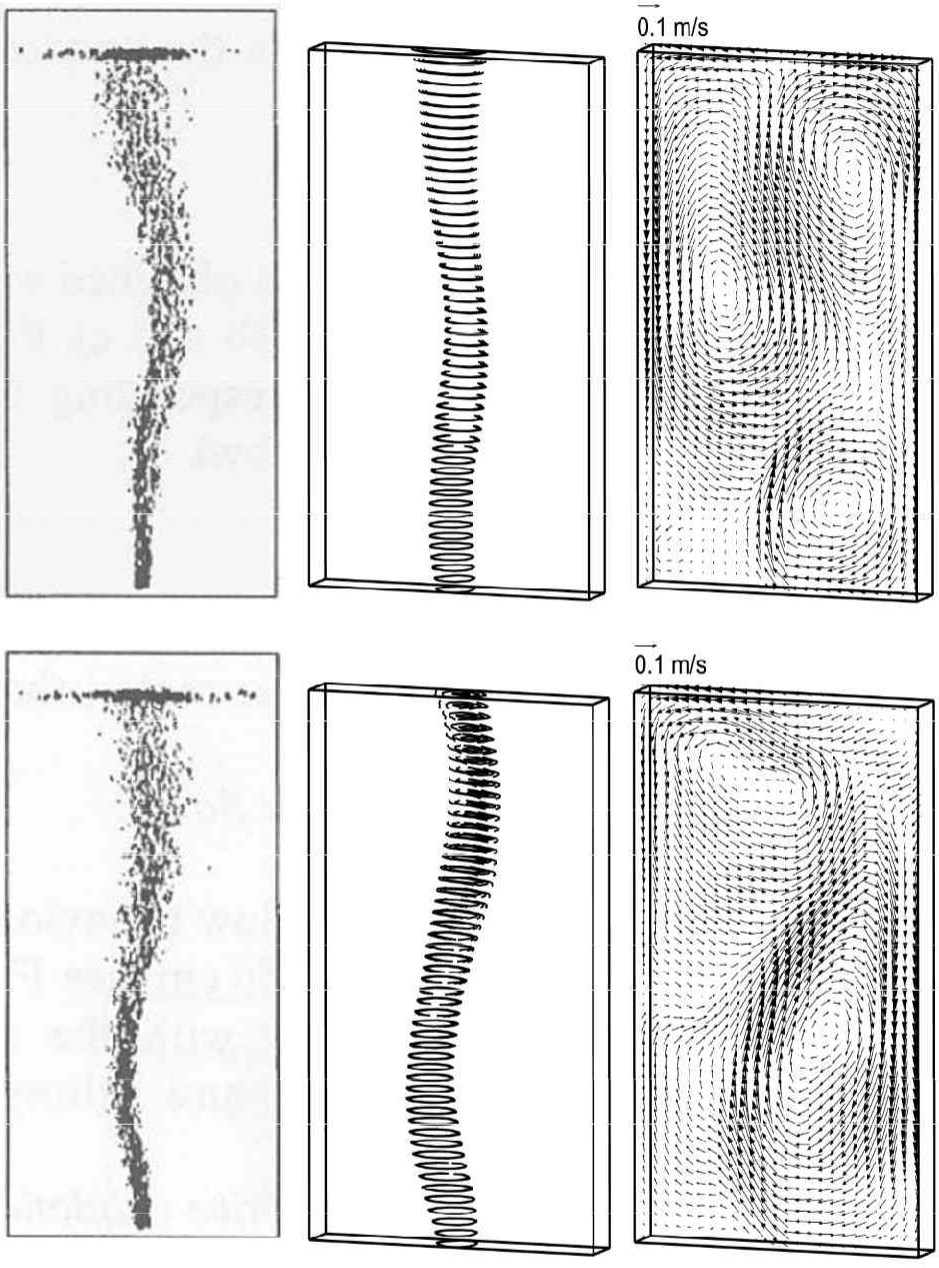

Figure 6.7: Comparison of observed and simulated bubble plumes for two time sections.

simulated bubble plumes at two time sections. Velocity profiles clearly show vorticies causing plume wandering.

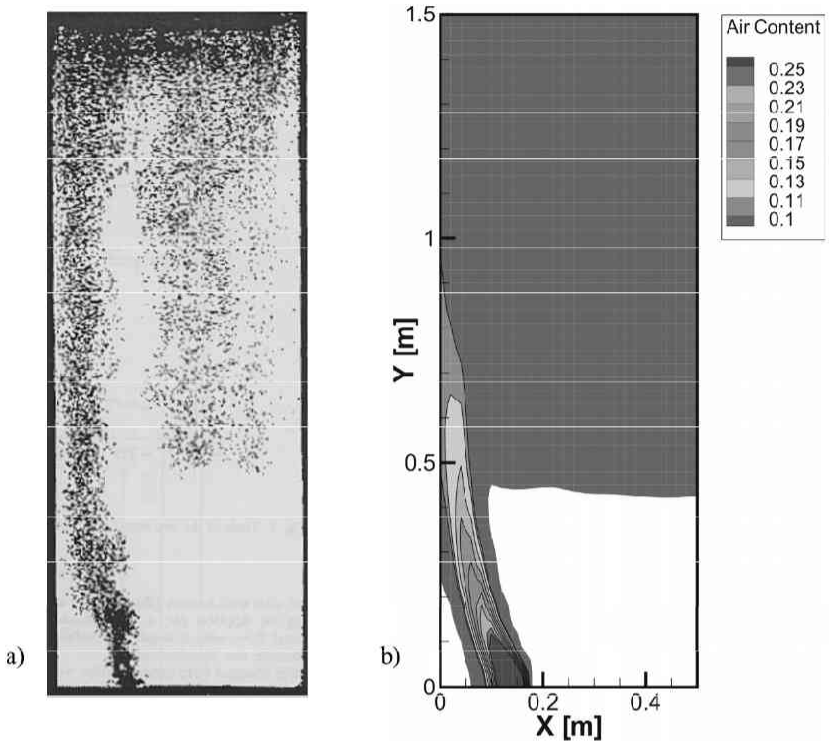

Figure 6.8: Comparison of observed and simulated bubble plumes for 1.5m water column and shifted air injection point ($Q_{air} = 8L/min$): a) observed image, [Becker *et al.*, 1994], b) simulation - steady state.

Case 3:

In this experiment the water column is 150 cm high, and air injection point is shifted form the center for 10cm toward left wall. Simulated air injection flow rate is 8L/min. A circulation is observed which forces the bubble plume to one side. Near the water surface, some amount of bubbles is driven by strong water vortex downward, toward the column bottom. Ratio of buoyancy force and vortex drag determines the depth to which the air will be driven. Comparison of observed and simulated air distribution is shown in Figure 6.8. A good agreement of depth up to which the air is driven by the vortex can be seen, as well as general shape of the air plume. However, model produced more uniform air distribution in this zone in comparison with observed distribution.

6.5 Simulation of oxygen dissolution

Developed and, in previous section, verified numerical model is applied on hypothetical case of pure oxygen injection at the bottom of 50m-deep lake. Oxygen injection rate of $2L/min$ is adopted for simulation. In order to simulate dissolved oxygen transport in the water phase, an additional equation of mass conservation in water phase is solved:

$$\frac{\partial\left(\alpha_w C_{O_2}\right)}{\partial t}+\frac{\partial\left(C_{O_2}\alpha_w V_{wj}\right)}{\partial x_j}-\frac{\partial}{\partial x_j}\left(\alpha_w D_w\frac{\partial C_{O_2}}{\partial x_j}\right)+G_{aw} \tag{6.38}$$

where C_{O_2} is the dissolved oxygen (DO) and D_w is the oxygen diffusion coefficient in water ($1.97\cdot 10^{-5}cm^2/s$). Again, the MUSCL-TVD numerical scheme is applied for calculation of the advective term.

Two simulation approaches are compared: (1) simulation with equilibrium assumption, where concentration in the water phase is determined by the gas phase pressure and Henry's constant, and (2) simulation with non equilibrium mass transfer, according to equation (6.10). In the former case, the mass transfer rate at each time step, required in the continuity equations is calculated from equation (6.38). Initial bubble diameter is assumed as $0.1mm$.

Figure 6.9 shows DO concentrations at three time sections after start of oxygen injection for the case of equilibrium assumption. Due to large dissolution rate, in this case the whole amount of injected oxygen is dissolved within first one meter from the injection point. Further DO spreading is a consequence of imposed momentum, as well as diffusion process.

Completely different behavior is observed with non equilibrium mass transfer calculation (Figure 6.10), which is a more realistic case. Significantly smaller, approximately an order of magnitude, concentrations of DO are observed. Due to entrainment of ambient water into the bubble plume, a minimal spreading of DO can be expected. Therefore, different injection strategy should be considered, such as moving injection point or pulsed injection. Presented numerical model can be utilized to analyze these options in terms of finding the optimal amelioration strategy. Equilibrium assumption obviously significantly overestimates dissolution rate, and should not be used for simulation of oxygen dissolution.

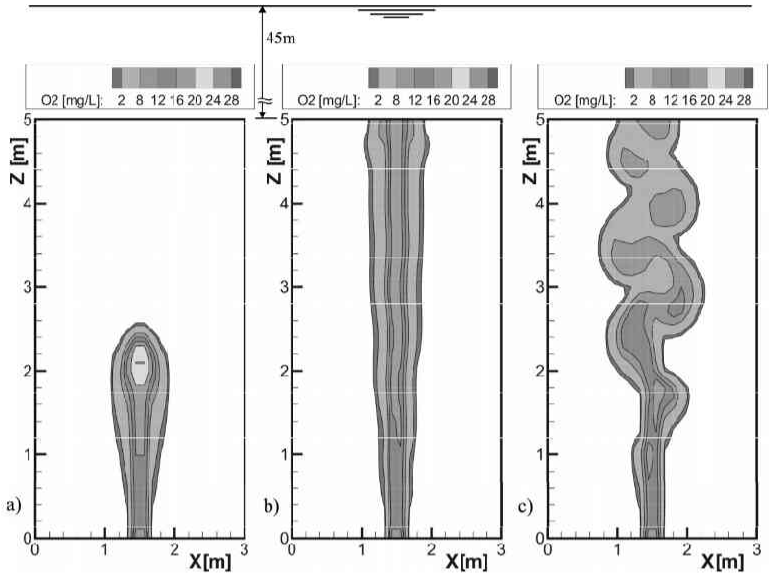

Figure 6.9: Simulated DO concentrations for $2L/min$ pure oxygen injection and equilibrium oxygen dissolution assumption: a) $t = 1min$, b) $t = 3min$ and c) $t = 4min$ after start of oxygen injection.

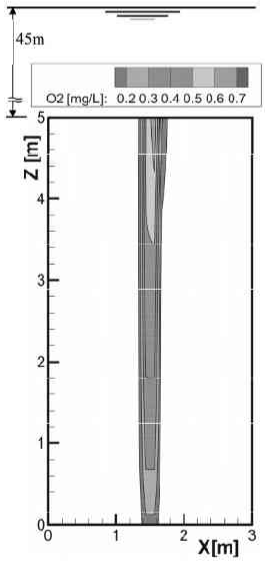

Figure 6.10: Simulated DO concentrations for $2L/min$ pure oxygen injection and non-equilibrium oxygen dissolution rate.

6.6 Summary

In this section, the applicability of developed numerical model to simulation of bubble plumes with/without mass exchange is examined. The model required several refinements to account important mechanisms involved in gas/water flows. This included additional terms in continuity equations, where compressibility of the air phase is introduced, as well as mass exchange between the phases. The drag term in momentum equations is also adjusted, according to reported relations for the drag, added mass and lift forces. In addition, it is confirmed that inclusion of a full 3D turbulence model is essential in order to simulate experiments in flat water tanks.

A modified HSMAC method is proposed, in order to obtain flow fields for both phases. Model is firstly applied to several reported experiments of bubble plumes in a flat water column. Simulation results showed good overall agreement with observations for both observed flow configurations: where the steady state is achieved, and cases where steady conditions can not develop. Based on these results, it is reasonable to assume that proposed model can reliably simulate amelioration of deep lakes by gas injection.

Hypothetical case of pure oxygen injection is simulated. Two models of oxygen dissolution are compared: (1) model based on equilibrium mass transfer, and (2) more realistic model of non-equilibrium dissolution, defined by equation (6.10). The equilibrium model produced approximately an order of magnitude higher DO concentrations. Simulation also revealed that, due to ambient water plume entrainment, significant spreading of dissolved oxygen concentrations can not be expected. Therefore, an alternative injection strategy should be considered.

Chapter 7

Model Application: Simulation of flows in complex flow domains

7.1 Preliminaries

Many practical problems involve complex flow domains consisting of clear fluid and flow through the porous media. Applications include ground water / surface water pollution and flow problems, geophysical systems, oil production, etc. Penetration of fluid from reservoir into some kind of porous media is also significant phenomena in various fields of industry (e.g. ink jet technologies), where the accompanying process of heat transfer can also be of interest. In practice, problem involves coupling of equations describing fluid region flow (Navier-Stokes equations) and flow through porous media, usually described by some form of Darcy-law equation. Due to different structure of these equations, some empirical conditions on the interface between regions are required. Beavers and Joseph [1967], amongst the first, proposed a "slip-flow" condition at the interface. Based on experimental results, they concluded that slip velocity is proportional to the shear rate on the interface.

After Wooding [1957], who introduced convective inertia term in the Darcy law equation, resembling in that way Navier-Stokes equations, Beckermann et al. [1988] solved coupled equations (for fluid and porous region) numerically in two dimensions. Their set of governing equations under steady state condition introduces binary parameter, through which transition from porous to fluid region is achieved. On the other hand, inertia effects

in the porous region were introduced using Brinkman and Forchheimer extensions of Darcy law equation.

In this Chapter, the developed multiphase model will be applied for simulation of flow in complex flow domains with free surface boundary. Both flow domains, the clear fluid and porous media, are represented by single set of equations, which are solved simultaneously. Continuity of velocities and stresses across the interface of two regions is assumed.

One of possible applications of presented model is simulation of an embankment overflow, in order to analyze effects of coupled free water and groundwater flow on effective stresses in the soil. However, such application, as well as many others, include flow domains with irregular boundaries. Since the developed model is formulated on finite volumes, one approach could be to discretize the slope of embankment with fine enough stair-stepped quadrilateral volumes. This would lead to poor resolution due to coarse grid discretization, or increased computational cost as a result of mesh refinement. Nevertheless, a more fruitful approach is to formulate model in generalized curvilinear coordinates, so discretization grid can be adapted to any flow domain. The latter approach will be applied herein.

7.2 Model formulation

Simultaneous clear fluid and ground water flow can be described by single set of governing equations, expressed in generalized curvilinear coordinates [Kimura *et al.*, 2002]:

$$\frac{1}{\sqrt{g}}\frac{\partial\left(\alpha_w V^j\sqrt{g}\right)}{\partial\xi^j}=0 \tag{7.1}$$

$$\frac{\partial\alpha_w V^i}{\partial t}+\nabla_j\left(\alpha_w V^i V^j\right)=\alpha_w G^i-\frac{\alpha_w}{\rho}g^{ij}\nabla_j p+\nu\nabla_j\left(\alpha_w g^{ik}\nabla_k V^j+\alpha_w g^{jl}\nabla_l V^i\right)+\frac{1}{\rho}R^i \tag{7.2}$$

where ξ^i is the generalized curvilinear coordinate, V^i is the contravariant component of pore velocity vector, G^i is the contravariant component of gravitational acceleration, g_{ij} and g^{ij} are the covariant and contravariant components of metric tensor, respectively, with $g=det(g_{ij})$, R^i is the contravariant component of the total drag force of porous media, and ∇_i indicates the covariant differential. The drag force exists only in the porous region and it is modeled according to the Darcy law:

$$R^i=-\rho G\frac{\alpha_w^2}{K}V^i \tag{7.3}$$

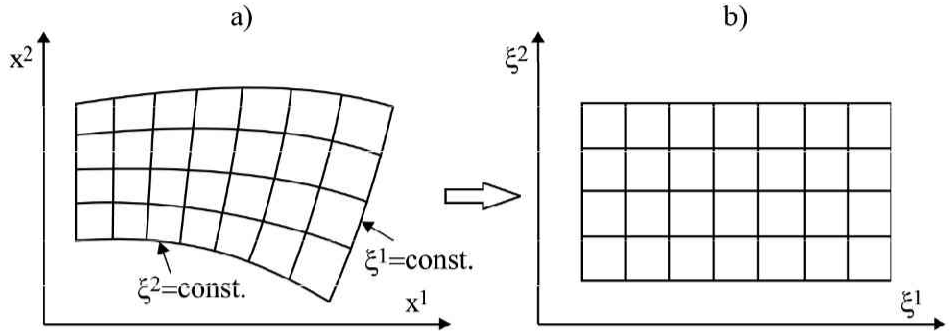

Figure 7.1: Physical (a) and computational (b) mesh.

The relation of Cartesian and generalized curvilinear coordinate systems is shown in Figure 7.1. Covariant and contravariant components of the metric tensor are defined as:

$$g_{kl} - \frac{\partial x^i}{\partial \xi^k}\frac{\partial x^i}{\partial \xi^l} \tag{7.4}$$

$$g^{kl} = \frac{\partial \xi^k}{\partial x^i}\frac{\partial \xi^l}{\partial x^i} \tag{7.5}$$

where x^i are coordinates in Cartesian coordinate system. The summation convention of repeated indicies in above expressions is implied.

Contravariant component of velocity vector in curvilinear coordinate system is transformed from the vector defined in Cartesian coordinates, and vice-versa as (Figure 7.2):

$$V^i = \frac{\partial \xi^i}{\partial x^j}U^j \quad U^j = \frac{\partial x^j}{\partial \xi^i}V^i \tag{7.6}$$

where U^j are components of velocity vector in Cartesian coordinate system.

The covariant derivative of the contravariant vector, figuring in momentum equations (7.2) is defined as:

$$\nabla_k V^i = \frac{\partial V^i}{\partial \xi^k} + V^j \Gamma^i_{jk} \tag{7.7}$$

where Γ^i_{jk} is the Riemann-Christoffel symbol, defined as:

$$\Gamma^i_{jk} = \frac{1}{2}g^{il}\left(\frac{\partial g_{kl}}{\partial \xi^j} + \frac{\partial g_{jl}}{\partial \xi^k} - \frac{\partial g_{jk}}{\partial \xi^l}\right) = \frac{\partial \xi^i}{\partial x^l}\frac{\partial}{\partial \xi^k}\left(\frac{\partial x^l}{\partial \xi^j}\right) = -\frac{\partial x^l}{\partial \xi^j}\frac{\partial}{\partial \xi^k}\left(\frac{\partial \xi^i}{\partial x^l}\right) \tag{7.8}$$

Similarly, the second term in equation (7.2) can be expressed as:

$$\nabla_j\left(\alpha_w V^i V^j\right) = \frac{\partial \alpha_w V^i V^j}{\partial \xi^j} + \alpha_w V^l V^j \Gamma^i_{lj} + \alpha_w V^i V^l \Gamma^j_{lj} \tag{7.9}$$

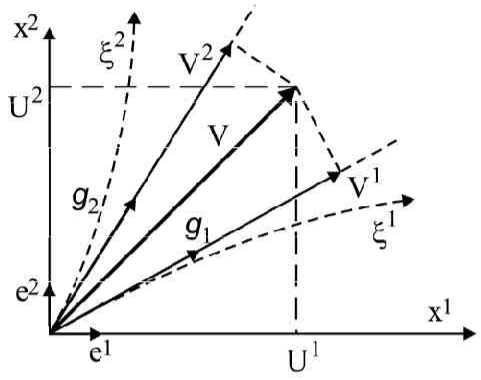

Figure 7.2: Definition of the contravariant components of velocity vector in two dimensions. $V = V^1 g_1 + V^2 g_2$, where covariant base vectors are defined as $g_i = \frac{\partial x^j}{\partial \xi^i} e^j$.

The free surface boundary is tracked utilizing the VOF method, herein adapted for curvilinear coordinates. The according advective equation of fluid volume is expressed as:

$$\frac{\partial (\alpha_w)}{\partial t} + \frac{1}{\sqrt{g}} \frac{\partial (\alpha_w V^j \sqrt{g})}{\partial \xi^j} = 0 \tag{7.10}$$

It should be noted that curvilinear coordinates may introduce a false pressure gradients, if the pressure term is not treated carefully. For example, for hydrostatic pressure distribution, one can write for horizontal direction:

$$\frac{\partial p}{\partial x^1} = 0 \tag{7.11}$$

However, discretized equations in curvilinear coordinates, in general case will produce a false gradient:

$$\frac{\partial p}{\partial \xi^j} \frac{\partial \xi^j}{\partial x^1} \neq 0 \tag{7.12}$$

due to which the false flow may occur for hydrostatic conditions. Therefore, in presented model the pressure gradients are firstly calculated in the Cartesian coordinates, and then transformed to contravariant components in curvilinear coordinates. In other words, the pressure term in equation (7.2) is calculated as:

$$g^{ij} \nabla_j p = \frac{\partial p}{\partial x^j} \frac{\partial \xi^i}{\partial x^j} \tag{7.13}$$

In order to calculate pressure gradients in Cartesian coordinates ($\partial p / \partial x^j$), pressures have to be interpolated on respective planes, as shown in Figure 7.3. Referring to the Figure,

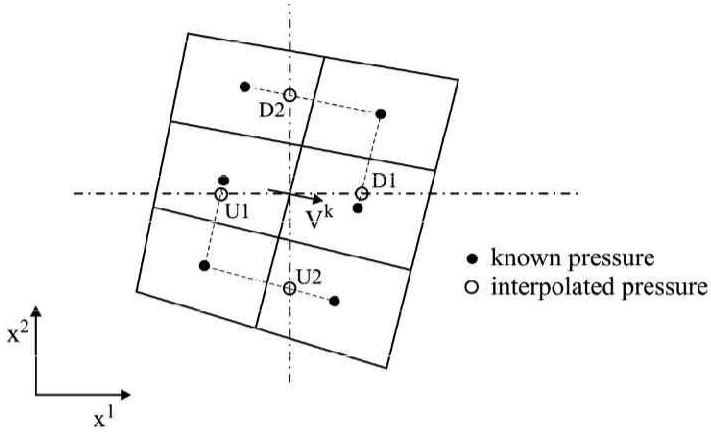

Figure 7.3: Calculation of pressure terms in curvilinear coordinates in order to avoid occurrence of false gradients: Example for the momentum equation of velocity V^k for a two-dimensional case. Pressures are firstly interpolated on x^1 and x^2 lines passing through the point where the velocity is defined. Gradients from interpolated pressures are estimated in Cartesian coordinates, and then contravariant components are calculated.

where a two-dimensional example is shown, pressure gradients in Cartesian coordinates are estimated as:

$$\frac{\partial p}{\partial x^1} \approx \frac{p_{D1} - p_{U1}}{x^1_{D1} - x^1_{U1}} \quad \frac{\partial p}{\partial x^2} \approx \frac{p_{D2} - p_{U2}}{x^2_{D2} - x^2_{U2}} \tag{7.14}$$

7.3 Simulation of embankment overflow and its application on the slope failure potential estimation

7.3.1 Flow simulation

A simple flow domain is adopted for analysis of effects of combined free surface and ground water flow on slpe failure potential. The slope value of 1:2 us adopted with the slope height of 0.5m. Simulated porous medium is extended to three slope heights below the slope toe. At the porous medium vertical boundaries, the zero pressure gradient is applied on the left side , and hydrostatic pressure at the right side as a boundary condition. After reaching the full embankment saturation, the hydraulice head at the soil surface, at the right domain side is applied, in order to provide realistic conditions.

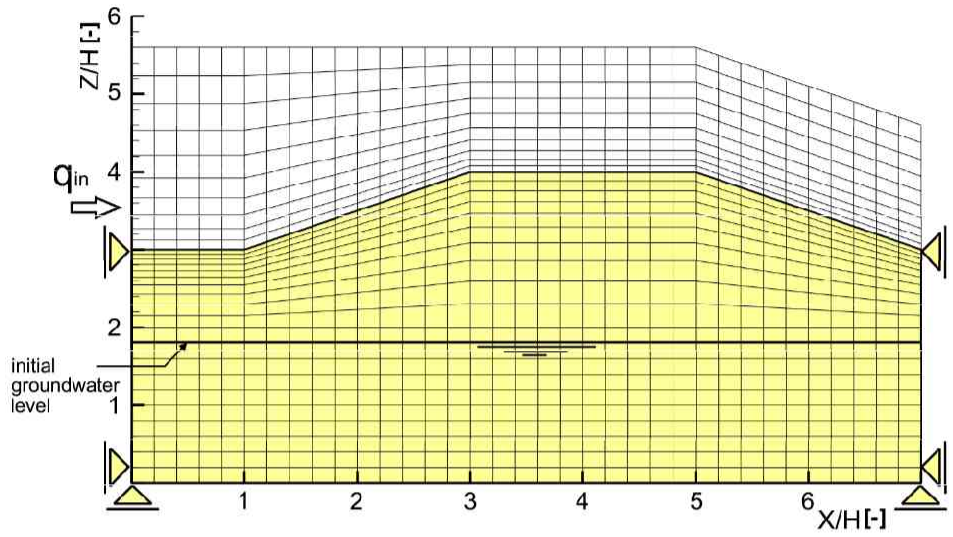

Figure 7.4: Calculation mesh, boundary and initial conditions for embankment overflow simulation.

For the bulk water flow, the constant influx on the left boundary is applied and a "free exit" boundary condition is applied on the right side. Figure (7.4) schematically shows the simulated flow domain with discretization mesh, initial and boundary conditions. All lengths in the figure are scaled with the embankment height. Hydraulic conductivity of the porous medium is adopted as $K = 1 \cdot 10^{-3} m/s$, and porosity $\phi = 0.4$.

The intention of the simulation is to demonstrate ability of developed model to simulate flow in complex flow domains with irregular boundaries. Capillarity is neglected in this simulation; however, since the hydraulic permeability is adopted as quite high, these effects can be considered as negligible.

Figures 7.5 and 7.6 show simulation results for several time sections after start of discharge ($q = 100\, L/m\, s$) from the left side. The steady conditions for the bulk fluid overflow is approached very fast, while the infiltration into the embankment continues for longer time period. At the upstream side, this process is faster, due to higher pressures on the surface, while on the downstream side this process is slower. The flow field in the embankment after full saturation is shown in Figure 7.7. Hydraulic gradient toward the slope surface can be seen at the downstream slope of the embankment.

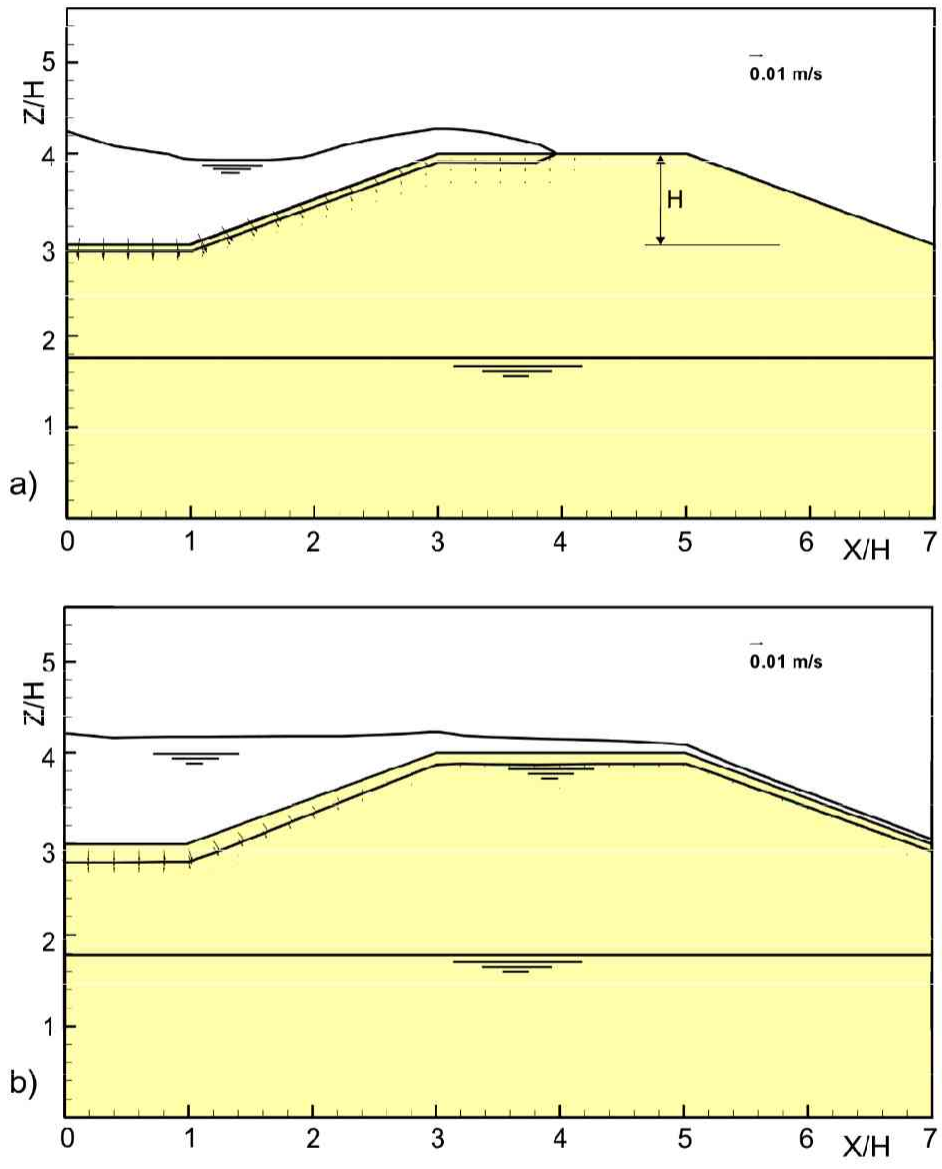

Figure 7.5: Simulation of embankment overflow: a) 0.5 sec. after start of simulation, b) 5 sec. after start of simulation.

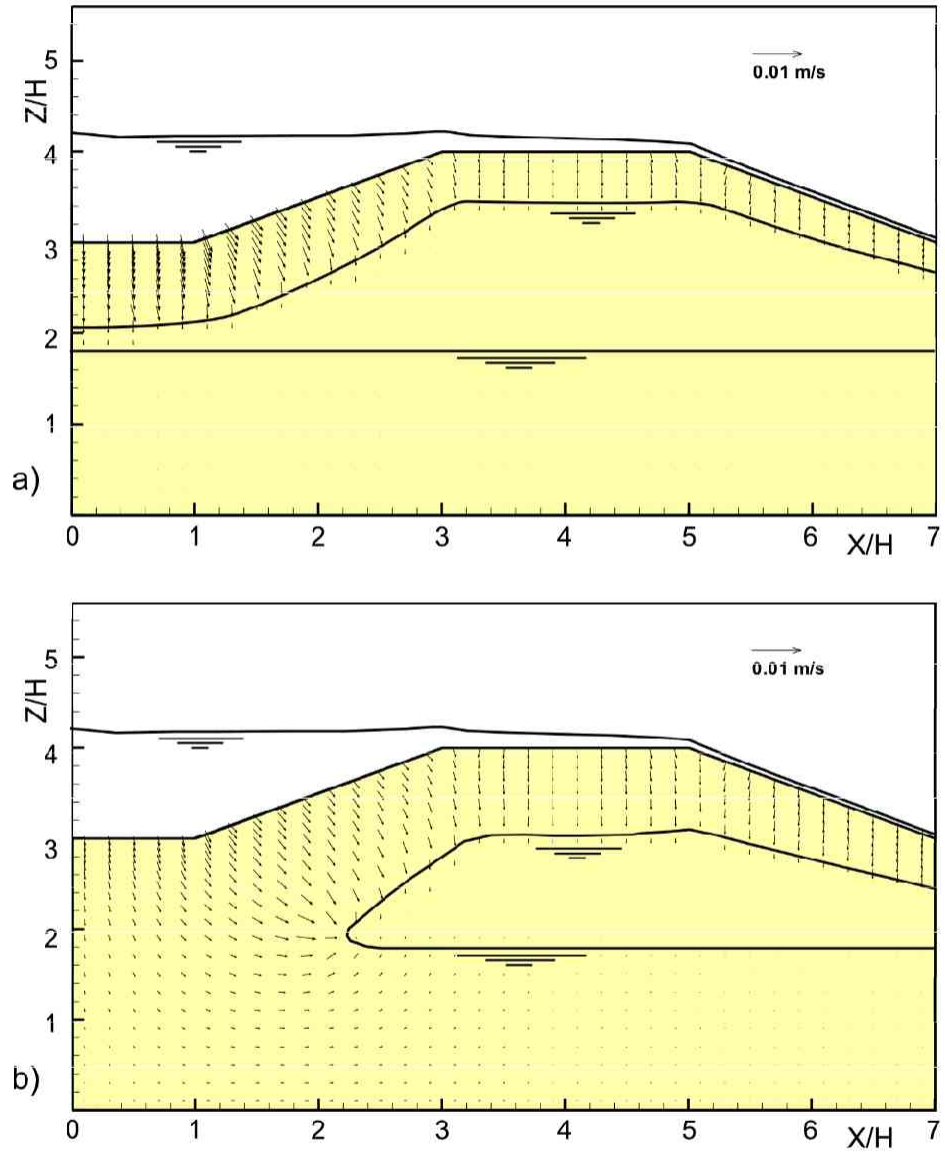

Figure 7.6: Simulation of embankment overflow: a) 45 min. after start of simulation, b) 90 min. after start of simulation.

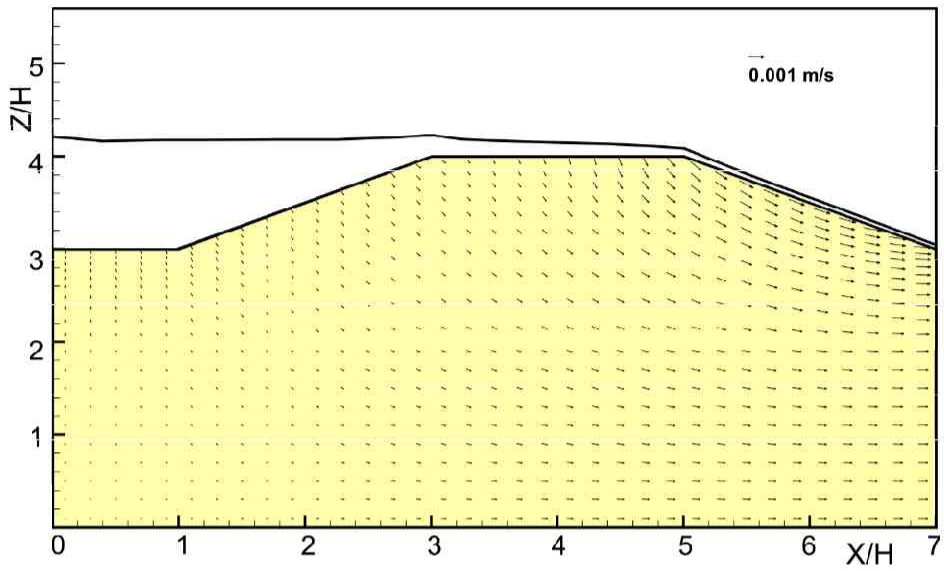

Figure 7.7: Simulation of embankment overflow: Steady conditions with full embankment saturation.

7.3.2 Effective stresses and slope failure potential analysis

As an application, results of flow simulation of coupled, clear water and groundwater flow, can be utilized for analysis of effective stresses in the soil. A traditional approach in analysis of the slope stability (a limit equilibrium approach) implies analysis of total forces acting on the assumed failure surfaces. In this study, a different approach will be utilized, where effective stresses in the porous medium will be calculated, and effects of groundwater and surface flow on slope failure potential will be quantified.

A fundamental, illustrative analysis will be conducted herein, without considering many important issues, such as soil cohesion, capillary pressure and slope erosion by the surface flow.

In order to analyze the effects of water flow on effective stresses in the porous media, numerical model for water flow is coupled with a FEM numerical model for elastic stress-strain calculation in porous medium, based on Hooke's law. Traditional Cauchy's equations for a static continuum [e.g. Malvern, 1969] in Cartesian coordinates, which are solved herein, are derived from the momentum equation (2.49), written for the fixed, incompressible and

saturated soil phase:

$$0 = -(1-\phi)\rho_s G\frac{\partial x_3}{\partial x_i} - (1-\phi)\frac{\partial p}{\partial x_i} + \frac{\partial\left(1-\phi\right)\tau'_{ij}}{\partial x_j} + F_i \tag{7.15}$$

where τ'_{ij} is the effective stress tensor in the soil phase, ρ_s is the soil density, ϕ is the porosity, and F_i is the drag force. The x_3 axis is considered as oriented vertically upward.

Now, the drag force, can be expressed from the momentum equation for the water phase, in which the inertial and viscous terms are neglected:

$$0 = -\phi\rho_w G\frac{\partial x_3}{\partial x_i} - \phi\frac{\partial p}{\partial x_i} - F_i, \tag{7.16}$$

and fluid pressure can be expressed via the hydraulic head:

$$h = \frac{p}{\rho_w G} + x_3 \tag{7.17}$$

Summation of equations (7.15) and (7.16), with substitution of (7.17) gives:

$$\frac{\partial\left(1-\phi\right)\tau'_{ij}}{\partial x_j} = \left(\rho_t - \rho_w\right)G\frac{\partial x_3}{\partial x_i} + \rho_w G\frac{\partial h}{\partial x_i} \tag{7.18}$$

in which ρ_t is the bulk density of the porous medium (solid-fluid mixture). In all these equations, normal stresses are defined as positive in tension. From equation (7.18) it is clear that existence of water in the porous medium affects the effective stresses in two ways: (1) through the buoyancy (the first term on the right side), and (2) through the seepage forces expressed through the second term on the right side.

Since in this study a two-dimensional problem in vertical plane is considered, equation (7.18) will be written in Cartesian coordinates, for horizontal and vertical direction, respectively:

$$\frac{\partial\left(1-\phi\right)\tau'_{xx}}{\partial x} + \frac{\partial\left(1-\phi\right)\tau'_{zx}}{\partial z} = \rho_w G\frac{\partial h}{\partial x} \tag{7.19}$$

$$\frac{\partial\left(1-\phi\right)\tau'_{xz}}{\partial x} + \frac{\partial\left(1-\phi\right)\tau'_{zz}}{\partial z} = \left(\rho_t - \rho_w\right)G + \rho_w G\frac{\partial h}{\partial z} \tag{7.20}$$

In order to calculate effective stresses in porous medium, it is necessary to include relations between stresss and strains [Iverson and Reid, 1992]:

$$(1-\phi)\tau'_{xx} = -\frac{E}{(1-\vartheta)}\left(\frac{\partial u_x}{\partial x}\right) - \frac{\vartheta E}{(1-2\vartheta)(1+\vartheta)}\left(\frac{\partial u_x}{\partial x} - \frac{\partial u_z}{\partial z}\right) \tag{7.21}$$

$$(1-\phi)\tau'_{zz} = -\frac{E}{(1+\vartheta)}\left(\frac{\partial u_z}{\partial z}\right) - \frac{\vartheta E}{(1-2\vartheta)(1+\vartheta)}\left(\frac{\partial u_x}{\partial x} + \frac{\partial u_z}{\partial z}\right) \tag{7.22}$$

$$(1-\phi)\tau'_{xz} = (1-\phi)\tau'_{zx} = \frac{\vartheta E}{2(1+\vartheta)}\left(\frac{\partial u_x}{\partial z} + \frac{\partial u_z}{\partial x}\right) \tag{7.23}$$

where u_x and u_z are infinitesimal displacements in x and z directions, respectively, E is the Young's modulus and ϑ is the Poisson's ratio of the porous material.

Substitution of equations (7.21) ... (7.23) into (7.19) and (7.20) gives:

$$A\left(\frac{\partial^2 u_x}{\partial x^2} + \frac{\partial^2 u_x}{\partial z^2}\right) + B\left(\frac{\partial^2 u_x}{\partial x^2} + \frac{\partial^2 u_z}{\partial x\,\partial z}\right) = \rho_w G\frac{\partial h}{\partial x} \tag{7.24}$$

$$A\left(\frac{\partial^2 u_z}{\partial x^2} + \frac{\partial^2 u_z}{\partial z^2}\right) + B\left(\frac{\partial^2 u_z}{\partial z^2} + \frac{\partial^2 u_x}{\partial x\,\partial z}\right) = (\rho_t - \rho_w)\,G + \rho_w G\frac{\partial h}{\partial z} \tag{7.25}$$

where parameters A and B are defined as:

$$A = \frac{E}{2\,(1+\vartheta)} \quad B = \frac{E}{2\,(1+\vartheta)} + \frac{\vartheta E}{(1-2\vartheta)\,(1+\vartheta)} \tag{7.26}$$

For given boundary conditions in terms of infinitesimal soil displacements, as showed in Figure 7.4, imposed shear stress at the surface due to bulk water flow, and hydraulic gradients due to groundwater flow, equations (7.24) and (7.25) are solved numerically. For obtained displacements, corresponding normal and shear stresses are calculated from equations (7.21) ... (7.23). Now, principal stresses can be calculated from the Mohr's circle:

$$\sigma_1 - \frac{\tau'_{xx} + \tau'_{zz}}{2} + \sqrt{\left(\frac{\tau'_{xx} - \tau'_{zz}}{2}\right)^2 + {\tau'_{zx}}^2} \tag{7.27}$$

$$\sigma_2 = \frac{\tau'_{xx} + \tau'_{zz}}{2} - \sqrt{\left(\frac{\tau'_{xx} - \tau'_{zz}}{2}\right)^2 + {\tau'_{zx}}^2} \tag{7.28}$$

where directions of principal stresses are rotated from the x-z axis by an angle γ:

$$\gamma = \frac{1}{2}\arctan\left(\frac{2\tau'_{zx}}{\tau'_{xx} - \tau'_{zz}}\right) \tag{7.29}$$

An slope failure potential will be quantified by the Coulomb failure rule for the cohesionless material [Iverson and Reid, 1992]:

$$\Phi = \frac{|\tau'_{max}|}{-\sigma_m} \tag{7.30}$$

where Φ is the slope failure potential, τ'_{max} is the maximum shear stress, and σ_m is the mean principal stress. Theoretically, Φ has the value between zero and one; the latter implying the failure. In the case of tension, the value of Φ has no meaning, since the soil is considered as cohesionless.

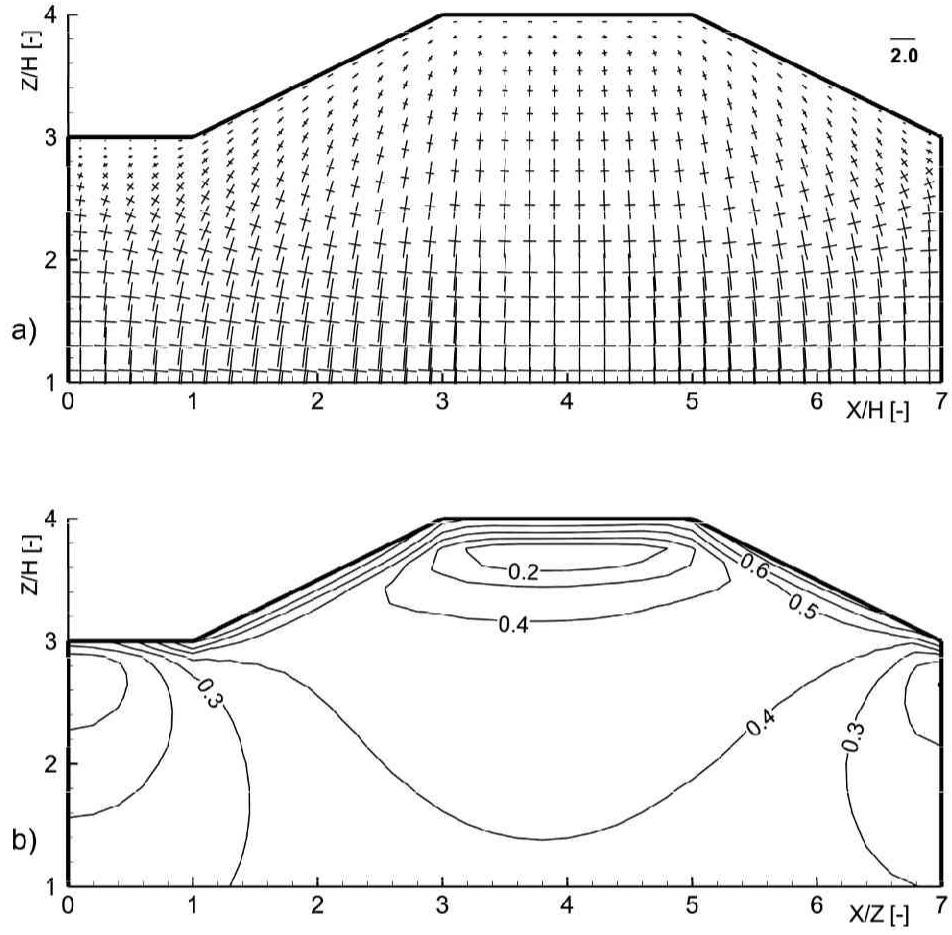

Figure 7.8: Principal stresses and failure potential coefficients for the dry soil case: (a) principal stresses (all compressional), scaled by $\rho_w GH$, and b) calculated failure potential coefficients.

Figure 7.8 - a) shows principal stresses for the dry soil case, scaled by the factor $\rho_w GH$. Soil parameter values are adopted as follows: ρ_t(dry)= $1600kg/m^3$, ρ_t(saturated)= $2000kg/m^3$, $\rho_w = 1000kg/m^3$, and $\vartheta = 0.333$. Maximum compressive stresses are oriented parallel to the surface in the zone near the slope surfaces. With the depth, maximum stresses become vertical, aligned with direction of the gravity.

Corresponding failure potential contours for the dry soil case, is shown in Figure 7.8 - b). It can be seen that maximum values occur near the slope surface, and that the zone of high Φ values is relatively shallow.

Figure 7.9 shows comparison of the failure potential contours at the downstream slope, for dry soil condition and after obtaining total saturation of the porous medium. It can be observed that combined effects of buoyancy, seepage forces and shear forces of the surface flow, generally increased the failure potential values. This increase is especially significant in the zone of the slope surface, near the slope toe, where it almost reached the theoretical maximum of one. In addition, the zone of higher Φ values is increased in comparison with the dry conditions. Figure 7.10-a) shows the increase expressed in percents. Effects of water flow on principal effective stresses can be seen in Figure 7.10-b). The zone of principal stresses parallel to the surface slope is increased in comparison with dry soil case. Also, due to hydraulic gradients near the slope toe, principal stresses are significantly rotated in this zone.

Based on these results, it can be speculated that surface erosion along the slope increases the hydraulic gradients toward the slope surface, which in turn, increases the failure potential coefficients in this zone. This again, promotes the erosion. It can be concluded that overall process is self-amplifying, which ultimately leads toward the embankment failure.

7.4 Summary

In this chapter, developed numerical model is further refined in order to simulate flows in complex flow domains, consisting of bulk fluid and flow in porous media. In addition, by formulation in boundary-fitted, curvilinear coordinates, model can be applied for simulation of flow domains with irregular boundaries.

Assuming the continuity of velocities and stresses at the boundary between two regions, the problem of coupled flow domains is formulated by single set of governing equations. Model is applied for hypothetical simulation of embankment overflow, where the combined effects of free surface and groundwater flow on effective stresses in porous media are analyzed. It is found that the water flow significantly influences the failure potential, which is quantified by calculation of the Coulomb failure potential.

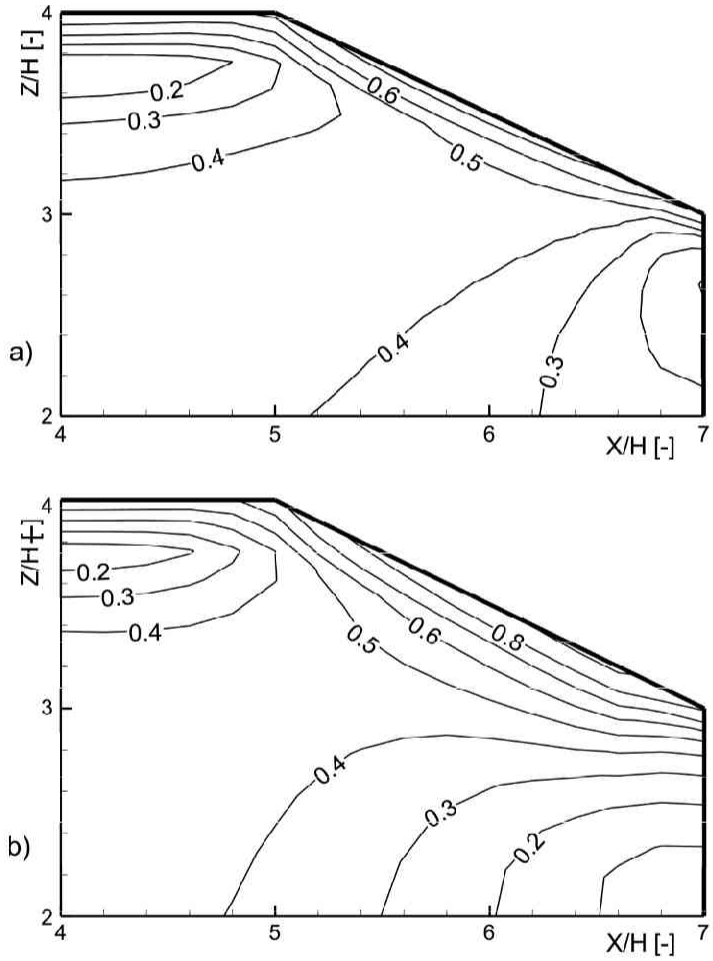

Figure 7.9: Comparison of calculated failure potential contours at the downstream slope: (a) dry soil conditions, and b) saturated soil conditions.

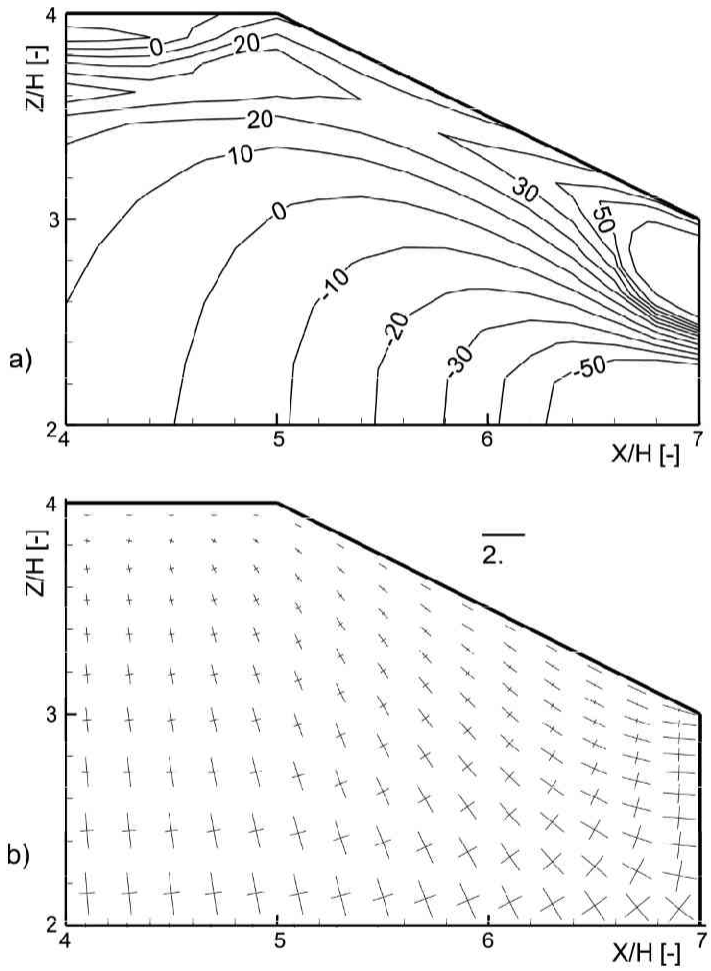

Figure 7.10: Increase of the failure potential (%) due to combined clear water and groundwater flow in comparison to the dry soil conditions-(a), and principal stresses scaled by $\rho_w GH$-(b).

Chapter 8

Conclusions and Recommendation

8.1 Conclusions

In this study a mechanistic numerical model for simulation of multiphase flows in porous media and/or bulk fluid has been developed. After its validation, model is applied for simulation of a variety of hydraulic engineering problems.

Firstly, developed model is utilized to investigate the role of local acceleration in the process of pressure redistribution in a deep porous media. This term is commonly neglected in the simulation of saturated flows in porous media. A simple example of flow initiated after tunnel excavation is considered, where two cases are analyzed: (1) the case of homogeneous medium and (2) the case with less permeable lining around the tunnel excavation. For both cases analytical solution for the symmetry line above the excavation has been derived, under assumption that vertical velocity distribution along this line is linear and that water and soil are incompressible. In the homogeneous case, it is found that pressure adapts to the new boundary conditions instantaneously, while the velocity profile develops from zero to quasi-steady condition very fast. This change of the velocity is numerically reproduced very well. Only during this period, the acceleration term plays a role. It is observed that required time to quasi-steady condition is proportional to hydraulic permeability value. Obtained analytical pressure distribution is in good agreement with numerical results, especially near the excavation, while the calculated velocities are in excellent agreement. Deviation in the analytical solutions is prescribed to the assumption of linear velocity distribution along

the symmetry line. In the heterogeneous case, however, there is a transient period for the pressure, as well as for the velocity distribution. Pressure changes from the homogeneous solution toward the quasi-steady distribution in a short time, proportional to the hydraulic permeability of the soil. It is revealed that quasi-steady pressure distribution depends on the permeability ratio between the lining and the medium, not on their absolute values.

Model has been successfully used for simulation of air/water flow during the air sparging. Here also, the traditional modeling approach excludes acceleration terms in momentum equations. Therefore, an analysis was conducted in order to analyze conditions for which this approximation can be valid. Numerical experiments showed that inertial effects become significant in the porous media with averaged grain diameter larger than 2 mm. This limit coincides with the transition from the channel air flow pattern toward the bubble flow pattern in previously saturated porous medium. Model is also used to simulate experimentally observed pulsation phenomena, where it was showed that only by modeling of acceleration terms this can be reproduced. The pulsation is also analyzed from the theoretical point by conducting a one-dimensional linear stability analysis. It is showed that acceleration promotes the instability, while the capillary forces oppose it. The ratio of these forces determines an onset of instability.

The numerical model for air sparging simulation has been also extended by inclusion of contaminant transport/transfer mechanisms in the air and water phase. In a traditional mechanistic model, a common approach is to consider air and water phases as completely mixed. Presented model, in contrast, considers the channel air flow pattern, which can be expected in the most of practical applications. Model has been validated by comparison with two-dimensional experiment, reported in the literature. Very good agreement between calculated and measured contaminant concentrations is observed.

Developed model has been further refined in order to simulate bubble plumes, occurring after air/gas is injected into clear water. The model required several refinements to account important mechanisms involved in gas/water flows. This included additional terms in continuity equations, where compressibility of the air phase is introduced, as well as mass exchange between the phases. The drag term in momentum equations is also adjusted, according to reported relations for the drag, added mass and lift forces. In addition, it is confirmed that inclusion of a full 3D turbulence model is essential in order to simulate ex-

periments in flat water tanks. The bubble plume model showed very good quantitative and qualitative agreement between simulated and experimentally reported results. Therefore, it is assumed that model can be reliably used for simulation of gas injection into deep lakes for amelioration purposes. Simulation of hypothetical pure oxygen injection showed that, due to ambient water plume entrainment, significant spreading of dissolved oxygen concentrations can not be expected. Therefore, an alternative injection strategy should be considered.

Additional model refinement is conducted in order to provide an application to flow domains with irregular boundaries. The model is applied for simulation of coupled, clear water and groundwater flow during the embankment overflow. The flow in complex flow domain is modeled by solving a single set of governing equations, valid in both regions. Results of flow simulation are utilized to analyze effects on effective stresses in an elastic soil. It is found that coupled buoyancy, hydraulic gradient and surface shear stress significantly influence slope failure potential, herein quantified by Coulomb failure coefficient.

8.2 Recommendation

In the case of air sparging simulations in coarse soils, the further numerical and experimental investigations of the drag term in momentum equations is required. This issue is not resolved satisfactorily in the literature yet. In the presented model, the modified Ergun resistance is used. However, it is not clear whether it holds for the air/water bubbly flow. Considering the contaminant removal modeling, a further model validation on the laboratory and in-situ scales is required. Since it is confirmed that limiting process of contaminant removal is the diffusive transport of contaminants toward the air phase, the purpose of these simulations would be to further examine the dependence of mass transfer coefficient between the immobile and the mobile water phase on other involved variables, such as soil physical and hydraulic parameters, contaminant characteristics, air distribution etc.

Simulations of laboratory experiments of bubble plumes in clear water showed that turbulence modeling has a great impact on obtained results. In presented model, a standard $k-\epsilon$ model is utilized. This model does not include the bubble induced turbulence, which may play an important role, especially for higher air injection flow rates. Further research (experimental and numerical) is required for appropriate modeling of this term.

References

Adams, J. A. and K. R. Reddy (1999), Laboratory Study of Air Sparging of TCE-Contaminated Saturated Soils and Ground Water, *Ground Water Monitoring and Remediation , Summer, 1999*: pp. 182-190.

Ahmed, N. and D. K. Sunada, (1969), Nonlinear flow in porous media, *Jour. Hydr. Div., ASCE, 95*: pp. 1847-1857.

Amsden, A. A. and F. H. Harlow (1970), A Simplified MAC Technique for Incompressible Fluid Flow Calculations, *J. Comput. Phys., 6*: pp. 322-325.

Aris, R. (1962), Vectors, Tensors, and the Basic Equations of Fluid Mechanics, Prentice-Hall, Inc.

Armstrong, J. E., E. O. Frind, and R. D. McClellan (1994), Nonequilibrium mass transfer between the vapor, aqueous, and solid phases in unsaturated soils during vapor extraction, *Water Resour. Res., 30(2)*: pp. 355-368.

Asaeda, T., and J. Imberger (1989), Behaviours of bubble plumes in a linear stratification, *J. Jpn. Soc. Civ. Eng., 411*: pp. 55-62.

Bachmat, Y. (1965), Basic transport coefficients as aquifer characteristics, *International Association of Scientific Hydrology Symposium of Fractured Rocks, Dubrovnik, 1*: pp.63-75.

Baehr, A. L., G. E. Hoag and M. C. Marley (1989), Removin volatile contaminants from the unsaturated zone by inducing advective air-phase transport, *J. Contam. Hydrol., 4(1)*: pp. 1-26.

Bear, J. (1972), Dynamics of Fluids in Porous Media, Elsevier, NY.

Bear, J. and Y. Bachmat (1991), Introduction to Modeling of Transport Phenomena in Porous Media, Kluwer Academic Publishers, Dordrecht, The Netherlands.

Beavers, G. S., and D. D. Joseph (1967), Boundary conditions at a naturally permeable wall, *J. Fluid Mech., 30*: pp. 197-207.

Becker, S., A. Sokolichin, and G. Eigenberger (1994), Gas-liquid flow in bubble columns and loop reactors: Part II. Comparison of detailed experiments and flow simulations, *Chem. Eng. Sci., 49(24B)*: pp. 5747-5762.

Beckermann, C., R. Viscanta, and S. Ramadhyani (1988), Natural convection in vertical enclosures containing simultaneously fluid an porous layer, *J. Fluid Mech., 186*: pp. 257-284.

Benner, M. L., S. M. Stanford, L. S. Lee, and R. H. Mohtar (2000), Field and numerical analysis of in-situ air sparging: a case study, *Journal of Hazardous Materials, 72)*: pp. 217-236.

Bird, R., W. Stewart, and E. Lightfoot (1960), Transport Phenomena, Wiley New York.

Borchers, O., C. Busch, A. Sokolichin, and G. Eigenberger (1999), Applicability of the standard $k-\epsilon$ turbulence model to the dynamic simulation of bubble columns. Part II: Comparison of detailed experiments and flow simulations, *Chem. Eng. Sci., 54*: pp. 5927-5735.

Braida, W., and S. K. Ong (2000), Modeling of air sparging of VOC-contaminated soil columns, *J. Contaminant Hydro., 41*: pp. 385-402.

Braida, W., and S. K. Ong (2001), Air sparging effectiveness: laboratory characterization of air-channel mass transfer zone for VOC volatilization, *Journal of Hazardous Materials, B87*: pp. 241-258.

Brooks, R. H., and A. T. Corey (1964), Hydraulic properties of porous media, *Hydrol. Paper No. 3*, Colorado State University, Fort Collins.

Brooks, M. C., W. R. Wise, and M. D. Annable (1999), Fundamental Changes in In Situ Air Sparging Flow Patterns, *Groundwater monitoring and remediation, Spring, 1999*: pp. 105-113.

Brusseau, M. (1991), Transport of Organic Chemicals by Gas Advection in Structured or Heterogeneous Porous Media: Development of a Model and Application to Column Experiments, *Water Resour. Res., 27(12)*: pp. 3189-3199.

Buckley, S. E., and M. C. Leverett (1941), Mechanism of Fluid Displacement in Sands, *Trans. AIME, 146*: pp. 107-116.

Burdine, N. T. (1953), Relative Permeability calculations from pore-size distribution data, *Trans. AIME, 198*, pp. 71-77.

Celia, M. A., E. T. Bouloutas, and R. L. Zarba (1990), A General Mass-Conservative Numerical Solution for the Unsaturated Flow Equation, *Water Resour. Res., 26(7)*: pp. 1483-1496.

Celia, M. A., and P. Binning (1992), A mass conservative numerical solution for two-phase flow in porous media with applicaiton to unsaturated flow, *Water Resour. Res., 28(10)*: pp. 2819-2828.

Chao, K. P., S. K. Ong, and A. Protopapas (1998), Water-to-air mass transfer of VOCs: Laboratory-scale air sparging system, *Journal of Environmental Engineering, 124*: pp. 1054-1060.

Chen, M. R., R. E. Hinkley, and J. E. Killough (1996), Computed tomography imaging of air sparging in porous media, *Water Resour. Res., 32(10)*: pp. 3013-3024.

Cho, H. J., and Jaffe P. R. (1990), The volatilization of organic compounds in unsaturated porous media during infiltration, *J. Contaminant Hydro., 6(4)*: pp. 387-410.

Chorin, A. J. (1968), Numerical solution of the Navier-Stokes Equations, *Mathematics of Computation, 22(104)*: pp. 745-762.

Choudhary, M., M. Propster, and J. Szekely (1976), On the Importance of the Inertial Terms in the Modeling of Flow Maldistribution in Packed Beds, *AiCHE Journal, 22(3)*: pp. 600-603.

Corapcioglu, M. Y., A. Cihan, and M. Drazenovic (2004), Rise velocity of an air bubble in porous media: Theoretical studies, *Water Resour. Res., 40*: W04214.

Dankworth D. C, I. G. Kevrekidis, and S. Sundaresan (1990), *Dynamics of Pulsing Flow in Trickle Beds, AIChE J.. 36(4)*: pp. 605-621.

Darcy, H., (1856), Les Fontaines Publiques de la Ville de Dijon, Victor Dalmont, Paris.

Demond, A. H., and P. V. Roberts (1991), Effect of Interfacial Forces on Two-Phase Capillary Pressure-Saturation Relationships, *Water Resour. Res., 27(3)*: pp. 423-437.

Ditmars, J. D., and K. Cederwall (1974), Analysis of air-bubble plumes, in the Proceeding of 14th Conference of Coastal Engineering, Copenhagen, pp. 2209-2226.

Drew, D. A., and R. T. Lahey (1987), The virtual mass and lift force on a sphere in rotating and straining inviscid flow, *Int. J. Multiphase Flow, 13(1)*: pp. 113-121.

Drew, D. A., and S. L. Passman (2000), Theory of Multicomponent Fluids, *Applied Mathematical Sciences, 135*, Springer, NY.

Dror, I., B. Berkowitz, and S. M. Gorelick (2004), Effects of air injection on flow through porous media: Observation s and analyses of laboratory-scale processes, *Water Resour. Res., 40*, W09203.

Durst, F., A. M. K. P. Taylor, and J. H. Whitelaw (1984), Experimental and numerical investigation of bubble-driven laminar flow in an axisymmetric vessel, *Int. J. Multiphase Flow, 10(5)*: pp. 557-569.

Elder, C. R., and C. H. Benson (1999), Air Channel Formation, Size, Spacing, and Tortuosity During Air Sparging, *Groundwater monitoring and remediation, Summer, 1999*: pp. 171-181.

Elder, C. R., C. H. Benson, and G. R. Eykholt (1999), Modeling Mas Removal during In Situ Air Sparging , *Journal of Geotechnical and Geoenvironmental Eng., 125*: pp. 947-958.

Enquist, B., and S. Osher (1981), One-sided difference approximations for nonlinear conservation laws, *Mathematics of Computation, 36*: pp. 321-352.

Ergun, S., (1952), Fluid Flow through Packed Columns, *Chem. Eng. Prog., 48(89)*: pp. 89-94.

Falta, R. W., K. Pruess, I. Javandel, and P. A. Witherspoon (1992a), Numerical modeling of steam injection for the removal of nonaqueous phase liquids from the subsurface, 1. Numerical formulation, *Water Resour. Res., 28(2)*: pp. 433-449.

Falta, R. W., K. Pruess, I. Javandel, and P. A. Witherspoon, (1992b), Numerical modeling of steam injection for the removal of nonaqueous phase liquids from the subsurface, 2. Code validation and application, *Water Resour. Res., 28(2)*: pp. 451-465.

Ferziger, J. H. (1987), Simulation of Incompressible Turbulent Flows, *J. Comput. Phys., 69*: pp. 1-48.

Forsyth, P. A., Y. S. Wu, and K. Pruess (1995), Robust numerical methods for saturated-unsaturated flow with dry initial conditions in heteregeneous media, *Adv. Water Resour.* , *18*: pp. 25-38.

Gierke, J. S., N. J. Hutzler, and J. C. Crittenden (1990), Modeling the movement of volatile organic chemicals in columns of unsaturated soil, *Water Resour. Res., 26(7)*: pp. 1529-1547.

Gray, W. G. and P. C. Y. Lee (1977), On the theorems for local volume averaging of multiphase systems, *Int. J. Multiphase Flow, 3*: pp. 333-340.

Grosser K., R. G. Carbonell, and S. Sundaresan (1988), Onset of Pulsing in Two-Phase Cocurrent Downflow through a Packed Bed, *AIChE J., 34(11)*: pp.1850-1860.

Hajdin, G. (1992), Mehanika fluida (In Serbian), Faculty of Civil Engineering, Belgrade

Hall, W. A. (1956), An analytical derivation of the Darcy equation, *EOS Trans., AGU, 37*: pp. 185-188.

Harlow, F. H. and J. E. Welch (1965), Numerical calculation of Time-Dependent Viscous Incompressible Flow of Fluid with Free Surface, *The Physics of Fluids, 8(12)*: pp. 2182-2189.

Harten, A. (1983), High resolution schemes for hyperbolic conservation laws, *J. Comput. Phys., 49*: pp. 357-393.

Hassanizadeh, M. and W. G. Gray (1979a), General conservation equations for multi-phase systems: 1. Averaging procedure, *Adv. Water Resour., 2*: pp. 131-144.

Hassanizadeh, M. and W. G. Gray (1979b), General conservation equations for multi-phase systems: 2. Mass, Momenta, energy, and entropy equations, *Adv. Water Resour., 2*: pp. 191-203.

Hassanizadeh, M. and W. G. Gray (1980), General conservation equations for multi-phase systems: 3. Constitutive theory for porous media flow, *Adv. Water Resour., 3*: pp. 25-40.

Hein, G. L., J.S. Gierke, N. J. Hutzler, and R. W. Falta (1997), Three-Dimensional Experimental Testing of a Two-Phase Flow-Modeling Approach for Air Sparging, *Groundwater monitoring and remediation, Summer, 1997*: pp. 115-126.

Hirsch, C. (1990), Numerical computation of internal and external flows, Vol. 2: Computational methods for inviscid and viscous flows, *J. Willey & Sons.*

Hirt, C. W. and Cook J. L. (1972), Calculating Three-dimensional Flows around Structures and Over Rough Terrain, *J. Comput. Phys., 10*: pp. 324-340.

Hirt, C. W. and B. D. Nichols (1981), Volume of Fluid (VOF) Method for the Dynamics of Free Boundaries, *Journal of Computational Physics, 39*: pp. 201-225.

Hubbert, M. K. (1956), Darcy's law and the field equations of the flow of underground fluids, *AIME, Petrol. Trans., 207*: pp. 222-239.

Irmay, S. (1958), On the theoretical derivation of Darcy and Forcheimer formulas, *EOS Trans.*, AGU, *39*: pp. 702-707.

Ishii, M. (1972), Thermo-fluid dynamic theory of two-phase flow, Eyrolles, Paris.

Iverson, R. M., and M. E. Reid (1992), Gravity-Driven Groundwater Flow and Slope Failure Potential 1. Elastic Effective-Stress Model, *Water Resour. Res., 28(3)*: pp. 925-938.

Jacimovic, N., T. Hosoda, K. Kishida, and M. Ivetic (2006), Two-phase numerical model for air sparging simulation with modeling of acceleration terms, *Journal of Applied Mechanics, JSCE, 9*: pp. 765-771.

Ji, W., A. Dahmani, D. P. Ahlfeld, J. D. Lin, and E. Hill (1993), Laboratory study of air sparging: air flow visualisation, *Groundwater monitoring and remediation, 13(4)*: pp. 115-126.

Johnson, P. C., R. L. Johnson, C. L. Bruce, and A. Leeson (2001), Advances in In Situ Air Sparging/BioSparging, *Bioremediation Journal, 5(4)*: pp. 251-266.

Kimura, I., T. Hosoda, and S. Onda (2002), Numerical simulator on full staggered boundary fitted coordinate system for the analysis of 3D turbulent flows in open channels, *Yokkaichi University Journal of Environmental and Information Sciencies*, in Japanese, *5(1-2)*: pp. 145-170.

Kirtland, B. C. and C. M. Aelion (2000), Petroleum mass removal from low permeability sediment using air sparging/soil vapor extraction: impact of continuous or pulsed operation, *J. Contaminant Hydro., 41*: pp. 367-383.

Kobus, H. E. (1968), Analysis of flow induced by air-bubble systems, In the Proceedings of 11th Conference of Coastal Engineering, London, pp. 1016-1031.

Kothe, D. B., W. J. Rider, S. J. Mosso, J. S. Brock, and J. I. Hochstein (1996), Volume Tracking of Interfaces having surface tension in two and three dimensions, *Los Alamos National Laboratory Report AIAA 96-0859.*

Krauss, G., D. Lazik, and H. Geistlinger (2003), Gas sparging for bioremediation: Experimental investigations of gas phase distribution, *In the proceedings of 2nd European Bioremediation Conference*, Chania/Kreta, Greece.

Lake, L. W., (1989), Enhanced oil recovery, Prentice Hall, Englewood Cliffs, NJ.

Leeson, A., R. E. Hinchee, G. L. Headington, and C. M. Vogel (1995), Air Channel Distribution During Air Sparging: A Field Experiment, In: *In situ Aeration: Air Sparging, Bioventing, and Related Remediation Processes*, pp. 513-522. (Hinchee R. E., R. N. Miller and P. C. Johnson, Eds.), Battelle Press: Columbus, Ohio.

Leonard, B. P. (1979), A stable and accurate convective modeling procedure based on quadratic upstream interpolation, *Comp. Methods in Appl. Mech. Engrg, 19(1)*: pp. 59-98.

Leverett, M. C. (1941), Capillary behaviour in porous solids, *Trans. Soc. Pet. Eng., 142*: pp. 152-169.

Luckner, L., M. T. van Genuchten, and D R. Nielsen (1989), A Consistent Set of Parametric Models for the Two-Phase Flow of Immiscible Fluids in the Subsurface, *Water Resour. Res., 25(10)*: pp. 2187-2193.

Lundegard, P. D. and G. Andersen (1996), Multiphase Numerical Simulation of Air Sparging Performance, *Ground Water, 34(3)*: pp. 451-460.

Lundegard, P. D. and D. LaBrecque (1995), Air sparging in a sandy aquifer: Actual versus apparent radius of influence, *J. Contam. Hydrol., 19(1)*: pp. 1-27.

Malvern, L. E. (1969), Introduction to the Mechanics of a Continuous Medium, *Prentice-Hall, Englewood Cliffs, New York.*

Marulanda, C., P. J. Culligan, and J. T. Germaine (2000), Centrifuge modeling of air sparging - a study of air flow through saturated porous media, *J. Hazard. Mater., 72*: pp. 179-215.

McCray, J. E. and R. W. Falta (1997), Numerical Simulation of Air Sparging for Remediation of NAPL Contamination, *Ground Water, 35(1)*: pp. 99-110.

McCray, J. E. (2000), Mathematical modeling of air sparging for subsurface remediation: state of the art, *Journal of Hazardous Materials, 72)*: pp. 237-263.

McDougall, T. J. (1978), Bubble plumes in stratified environments, *J. Fluid Mech., 85(4)*: pp. 655-672.

Milgram, J. H. (1983), Mean flow in round bubble plumes, *J. Fluid Mech., 133*: pp. 345-376.

Millington, R. J. and J. M. Quirk (1961), Permeability of porous soils, *Tans. Faraday Soc., 57*: pp. 1200-1207.

Mualem, Y. (1976), A new model for predicting the hydraulic conductivity of unsaturated porous media, *Water Resour. Res., 12*: pp. 513-522.

Neuman, S. P., (1977), Theoretical derivation of Darcy's law, *Acta Mechanica, 25*: pp. 153-170.

Neuman, S. P. and Witherspoon P. A. (1971), Analysis of nonsteady flow with a free surface using finite element method, *Water Resour. Res., 7*: pp. 611-623.

Peterson, J. W., P. A. Lepczyk, and K. L. Lake (1999), Effect of sediment size on area of influence during groundwater remediation by air sparging: a laboratory approach, *Environmental Geology, 38(1)*: pp. 1-6.

Peterson, J. W., M. J. DeBoer, and K. L. Lake (2000), A laboratory simulation of toluene cleanup by air sparging of water-saturated sands, *Journal of Hazardous Materials, 72)*: pp. 167-178.

Philip, J. R. (1957), Transient fluid motions in saturated porous media, *Australian Jour. Phys., 10(43)*: pp. 1483-1496.

Pinder, G. F. and W. G. Gray (1977), Finite Element Simulation in Surface and Subsurface Hydrology, *Academic Press.*

Raats, P. A. C. and A. Klute (1968), Transport in soils: The balance of momentum, *Sols Sci. Soc. Am. Proc., 32*: pp.452-456.

Rabideau, A. J. and J. M. Blayden (1998), Analytical Model for Contaminant Mass Removal by Air Sparging, *Ground Water Monit. Rev., Fall, 1998*: pp. 120-130.

Rabideau, A. J., J. M. Blayden, and C. Ganguly (1999), Field Performance of Air-Sparging System for Removing TCE from Groudwater, *Environ. Sci. Technol., 33(1)*: pp. 157-162.

Rathfelder, K. and L. M. Abriola (1998), The influence of capillarity in numerical modeling of organic liquid redistribtuion in two-phase systems, *Adv. W. Res., 21(2)*: pp. 159-170.

Reddy, K. R. and L. Tekola (2004), Remediation of DNAPL source zones in groundwater using air sparging, *Land Contamination and Reclamation, 12(2)*: pp. 67-83.

Reddy, K. R. and J. A. Adams (2000), Effect of groundwater flow on remediation of dissolved-phase VOC contamination using air sparging, *Journal of Hazardous Materials, 72*: pp. 147-165.

Rider, W. J. and D. B. Kothe (1998), Reconstructing Volume Tracking, *Journal of Computational Physics, 141*: pp. 112-152.

Rogers, S. W., K. P. Chao, and S. K. Ong (2004), Benzene Nonaqueous Phase Liquids Removal under Air-Sparged Conditions, *Journal of Environmental Engineering, ASCE, 130*: pp. 751-758.

Roosvelt, S. E. and M. Y. Corapcioglu (1998), Air bubble migration in a granular porous medium: Experimental studies, *Water Resour. Res., 34(5)*: pp. 1131-1142.

Saez, A. E. and R. G. Carbonell (1985), Hydrodynamic Parameters for Gas-Liquid Cocurent Flow in Packed Beads, *AIChE J., 31(1)*: pp. 52-62.

Sahoo, G. B., and D. Luketina (2003), Modeling of bubble plume design and oxygen transfer for reservoir restoration, *Water Research, 37*: pp. 393-401.

Scheidegger, A. E. (1954), Statistical hydrodynamics in porous media. *Journal of Applied Physics, 25(8)*: pp. 994-1001.

Schladow, S. G. (1992), Bubble Plume Dynamics in a Stratified Medium and the Implications for Water Quality Amelioration in Lakes, *Water Resour. Res., 28(2)*: pp. 313-321.

Semer, R., J. A. Adams and K. R. Reddy (1998), An experimental investigation of air flow patterns in saturated soils during air sparging, *Geotech. Geol. Eng., 16(1)*: pp. 59-75.

Semer, R. and K. R. Reddy (1998), Mechanisms controlling toluene removal from saturated soils during in situ air sparging, *Journal of Hazardous Materials, 57*: pp. 209-230.

Slattery, S. (1967), Flow of viscoelastic fluids through porous media, *AIChE J.*, *13*: pp. 1066-1071.

Slattery, S. (1969), Single-phase flow through porous media, *AIChE J.*, *13*: pp. 866-872.

Sokolichin, A. and G. Eigenberger (1994), Gas-liquid flow in bubble columns and loop reactors: Part I. Detailed modelling and numerical simulation, *Chem. Eng. Sci.*, *49*: pp. 5735-5746.

Sokolichin, A. and G. Eigenberger (1999), Applicability of the standard $k - \epsilon$ turbulence model to the dynamic simulation of bubble columns. Part I: Detailed numerical simulation, *Chem. Eng. Sci.*, *54*: pp. 2273-2284.

Sokolichin, A., G. Eigenberger, and A. Lapin (2004), Simulation of Buoyancy Driven Bubbly Flow: Established Simplifications and Open Questions, *AIChE J.*, *50(1)*: pp. 24-45.

Sweby, P. K. (1984), High resolution schemes using flux limiters for hyperbolic conservation laws, *SIAM Journal on Numerical Analysis*, *21(5)*: pp. 995-1011.

Unger, J. A., E. A. Sudicky, and P. A. Forsyth (1995), Mechanisms controlling vacuum extraction coupled with air sparging for remediation of heterogeneous formations contaminated by dense nonaqueous phase liquids, *Water Resour. Res.*, *31(8)*: pp. 1913-1925.

van Dijke, M. I. J., S.E.A.T.M. van der Zee, and C.J. van Duijn (1995), Multi-phase flow modeling of air sparging, *Adv. W. Res.*, *18(6)*: pp. 319-333.

van Dijke, M. I. J. and S.E.A.T.M. van der Zee (1998), Modeling of air sparging in a aLayered Soil: Numerical and Analytical Approximations, *Water Resour. Res.*, *34(3)*: pp. 341-353.

van Genuchten, M. T. (1980), A closed-form equation for predicting the hydraulic conductivity of unsaturated soils, *Sci. Soc. Am. J.*, *44*: pp. 892-898.

van Leer, B. (1979), Towards the ultimate conservative difference scheme. V. A second order sequel to Godunov's method, *J. Comput. Phys.*, *32*: pp. 101-136.

Welch, J. E., F. H. Harlow, J. P. Shannon, and B. J. Daly (1965), A computing technique for solving viscous, incompressible, transient fluid-flow problems involving free surfaces, *Los Alamos Scientific Laboratory Report*, LA.3425.

Whitaker, S. (1966), The equations of motion in porous media, *Chem. Engin. Sci.*, *21*: pp. 291-300.

Whitaker, S. (1969), Advances in theory of fluid motion in porous media, *Ind. Eng. Chem.*, *61*: pp. 14-28.

Viecelli, J. A. (1971), A Computing Method for Incompressible Flows Bounded by Moving Walls, *J. Comput. Phys.*, *8*: pp. 119-143.

Wilson, D. J., A. Clarke, K. Kaminski, and E. Chang (1997), Groundwater Cleanup by In-Situ Sparging. XIII. Random Air Channels for Sparging of Dissolved and Nonaqueous Phase Volatiles,*Sep Sci. Technol.*, *32(18)*: pp. 2969-2992.

Wilson D. J., J. M. Rodiguez-Maroto and C. Gomez-Lahoz (1994), Groundwater Cleanup by In-Situ Sparging. VI. A Solution/Distributed Diffusion Model for Nonaqueous Phase Liquid Removal,*Sep Sci. Technol.*, *29(11)*: pp. 1401-1432.

Wooding, R. A. (1957), Steady state free thermal convection of liquid in a saturated permeable medium, *J. Fluid Mech.*, *2*: pp. 273-285.

Wu, Y. S. (2001), Non-Darcy displacement of immiscible fluids in porous media, *Water Resour. Res.*, *37(12)*: pp. 2943-2950.

Wuest, A., N. H. Brooks, and D. M. Imboden (1992), Bubble Plume Modeling for Lake Restoration, *Water Resour. Res.*, *28(12)*: pp. 3235-3250.

Youngs, D. L. (1982), Time-dependent multi-material flow with large fluid distortion, *Numerical Methods for Fluid Dynamics*, pp. 273-285.